DC, Microwave and Optoelectronic Characterization of $YBa_2Cu_3O_{7-x}$ Nano-scale Thin Film Structures

by

Thomas G. McConkey

A thesis
presented to the University of Waterloo
in fulfillment of the
thesis requirement for the degree of
Master of Applied Science
in
Electrical and Computer Engineering

Waterloo, Ontario, Canada, 2012

Author's Declaration

I hereby declare that I am the sole author of this thesis. This is a true copy of the thesis, including any required final revisions, as accepted by my examiners.

I understand that my thesis may be made electronically available to the public.

Thomas G. McConkey

Abstract

The nonlinear electrodynamic characteristics and presence of vortex dynamics in pseudo 2-dimensional microbridges make them attractive to design novel passive and active microwave circuits. Before such applications could be feasibly accomplished, a greater understanding of the the these devices are necessary, by a complete DC, microwave and optoelectronic characterization.

A cryostat design and construction is discussed including the creation of test beds for DC characterization. Coplanar waveguide (CPW) design methodology is presented and used for the creation of CPWs for microwave characterization. Microbridges and meander lines are also embedded into the CPWs for determining the microwave performance of said devices and for optoelectronic characterizations.

Results are compared against accepted results from theory and simulations, introducing vortices as explanations for device behaviour. Feasibility of these devices as single photon detectors is discussed.

Acknowledgments

I would like to first express my gratitude and appreciation to my supervisor, Dr. Hamed Majedi, who has provided guidance and support through out this research. I must extend this to both current and past members of our research group, Integrated Quantum Optoelectronics Lab. Haig Atikian for initial assistance with CPW design and Dr. Hamid Mohebbi for guidance with microwave theory. Amir Salim and Amin Eftekharian for discussions and suggestions in regards to superconductive theory. Dr. Mohsen Akhlagi for the laboratory guidance and use of his helium cryostat and Jean-Luc Orgiazzi for his guidance on cryostat design.

I would also extend my thanks to the staff of both the Physics Machine Shop and the Engineering Student Machine Shop for their assistance and guidance. Om Patange for his assistance with Dr. David Cory's AFM.

I would like to thank both of my readers, Dr. Adrian Lupascu and Dr. Dayan Ban, for taking the time to review this thesis.

I thank both the University of Waterloo, IQC and the Government of Ontario for their financial support of my research.

Finally I would like to thank my family and friends for their support through out this research.

Contents

List of Figures

List of Tables

Chapter 1

Introduction

1.1 History of Superconductivity

It was well known by the late 19th century that the resistance of a conductor is inversely proportional to temperature, and was viewed as an important issue for theoretical explanation by leading scientists for temperatures approaching absolute zero. It was from the extensive cryogenic research and liquefying of helium by Heike Kamerlingh Onnes that superconductivity was discovered in mercury in 1911 [1]. Research in the Leiden laboratory, Onnes' research group, continued to determine other superconducting materials, including some of their parameters [2]. Further discoveries were made during the early 20th century, such as the magnetic properties of superconductors by Meissner and Ochsenfeld [3]. This work led to what is now known as the Meissner effect and the thermodynamic treatment of superconductivity.

It was at a similar time that the London brothers, known for the superconducting parameter the London penetration depth (λ_L), published their semi-phenomenological theory of superconductivity and explained the Meissner effect [4]. Their work also explained the connection between critical current (I_c) and critical temperature (T_c). A more profound phenomenological explanation of the macroscopic properties of superconductors was published by Vitaly Lazarevich Ginzburg and Lev Landau in 1950 [5]. It was from this work that in 1957 Abrikosovo showed that superconductors fall into two groups (Type I and Type II) due to magnetic properties, and further introduced the idea of vortices as an explanation of how magnetic flux penetrates the type II superconductor [6]. It was at roughly the same time that the first theoretical explanation of superconductors based on quantum first principles was given by Bardeen, Cooper and Schrieffer (BCS), introducing the concept of 'cooper pairs' [7].

With greater understanding of the physics of superconductors, much work was now being pursued with the goal of higher T_c. Attempts along organic superconductors were made, [8], but it was not until the work by Georg Bednorz and Alex Muller that a breakthrough in T_c was achieved with perovskite-type oxides [9], the first high temperature superconductors (HTS). It was shortly after that YBCO was discovered with a T_c of 93 [K], the first to be above the boiling temperature of liquid nitrogen (LN2) [10]. With cooling to such higher temperatures being significantly easier, pursuit of practical applications began in earnest. However the fabrication of perovskite-type oxides is still proving much more difficult than the standard low temperature superconductors (LTS), and the physics behind how these oxides transition to the superconductive state is still not fully understood.

1.2 Superconductor Theory

A heavy in depth review on the theory of superconductivity would be beyond the scope of this work as it is primarily experimental in nature. However some basic understanding of the behavior and current theories of superconductivity, more specifically that of Type II HTS, is helpful for both understanding experimental results and determining what behavior is being observed.

The basic current standing explanation behind superconductivity is BCS theory, which states that at low enough temperatures electrons near the Fermi surface form pairs, called cooper pairs, with opposite momentum and spin by way of virtual phonons [2, 11]. These cooper pairs, which have a 'size' of a coherence length (ξ), are composite bosons, which allow all the cooper pairs to be in the same ground state. This allows a simplified view of the system as a macroscopic quantum state, following Ginzburg-Landau theory, where the superconductor is represented by the macroscopic quantum wave function Ψ, which can be represented by

$$\Psi = |\Psi| \, e^{j\phi} \tag{1.1}$$

where $|\Psi|$ can be viewed as the density of cooper pairs, or superfluid density. Given the total charge density in the superconductor n_0, one can determine the temperature dependent normal and superconductor charge carrier density

$$n_s(\mathrm{T}) = n_0 \begin{cases} 0 & \mathrm{T} \geq \mathrm{T}_c \\ 1 - \left(\frac{\mathrm{T}}{\mathrm{T}_c}\right)^{\gamma} & \mathrm{T} \leq \mathrm{T}_c \end{cases} \tag{1.2}$$

$$n_n(\mathrm{T}) = n_0 \begin{cases} 1 & \mathrm{T} \geq \mathrm{T}_c \\ \left(\frac{\mathrm{T}}{\mathrm{T}_c}\right)^{\gamma} & \mathrm{T} \leq \mathrm{T}_c \end{cases} \tag{1.3}$$

where γ is a phenomenogical parameter dependent on the material in question, for the case of YBCO, it is generally accepted to be 2. The superfluid density is also approximately equal to $1/(\lambda_L(\mathrm{T})^2)$ [12]. T_c refers to the critical temperature, the upper temperature bound to which the material remains in the superconducting state. Two other critical values are the critical current (I_c) and critical magnetic field (H_c), as can be seen in the phase diagram Fig. 1.1a, above which the material transitions to the normal state. It is important to note that the relative critical values during operation are highly dependent on each other. A superconductor does not just have zero resistance such as a perfect conductor, but also perfect diamagnetism from the Meissner effect: the exclusion of magnetic fields (up to H_c) from the superconducting material by screening currents. The magnetic field does still penetrate some of the surface of the superconducting material, the depth of which is referred to as the London penetration depth (λ_L).

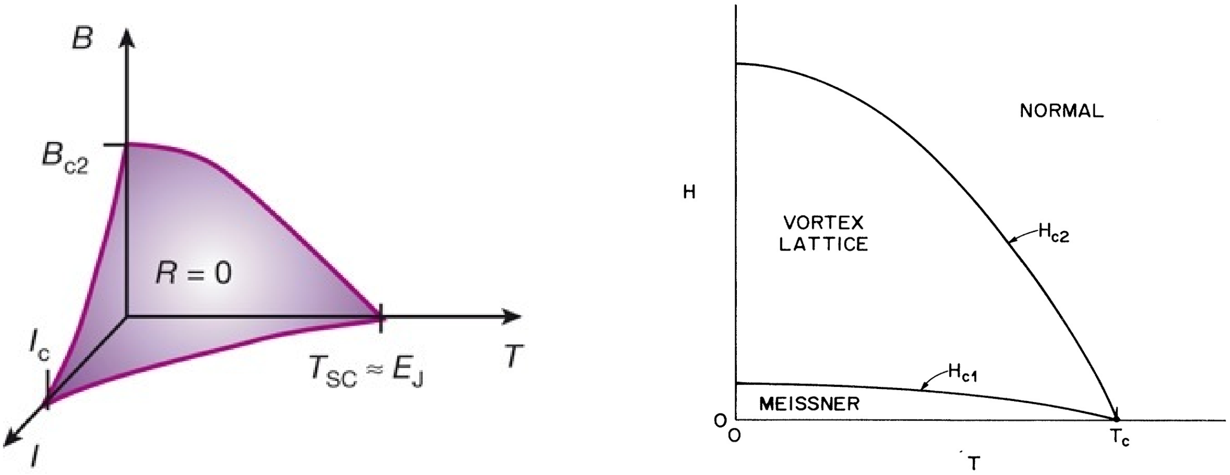

(a) Phase Diagram of a Superconductor, showing T_c, I_c, B_c [13]

(b) Phase Diagram of Type II Superconductor showing H_c1 and H_c2 [14]

Figure 1.1: Phase Diagrams of Superconductors

The behaviour of a superconductor in a magnetic field actually falls into two categories, Type I and Type II, which can be determined from a materials Ginzburg-Landau parameter, κ. Type I, $\kappa < 1/\sqrt{2}$, follows the previous explanation that when an applied field reaches H_c the material switches from the Meissner state to the normal state, with the magnetic flux fully penetrating the material. Type II, $\kappa > 1/\sqrt{2}$, however have two critical points, H_{c1} where the material switches from Meissner state to a partial penetration of the flux or 'Vortex' state, and H_{c2} where the material reaches full flux penetration and switches to normal state, as seen in Fig. 1.1b. The vortices can be simplistically viewed as a hurricane of supercurrent with an eye that is in a normal state. The radius of the supercurrent circulating around the normal state core is λ_L where the radius of the normal state core is ξ [2].

$$\kappa = \frac{\lambda_L(\mathrm{T})}{\xi(\mathrm{T})} \tag{1.4}$$

This is important to note as the material being used for this work, $YBa_2Cu_3O_{7-x}$, is strongly Type II, with a $\kappa(0) \approx 70$ (in the a-b plane). It is a highly anisotropic cuprate material, as can be seen from Fig. 1.2, and as such the values given in Table 1.1, are specifically for the a-b plane. There is a slight difference between the value for λ_{La} and λ_{Lb}, but as they are relatively close, the average value is taken.

Table 1.1: Standard Superconducting Parameters for YBCO, (a) - Post Fabrication report from THEVA

London Penetration depth ($\lambda_L(0)$) [15]	150 [nm]
Coherence Length ($\xi(0)$) [16]	3 [nm]
Critical Temperature - Thin Film (T_c)^a	85.6 [K]

It should also be noted that BCS theory, although it explains the behaviour of LTS superconductors very well, does not fully explain the behaviour of HTS superconductors, though recent work with the resonating valence bond model has provided understanding of previously anomalous properties of the cuprates [17]. It is certainly beyond the scope of this work to hope to find a more optimal explanation, but the resulting measurements may provide assistance in reaching such an understanding.

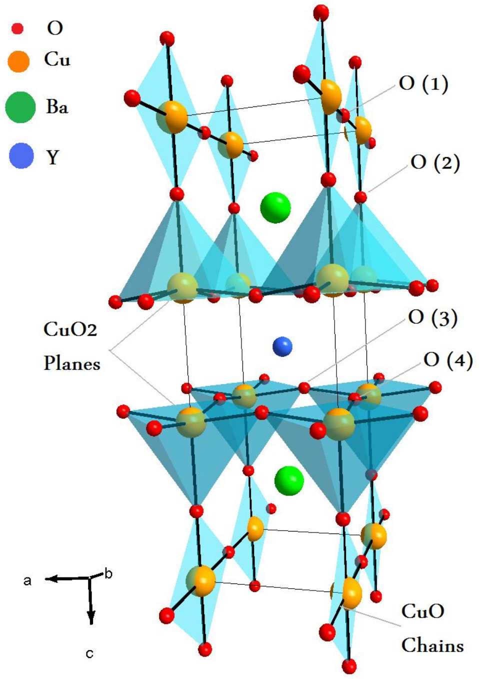

Figure 1.2: YBCO lattice structure showing abc orientation, roughly 1.17 nm 'tall' on c-axis [12] figure origin:public domain

1.3 Thesis Purpose and Organization

The initial driving idea behind this thesis was due to the interesting results obtained by a previous graduate student of the Integrated Quantum Optoelectronics Lab, Haig Atikian, whom had been working on 100 [nm] thin film YBCO microwave and optoelectronic devices. Specifically the photoresponse results of these devices and the apparent Josephson Junction like behaviour of IV measurements. This lead to the goal of both a better understanding of the mechanics behind these behaviours and what methods could be employed to amplify said behaviours for the benefit of device application, with the ultimate goal being a YBCO based superconductive single photon detector. The steps to this goal is through the DC, microwave and optoelectronic characterization of an even thinner film, 25 [nm], which ideally also translates into greater sensitivity. To accomplish this, a cryostat and test bed for taking DC measurements, specifically resistance-temperature and current-voltage measurements, had to be designed, created and implemented. The designing and then testing of the YBCO devices in the previously mentioned cryostat in addition to an already available microwave cryostat would complete the intended goals.

The thesis is broken down into three primary chapters. Chapter 2 discusses the design process behind the cryostats, test bed and YBCO devices. This includes the design methodology used behind the YBCO CPW structures and the thermal calculations applied to the created cryostat to insure proper operations. Chapter 3 presents relevant background theory on DC measurements of similar materials and designs and discusses and analyzes the DC measurements made for this work. Analysis leads to attempts at applying vortex mechanics as a method to explain device behaviour. Chapter 4 follows the style of Chapter 3 but for microwave and optoelectronic measurements. Specifically analyzing the behaviour of the CPWs S-Parameter measurements and the possible explanations for the discrepancy when compared to simulation results, and the changes in S-Parameters when devices are subject to excitation from a 1310 [nm] laser.

Chapter 2

Apparatus

It should be noted by the reader that all references made in this chapter, unless otherwise noted, are from the experimental text book by Ekin [18]. It is an excellent source for any superconductoring based experiments, though still has useful explanations and examples for low temperature or electronically sensitive research.

As is the case with much experimental work, custom test setups had to be designed and built for the purpose of this thesis. Although for the microwave and optoelectronic experiments a previously constructed microwave cryostat was available, as discussed in Sec. 2.2, a setup for DC characterization was required.

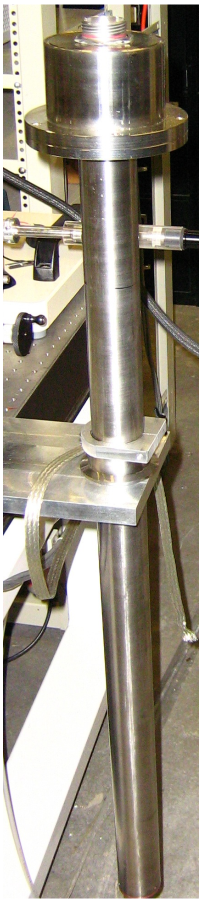
Figure 2.1: Dipper Probe

2.1 Dipper Probe

The YBCO/MgO wafer, discussed further in Sec. 2.3, had been designed and fabricated before the cryostat for DC characterization was considered, leading to a top-down design process. This is a non-ideal approach as nearly all aspects of the cryostat had to be custom designed, leading to greater expense and time consumption. A bottom-up approach is more desirable when possible, and would merely require the designing of the contact pads and number of devices per sample section on the YBCO/MgO wafer to be based on the geometry of a commercially available sample holder, such as a surface mount Kapton material substrate chip carrier.

Due to the requirements and restrictions present, it was determined a dipper probe was the optimal cryostat design for the DC characterization measurements as less than 1 [A] of current was expected to be required during current-voltage (IV) sweeps. It would provide excellent thermal coupling between the samples and the cryogen, while being relatively simple to construct and easily modified. Such a design would lead to cryogen boil off that is not recaptured, but this was not a concern due to the low cost and relative abundance of liquid nitrogen.

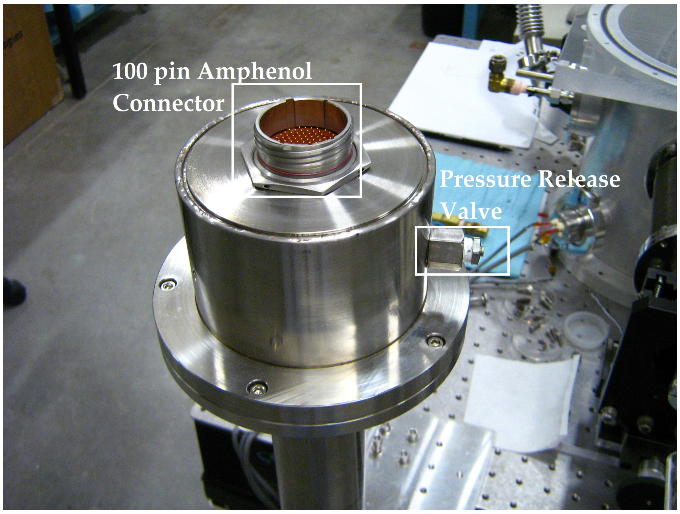

Figure 2.2: Dipper probe head connector and pressure release valve.

A two inch thin walled (0.01") stainless steel tube was used as the body of the dipper probe. This was capped with a removable, o-ring sealed steel connector head, as seen in Fig. 2.1. A pressure release valve was added to the connector head to avoid an unsafe pressure build up, as any liquid nitrogen that may have seeped into the dipper probe during a cool down cycle would quickly raise the internal pressure after warming up, and has been known to cause pressure explosions. The top of the connector head was fitted with a free unique jam nut 100 pin connector provided by Amphenol Aerospace. It was from a canceled series of prototype test connectors they had made for low temperature/pressure use with each pin being individually hermetically sealed. It was paired with a matching connector to which shielded twisted pair wire was attached for connecting to the Keithley Sourcemeter 2400 and Lakeshore Temperature Controller 332, Fig. 2.3.

The internal wiring was a combination of Kapton clad 32 AWG copper wire and enameled 34 AWG magnesium wire, made into twisted pair with an automatic drill, following (2.1) in order to determine the maximum twist length (l_t) to minimize the induced voltages, from wire diameter

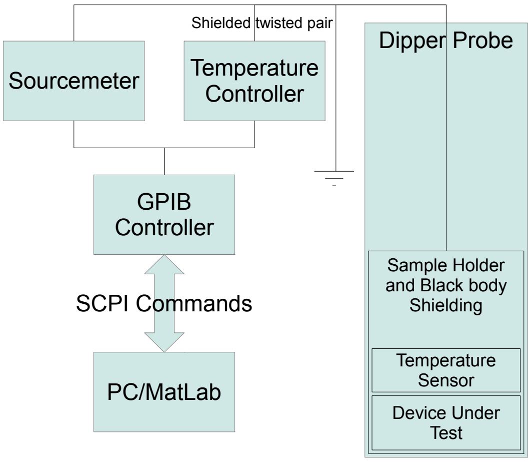

Figure 2.3: Block Diagram of DC Measurement Setup

(d_w). The choice of wire size was based off the data provided from Appendix 4.1a of [18]. Twisted pair was used over coaxial cable as it is more effective at minimizing any magnetically induced noise voltage, which was a concern in the testing environment as the cryostat did not have any mu-metal shielding incorporated into the design. The body of the cryostat was to be grounded, to a universally shared ground, providing a simple Faraday cage around the sample during testing.

$$l_t \leq 20d_w \tag{2.1}$$

The wires were connected to two 30 pin female socket connectors, 1 [mm] pitch Pico-Clasp series, which had matched surface mount connectors on the PCB, Sec. 2.1.2. This was accomplished with the use of the in lab micro-soldering station and fine tipped crimper. Liberal application of flux was required to allow clean flow of solder into the crimped section of the wire/pin. The solder surface tension at this scale and rate of oxidization was too great for clean bonding otherwise. Care also had to be taken to avoid over soldering as this would clog the pin receptacle making the connector useless. For this reason a mocked up soldering bed had to be created, allowing for good thermal contact of a heat sink to allow a fast cooling time of the solder while providing mechanical stability.

The sample holder of the dipper probe was constructed from a solid piece of an oxygen free copper cylinder in order to maximize heat flow from the sample under test. A hatch pattern of

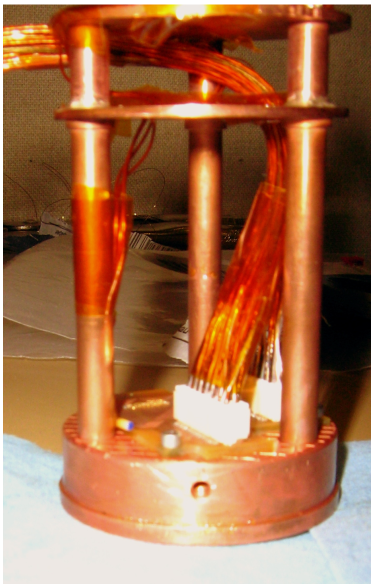

Figure 2.4: Photo of the compiled blackbody shielding and copper base with PCB sample holder screwed into position. Connection leads and temperature sensor wires seen running through the shielding.

thin shallow grooves was cut into the surface of the copper, as it was found it improved thermal contact between the sample and sample holder. Without these channels, the thermal grease or silver cement used to bond the two together may form an excess film, lowering the thermal contact. The channels also provide a path for acetone to flow in order to remove the sample when silver cement was used. The sample holder was attached to two layers of thin polished copper by three columns of copper, as seen in Fig.2.4, to act as shielding from black body radiation. Radiative heat transfer can be a significant concern in a cryostat environment, as calculated in Sec. 2.1.1. A 100 [Ω] platinum temperature sensor was attached to the columns of the shielding, so as to see when the test bed had cooled to below estimated T_c. During testing it was found that this location of the temperature sensor was giving unreasonable T_c values of the devices under test (DUT), and so was relocated to the copper test bed.

2.1.1 Thermal Calculations

To insure that the cryostat would successfully cool down the DUT, heat transfer calculations for this design were evaluated. This would also allow an estimation on the rate of LN2 consumption during testing, though this was not too great of a concern. A worst case scenario was assumed, such as heat transfer through the steel tube being fully absorbed by the copper sample holder, which was certainly not the case. Assuming the worst case scenario also allows for simplification of the calculations. The initial requirement was to determine the temperature the top surface of the copper sample holder would be at once the dipper had been immersed in LN2 and reached a thermal steady state. First the heat conduction from room temperature through the stainless steel support tube and the copper/magnesium wire instrumentation leads was found from

$$\dot{q}_{cond} = \frac{A}{L} \int_{\mathrm{T}_1}^{\mathrm{T}_2} \lambda(\mathrm{T}) dT \tag{2.2}$$

where A is the cross sectional area, orthogonal to the direction of temperature change, L is the length, and T_2 and T_1 are the temperatures of the ends of the object in question and $\lambda(\mathrm{T})$ is the temperature dependent thermal conductivity. For our purposes T_2 is taken to be room temperature (300K) and T_1 the temperature of the copper sample holder. As the thermal conductivity of high purity metals is nonlinear at low temperatures, Appendix 2.1 from [18] is used for solving of (2.2). As these values are given for the thermal conductivity between a T and 4K, (2.3) must be used to determine the thermal conductivity at LN2 temperature, 77.4 [K] (T_{LN2}). As limited data points were provided, a linear simplification was taken to determine the thermal conductivity between the available temperature points, following (2.4).

$$\dot{q}_{cond} = \frac{A}{L} \left[\int_{4\mathrm{K}}^{\mathrm{T}_2} \lambda(\mathrm{T}) dT - \int_{4\mathrm{K}}^{\mathrm{T}_1} \lambda(\mathrm{T}) dT \right] \tag{2.3}$$

$$\int_{4\mathrm{K}}^{b} \lambda(\mathrm{T}) dT = (b-a) \frac{\int_{4\mathrm{K}}^{c} \lambda(\mathrm{T}) dT - \int_{4\mathrm{K}}^{a} \lambda(\mathrm{T}) dT}{c-a} + \int_{4\mathrm{K}}^{a} \lambda(\mathrm{T}) dT \quad c > b > a \tag{2.4}$$

In a cryogen environment, any line of sight paths between areas of extreme temperature difference can be of significant concern due to radiative heat. Although radiative heat is present no matter the temperature of the object (except absolute zero that is), the temperature difference between two surfaces leads to a net gain for the colder surface. The radiative heat transfer is found from

$$\dot{q}_{rad} = \sigma \boldsymbol{E} A \left(\mathrm{T}_2^4 - \mathrm{T}_1^4 \right) \tag{2.5}$$

where σ is the Stefan-Boltzmann constant, 5.67×10^{-8} [W/(m^{2}K^4)], and $\boldsymbol{E}$, of parallel plates, is found from

$$\boldsymbol{E} = \frac{\epsilon_1 \epsilon_2}{\epsilon_1 + \epsilon_2 - \epsilon_1 \epsilon_2} \tag{2.6}$$

where ϵ is the emissivity of the surfaces in question. With no blackbody shielding the radiative heat from the top of the dipper probe would reach the sample holder, which from its non-planar layout and non-reflective surface (from the PCB), would absorb a great deal of it. The blackbody shielding not only intercepts the radiative heat, but from being both a parallel flat surface and highly reflective causes the amount absorbed to be comparably lower. If the DUT or blackbody shielding is fully submerged, the radiative heat would be completely absorbed by the LN2 (giving an $\boldsymbol{E}$ of 1) and would only be a concern for determining the rate of boil off.

Joule heating from the current leads can be a concern, but as the expected maximum current to be used in these measurements was to be under 100 [mA], resulting in worst case $\dot{q}_{JH}$ on the order of 1 [mW], it was ignored for this analysis. Finally the heat conduction across the liquid/solid interface of the copper sample holder and the LN2 is required, given as

$$\frac{\dot{q}}{A} = 5 \times 10^2 \Delta \mathrm{T}^{2.5} \left[\mathrm{W/m^2(K^{-2.5})}\right] \tag{2.7}$$

Though this is for low levels of heat flux, when the liquid nitrogen is only undergoing nucleate boiling, which once having reached thermal steady state is a fair assumption as thermal power output from DUTs during testing is expected to be minimal. Resulting calculations found the total input to be no more than 0.19 [W] even with the top of the copper surface at LN2 boil temperature, with a balanced temperature being reached at only 0.03 [K] above that of LN2. This slight temperature difference is primarily due to the thermal output being 50 [W/K]. This input also translates into an additional LN2 consumption of 4 [mL] an hour, which pales in comparison to that lost during initial cool down, which is on the order of a liter.

Another concern is that the actual samples are well thermally coupled to the copper sample holder. If poorly coupled, inaccurate IV measurements could result, as self heating of the device would lead to lower I_c values than theoretically expected, and possibly thermally induced hysteresis when sweeping with current. The use of thermal grease or silver cement paired with a method to increase pressure between the two surfaces can significantly improve the thermal coupling.

2.1.2 Printed Circuit Board

The geometry of the contact pads on the wafer for the DC devices were initially designed with plans of using a probing station. As this option of measurement ended up being unavailable, and four point measurements were desired, wedge wire bonding was the best viable option to connect the DUT to the rest of the cryostat system. Specifically wedge wire bonding as ball bonding would damage the YBCO material from the sudden temperature rise. Although other options, such as pogo pins, are also good choices, none with the required pitch size could be found. Due to the contact pad size and device layout, Fig. 2.6c, a very small trace and space was required (0.004" or 100 [mm]). A standard FR4 substrate with 0.006" trace, 0.004" space, 0.5 ounce weight copper and no solder mask or silk screen was ordered from Fine Circuits, following the design seen in Fig. 2.5.

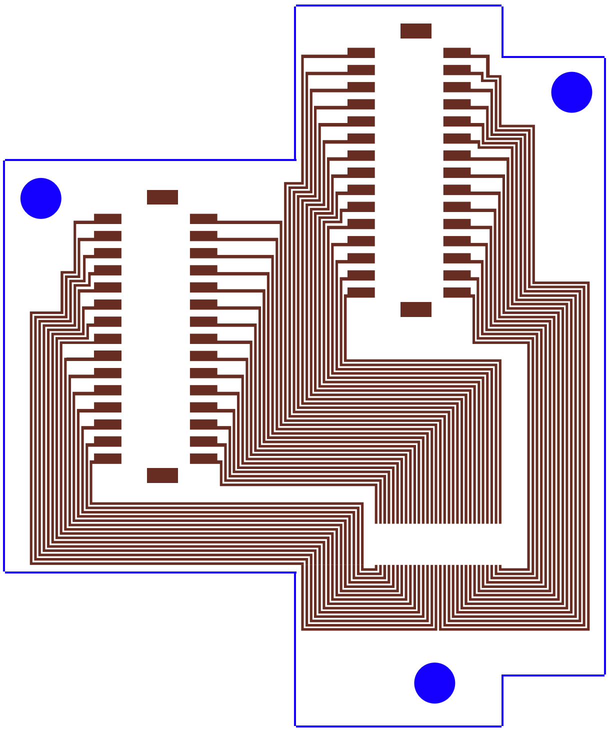

Figure 2.5: Printed circuit board design created with Agilent Design Software. Lines are 150 [um] wide with 100 [um] spacing.

Although a surface finish of soft gold would have protected against oxidization and slightly improved wedge bond contacts, it significantly increased the cost and so was not included in the design. Other surface finishes would have protected against oxidization, but the PCBs were to be kept in a humidex safe significantly limiting the oxidization, and wedge bond tips may have been damaged on surfaces they are not designed for. A Kapton substrate would have improved thermal coupling to the copper sample stage, but the significantly higher cost for minimal benefit was deemed unnecessary for these experiments. It would be worth considering though for much lower temperature experiments that have devices far more sensitive to thermal fluctuations.

The order of the work done on the PCBs was planned out carefully, as the YBCO samples could not be exposed to high temperatures, such as would occour from any soldering, to water, or exposed to high humidity atmosphere for great periods of time. Such exposures result in damage to the YBCO, from a change in the oxygen content of the material. An initial prototype found that wire bonding to a sample that was bonded directly to the surface of the PCB required a large loop size due to the 500 [um] thickness of the MgO, as can bee seen in Fig. 2.6c. This was resulting in bonds sometimes not holding well to the copper lines and increased time requirements due to the large height difference. To compensate, 500 [um] deep pockets were drilled into the FR4 by use of a lathe drill with a 60 gauge drill bit. To fit the DC samples and providing some space for excess silver cement to flow, while also compensating for the curved corners inherent from lathe drilling, the pocket dimensions were set to 9 [mm] x 2.3 [mm]. The drilled pockets also improved thermal coupling of the DC samples to the copper base, and simplified contact pad to copper line alignment.

With the pockets drilled the surface mount connectors could be soldered to their matching contact pads on the PCB, after the contacts had been lightly sanded (ISO P2000) to remove oxidization, then cleaned in an acetone ultrasonic bath and rinsed in isopropynol. A solder paste in combination with a heating pad was first attempted, but uneven heat distribution was giving poor contacts and weak bonding. An alternative surface mount soldering technique was used with the micro-soldering station and microscope.

The connector is held in place temporarily with a clamp or tape ensuring the pins and copper contacts are aligned. A liberal amount of flux was applied to the pins to insure the metal was non-oxidized and that the wetting characteristic of the solder was high enough that the solder forms a strong intermetallic bond. A solder wire was placed across the pins, with the solder tip being slowly dragged across. The excess flux insured the solder was attracted to the copper pads and pins. Some cleaning up of the contacts with spot soldering was often required but easily accomplished. The PCB was then again placed in an acetone ultrasonic bath, then rinsed with isopropynol to remove any excess flux. Due to cleaning with acetone it was paramount the connectors body not be made from plastic, as this would be melted. Because of this connectors with a nylon body were purchased, specifically 1mm Pitch Pico-Clasp$^{\text{TM}}$ Wire-to-Board series from Molex. Finding a good quality and reasonably priced connector with a pitch size that could accommodate the number of lines present on the PCB proved difficult.

The DC samples were then placed in the previously drilled pockets, insuring the gold contact pads aligned with the appropriate copper lines on the PCB, with a thin layer of 'Leitsilber' Conductive Silver Cement and allowed to dry in a humidex safe. Connections between the copper lines and pads were made using the wedge bonding station, using the (50 [um]) gold wire. The copper lines were first lightly sanded to remove any oxidization and improve both conductivity

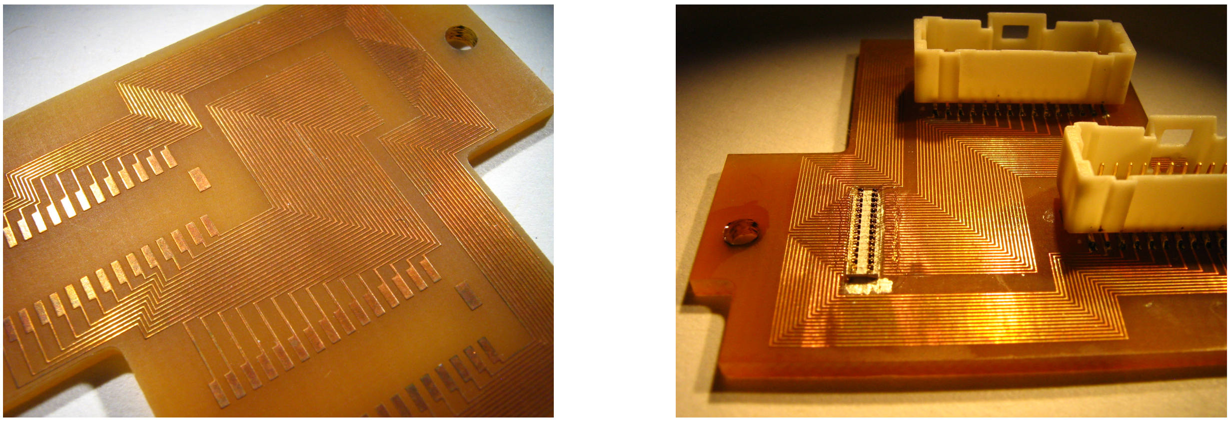

(a) Printed circuit board - no solder mask or silkscreen included.

(b) Compiled PCB - surface mounts soldered, sample cemented and wire bonded to.

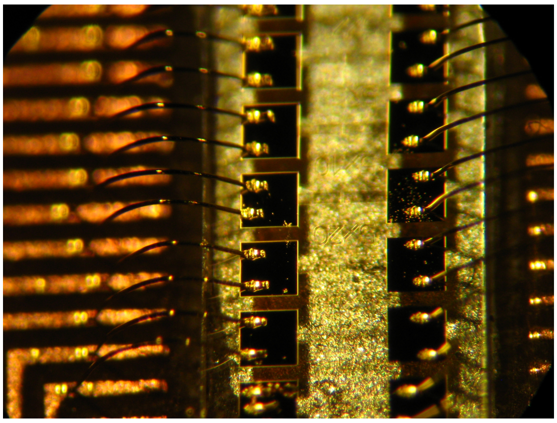

(c) Zoomed in view of the 4-point contacts

Figure 2.6: PCB Construction

and bonding strength. The narrowness of the copper lines, such that the surface of the lines were actually noticeably curved, often resulted in poor bonds that had to be redone, sometimes damaging the gold contact pads in the process.

After numerous bonds, as roughly 150 devices were measured for the DC portion of this work or 600 bonds, no completely consistent settings were found to work on the wedge bonder. Generally one contact pad on a sample would be used for calibrating the bonder, which although would at times result in the relevant device being unmeasurable, would result in strong clean bonds for the rest of the devices on the sample.

It should be noted that dependent on the expected current the minimum contact area (A_c) required to insure that the joule heating generated by the interface resistance is minimal can be determined. Working from (2.7) as the basis for the rate of cooling and desiring a maximum temperature rise of 0.5 [K], the maximum resistance (R_c) can be found from

$$R_c \leq \dot{q} I^{-2} \tag{2.8}$$

where I is the expected current. By determining the effective contact resistivity, the minimum area (A_c) can be found by

$$A_c \geq \frac{\rho_{c\ \text{eff}}}{R_c} \tag{2.9}$$

where $\rho_{c\ \text{eff}}$ is the effective specific contact-interface resistivity.

2.2 Microwave Cryostat

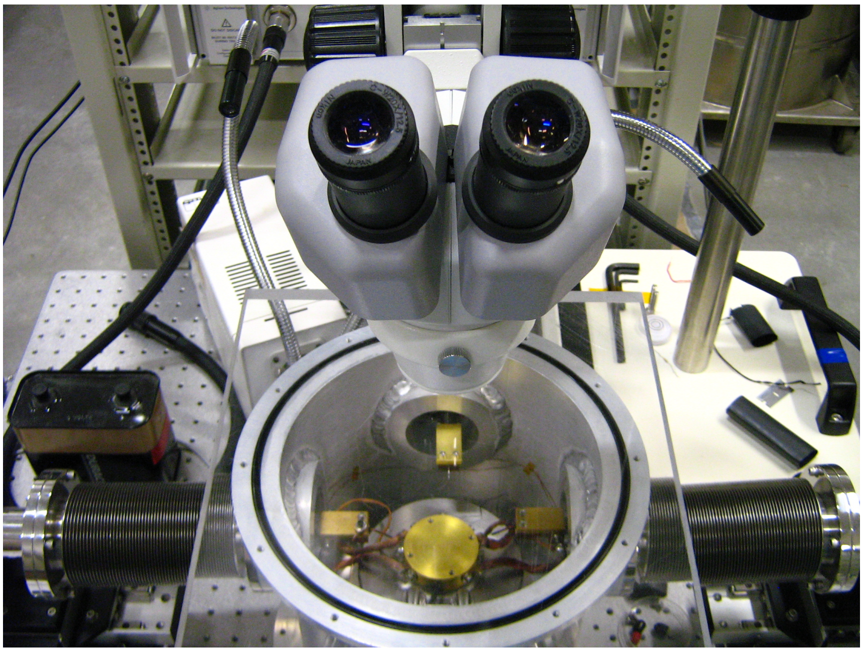

Figure 2.7: Microwave Cryostat

The microwave cryostat, Fig. 2.7, was created by a former graduate student in the Integrated Quantum Optoelectronics Lab, Haig Atikian. An in-depth description of the construction of this cryostat is given in his thesis, "Microwave Photonic Characterization of High Temperature Superconducting Optoelectronic Devices", but a brief description is given below.

The body of the cryostat was constructed from 6061 aluminum alloy, with four flanges at 90 degree separations on the outer sidewall of the body. These flanges serve as ports for the two microwave probe arms, the optic fiber probe arm, and the inlet/outlet for the cryogen reservoir, which are all sealed with o-rings to allow the internal compartment to be pumped down to vacuum. Two additional smaller flanges are present below and offset from the inlet/outlet flange, for electrical leads such as for temperature sensors and for attaching to the two stage vacuum pump from BOC Edwards. When optimally sealed the internal compartment can be pumped down to roughly 5×10^{-5} [mbar]. The cryogen reservoir was capped with a 2 inch copper rod, so that the majority of the rod would be submerged in the LN2 during operation, with a half inch protruding from the top. The copper rod was gold plated to protect it from any oxidization, as this significantly lowers the conductivity across any solid/solid interface. A soft silver solder, Staybrite$^{\mathrm{TM}}$, was used to solder the rod into place, and prevent any LN2 from leaking into the vacuum environment.

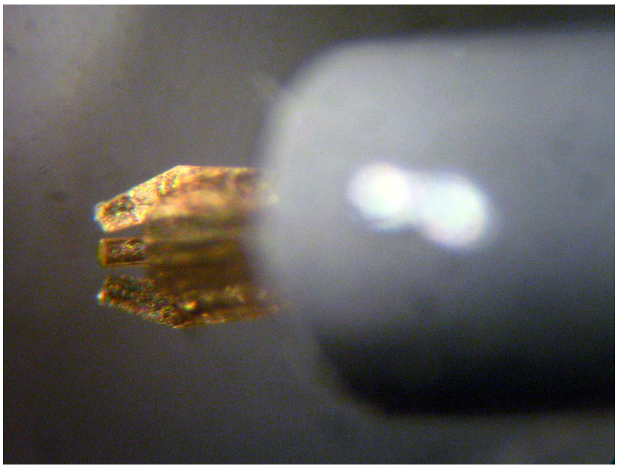

Figure 2.8: 200 [um] pitch Picoprobes for microwave measurements.

The microwave probe tips, Fig. 2.8, were strongly thermally coupled to the room temperature environment, which was an issue during testing as they would significantly increase the temperature of the sample when making contact. To compensate for this, a pair of copper braids for each probe were anchored to the gold plated copper rod by screws and Heli-Coil inserted screw threads and in turn connected to the probe arms. Although this was not enough to bring the probe arms down to T_{LN2} (temperature reaches a minimum of 90 [K]), it does prevent the probe tips from having a high enough of a temperature to raise the samples above T_c when in contact. The probe arms, in addition to the optic fiber probe arm, are controlled with Newport 426A series 3-axis micro-manipulators to adjust their positions for interacting with the DUT. Stainless steel bellows bridge between the flanges and the micro-manipulators, in order to allow movement while maintaining a vacuum seal. The optic fiber probe was a Corning SMF28 fiber that is fed through the probe arm and bent so as to be perpendicular to the sample stage surface. The bending radius was kept large so as to minimize any attenuation. The microwave probe arms are fitted with Picoprobe Model 40A CPW 200um pitch probes from GGB Industries. These probes are quite delicate and any excess pressure or misalignment during measurement could irreversibly damage them. The exterior end of the probe arms are connected to high quality rugged Gore coaxial cables, which maintain very stable profiles relative to differences in temperature or physical bending.

The sample stage is a 2 inch copper puck, designed so as to be screwed into the gold plated copper rod mentioned previously, by the same method used for the copper braids. The two surfaces are the same material and being pressed together with great enough force that no thermal grease is necessary for good thermal coupling. The top of the sample stage had hatch pattern of grooves machined into it similar to that done for the DC copper base, discussed in Sec. 2.1. The hatch pattern serves an additional purpose in this case, as it provides channels for any air trapped beneath the sample to escape when pumping the chamber down to vacuum. Without these any air bubbles trapped beneath the sample by the silver cement could shift the sample or completely dislodge it.

A diode temperature sensor was placed on the gold plated copper rod and another on one of the microwave probe arms. It was found that the copper rod sensor would read a minimum of 77.5 [K] and the microwave probe arm would read roughly 90 [K] after 25/60 minutes from starting the cool down process respectively. The probe arms would need to be manipulated to over the sample stage so that the copper braiding was not in contact with the outer wall of the cryostat, as this would not only increase the cooling time but limit the temperature of the microwave probe until it was repositioned.

It is also important to note the micromanipulators undergo a great deal of stress during use, considering the extreme pressure difference. Proper maintenance and upkeep is essential for continued use, otherwise wear and tear can result in a manipulator slipping and causing the probe arm to be instantly sucked into the cryostat. The top of the cryostat is covered with an inch thick slab of plexiglass and sealed with an o-ring. This allows for viewing of the DUT on the sample stage during measurement with the use of a Nikon SMZ660 stereomicroscope attached to an articulating arm boom stand.

2.3 Wafer Design and Fabrication

The thought process behind the design and over all layout of the wafer was to have appropriate device designs in order to;

- Determine the I$_c$ and T$_c$ of the different microbridge dimensions and meander designs mimicking standard SSPD layouts.
- Measure the S-parameters of the same microbridges and meander designs.
- Measure the change in S-parameters from optical excitation and the photon detection sensitivity based on the previous results.

2.3.1 DC Device Design

As mentioned in Sec. 2.1.2 the contact pads of the DC samples were sized with plans of use of a probing station. This resulted in pads that were only 400 x 400 [um]. In addition neighbouring device contact pads were separated by only 100 [um] in order to fit as many devices on to the wafer as possible so as to acquire numerous useful measurements. The contact resistivity, as again discussed in Sec. 2.1.2, for these measurements was determined by the wire dimensions used for bonding, but the current-transfer voltage was determined by the distance between the current and voltage leads. Even with optimal placement, the maximum distance between the two bonds on the contact pads were 250 [um], though this required them to be on the edge of the pad which often resulted in poor bonding. The minimum distance (x_{min}) between the two leads in order for the voltage lead to avoid picking up any voltage generated by the current lead can be found from

$$x_{\text{min}} = D_{cl} \left(\frac{0.1}{n} \right)^{0.5} \left(\frac{\rho_{\text{m}}}{\rho'} \right) \tag{2.10}$$

where ρ' is the estimated resistivity detection limit of the measurement setup, since if it is not detectable it is of no concern, ρ_{m} is the sample's matrix resistivity, n is an index of the nonlinearity of the sample's intrinsic $V - I$ characteristic ($V \propto I^n$) and D_{cl} is the sample diameter. For a thin film homogeneous sample, the voltage lead should be several strip widths from the current lead to insure the current has completed distributing itself along the thin film. Placement of the leads should also not be near sharp corners or bends as current crowding will cause disproportionate

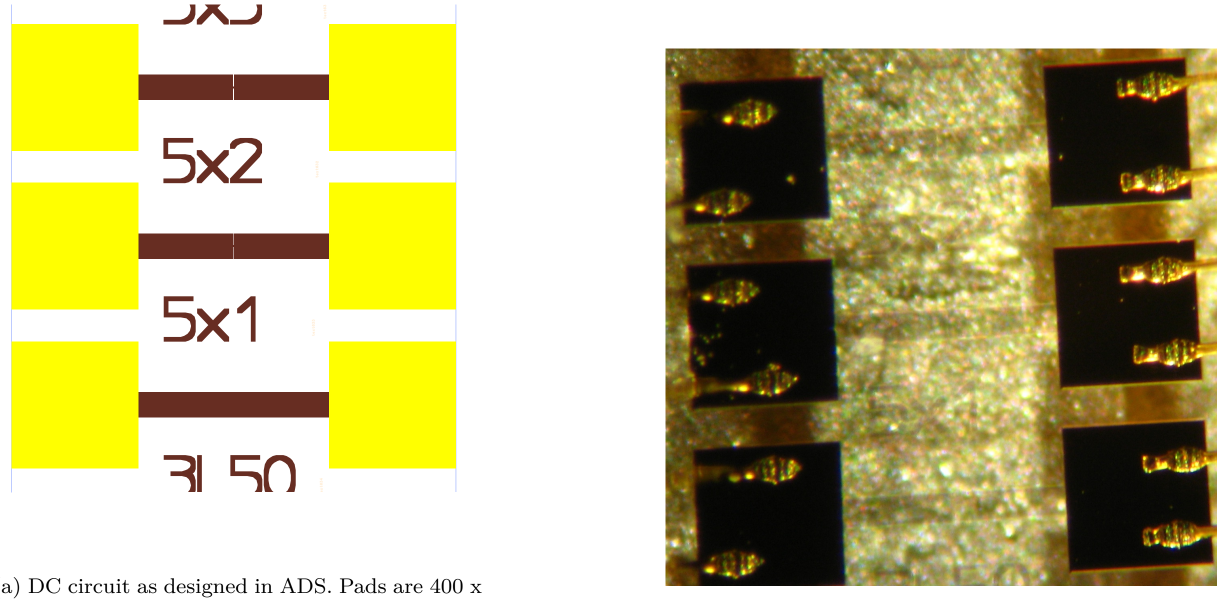

(a) DC circuit as designed in ADS. Pads are 400 x 400 [um], cental line is 80 [um] wide by 600 [um] long.

(b) Fabricated DC Circuits, with wedge bonded contact leads

Figure 2.9: DC circuits for four-point measurements

current distribution at these points [19]. An ideal placement between the two contact leads to avoid any measurable current-transfer voltage for these measurements is roughly 400 [um].

The DC portion of the wafer was designed to be diced to have 15 devices per sample, devices being grouped based on microbridge size or meander design. Each sample contained one 'bulk' strip so as to allow for confirmation of the YBCO devices switching to the superconducive phase in each measurement. The bulk strip also allows comparison of IV sweeps to determine what behaviour that is present in a measurement is due to the device or to any noise voltages such as current-transfer voltage. The listing of the devices can be seen in Table A.1. Backup copies, in some cases up to four, were present on the wafer of some samples, as it was expected that devices could be burned out during testing or fabrication errors could result in damage to some copies of a device. Multiple copies of a device also allow comparisons of measurements to determine the variability of parameters from the fabrication process of a device, such as how much the measured I_c may differ provided all environmental parameters are the same.

2.3.2 Microwave Device Design

To accurately and precisely measure the scattering parameters and minimize any signal delay of optoelectronic measurements of the devices, a well designed transmission line in which to embed said devices into is essential. A coplanar waveguide (CPW) transmission line, two ground plane strips that are equidistant from the center conductor strip as seen in Fig. 2.10, was chosen as it has the benefit of being a planar structure. This results in a simpler fabrication process and allows for the substrates non-fabricated side to be fully thermally coupled to the copper sample base. The dimensions of the CPW had to be compatible with 200 [um] pitch probes of the Microwave Cryostat, such that $s/2 + w < 200$ [um].

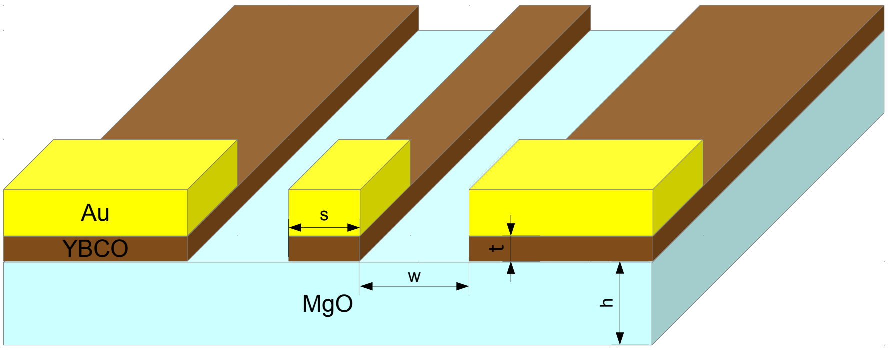

Figure 2.10: Coplanar Waveguide Structure with important dimensions labeled.

The design functions based on the HTS two fluid-model [15], which is simply a modified version of Gorter and Casimir's two fluid model, follows the idea of the temperature dependence of the density of the normal (n_n) and superconducting (n_s) state charge carriers. This can be seen in the empirical relation from (1.2) and (1.3). From this model one can view the circuit as containing a normal fluid channel and superfluid channel, and this approach has been used as a starting point for determing the impedance of a superconducting circuit through the complex conductance [20, 15]. This approach was further expanded for use with CAD modeling by Dr. Mohebbi [21], and is the process used for this work and source of all formula for this section unless otherwise noted.

The surface resistance ($R^t_{s,sc}$) and reactance ($X^t_{s,sc}$) of a superconductor plate can be determined, with respect to temperature (T) and film thickness (t) at angular frequency (ω) by

$$R_{s,sc}^{t} = \frac{1}{\delta_{sc}\sigma_n}\left(\frac{\lambda_L}{\delta_{sc}}\right)^3 \frac{\sinh\left(\frac{2t}{\lambda_L}\right) + \left(\frac{\delta_{sc}}{\lambda_L}\right)^2 + \sin\left(\frac{2t\lambda_L}{\delta_{sc}^2}\right)}{\sinh^2\left(\frac{t}{\lambda_L}\right) + \sin^2\left(\frac{t\lambda_L}{\delta_{sc}^2}\right)} \tag{2.11}$$

$$X_{s,sc}^{t} = \frac{1}{2}\omega\mu_0\lambda_L \frac{\sinh\left(\frac{2t}{\lambda_L}\right) - \left(\frac{\lambda_L}{\delta_{sc}}\right)^2 \sin\left(\frac{2t\lambda_L}{\delta_{sc}^2}\right)}{\sinh^2\left(\frac{t}{\lambda_L}\right) + \sin^2\left(\frac{t\lambda_L}{\delta_{sc}^2}\right)} \tag{2.12}$$

where $\sigma_n(\mathrm{T})$ is the conductivity of the normal channel of the superconductor plate, $\lambda_L(\mathrm{T})$ is the temperature dependent london penetration depth, and $\delta_{sc}(\omega, \mathrm{T})$ is the skin depth of the superconductor in the normal channel and are found from

$$\sigma_n(\mathrm{T}) = \begin{cases} \sigma_0 & \mathrm{T} \geq \mathrm{T}_c \\ \sigma_0(\frac{\mathrm{T}}{\mathrm{T}_c})^\gamma & \mathrm{T} \leq \mathrm{T}_c \end{cases} \tag{2.13}$$

$$\lambda_L(\mathrm{T}) = \begin{cases} \infty & \mathrm{T} \geq \mathrm{T}_c \\ \frac{\lambda_L(0)}{\sqrt{1-(\frac{\mathrm{T}}{\mathrm{T}_c})^\gamma}} & \mathrm{T} \leq \mathrm{T}_c \end{cases} \tag{2.14}$$

$$\delta_{sc}(\omega, \mathrm{T}) = \sqrt{\frac{2}{\omega\mu_0\sigma_n(\mathrm{T})}} \tag{2.15}$$

where σ_0 is the DC conductivity at T just above T_c. Although these do not directly give us the dimensions required for the CPW design, they are necessary to determine as the stored time-averaged magnetic energy and power loss per unit length must be identical to that calculated from circuit theory. This relation allows for determining the series resistance per unit length (R_{sc}) once the kinetic inductance per unit length (L_k) has been calculated.

$$\frac{\mathrm{R}_{sc}}{R_{s,sc}^{t}} = \frac{\omega\mathrm{L}_k}{X_{s,sc}^{t}} \tag{2.16}$$

The geometry dependent equivalent circuit values for the transmission line, as seen in Fig. 2.11, can partially be determined from the standard formula for CPW design, as the shunt capacitance and conductance are not altered by the use of a superconductive material. The shunt capacitance per unit length (C) was found from

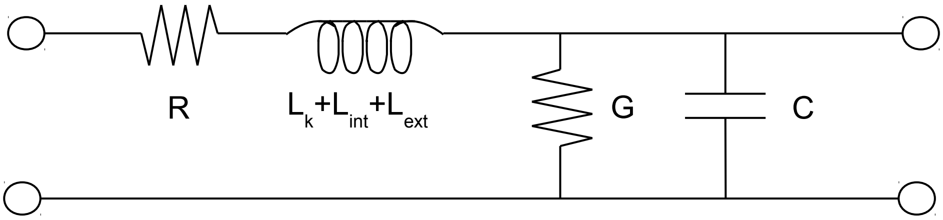

Figure 2.11: Equivalent lumped element circuit model for superconducting transmission line

$$\mathrm{C} = 2\varepsilon_0(\varepsilon_{rd}-1)\frac{K(k_1)}{K(k_1{}')} + 4\varepsilon_0\frac{K(k_0)}{K(k_0{}')} \tag{2.17}$$

where $K(x)$ is the complete elliptical integral of the first kind, ε_0 is free space permittivity and ε_{rd} is the substrate dielectric constant, which for MgO is 9.8. k_0, $k_0{}'$, k_1, and $k_1{}'$ are found from

$$k_0 = \frac{s}{s+2w} \tag{2.18}$$

$$k_0{}' = \sqrt{1-k_0^2} \tag{2.19}$$

$$k_1 = \frac{\sinh\left(\frac{\pi s}{4h}\right)}{\sinh\left(\frac{\pi(s+2w)}{4h}\right)} \tag{2.20}$$

$$k_1{}' = \sqrt{1-k_1^2} \tag{2.21}$$

where s, h and w are the geometric dimensions of the CPW, as seen in Fig. 2.10. The shunt conductance is found from

$$\mathrm{G} = \omega \mathrm{C} q \tan(\delta) \tag{2.22}$$

where $\tan(\delta)$ is the loss tangent of the dielectric substrate and q is the filling factor, in simple terms the measure of the percentage of electric field penetrating the substrate (versus that which is traveling through the air), which is found from

$$q = \frac{1}{2}\frac{K(k_1)K(k_0{}')}{K(k_1{}')K(k_0)} \tag{2.23}$$

The inductance (L) per unit length is found from

$$\mathrm{L} = \mathrm{L}_{ext} + \mathrm{L}_{int} + \mathrm{L}_k \tag{2.24}$$

where L_{ext} refers to the external inductance, which is the magnetic field penetrating the substrate (and air), L_{int} refers to the internal inductance, which is the magnetic field penetrating the superconductor, and L_k refers to the kinetic inductance, which will be described in more detail below and in Sec. 4.1.1. The internal inductance however is disregarded for this design as for film thickness that is half or less the penetration depth results in $\mathrm{L}_k \gg \mathrm{L}_{int}$ [11]. The external inductance, which is also not affected by the presence of a superconductive material, is found from (2.25), where Z_0 is the characteristic impedance of the CPW and C is the shunt capacitance previously calculated.

$$\mathrm{L}_{ext} = Z_0^2 C \tag{2.25}$$

$$Z_0 = \frac{30\pi}{\sqrt{\varepsilon_{ref}^t(f)}}\frac{K(k_0{}')}{K(k_0)} \tag{2.26}$$

The frequency dependent effective dielectric constant ($\varepsilon_{ref}^t(f)$) is determined by initially calculating the effective dielectric constant for a zero thickness conductor at zero frequency, found from the substrates dielectric constant and the previously determined filling factor (2.23)

$$\varepsilon_{\mathrm{ref}}(0) = 1 + q(\varepsilon_{rd} - 1) \tag{2.27}$$

The finite thickness of the film must also be taken into account by

$$\varepsilon_{\mathrm{ref}}^t(0) = \varepsilon_{\mathrm{ref}}(0) - \frac{0.7\left[\varepsilon_{\mathrm{ref}}(0) - 1\right]\frac{t}{w}}{\frac{K(k_0)}{K(k_0{}')} + 0.7\frac{t}{w}} \tag{2.28}$$

From this the frequency dependent effective dielectric constant can be found from the closed-form expression

$$\sqrt{\varepsilon^{t}_{\mathrm{ref}}(f)} = \sqrt{\varepsilon^{t}_{\mathrm{ref}}(0)} + \frac{\sqrt{\varepsilon_{\mathrm{rd}}} - \sqrt{\varepsilon^{t}_{\mathrm{ref}}(0)}}{1 + g\left(\frac{f}{f_{\mathrm{TE}}}\right)^{-1.8}} \tag{2.29}$$

$$g = \mathrm{e}^{u\ln\left(\frac{s}{w}\right)} + v \tag{2.30}$$

$$f_{\mathrm{TE}} = \frac{c_0}{4h\sqrt{\varepsilon_{rd} - 1}} \tag{2.31}$$

$$u = 0.54 - 0.64p + 0.015p^2 \tag{2.32}$$

$$v = 0.43 - 0.86p + 0.54p^2 \tag{2.33}$$

$$p = \ln\left(\frac{s}{h}\right) \tag{2.34}$$

where s, w and t are the dimensions found from Fig.2.10 and c_0 is the speed of light in a vacuum.

The kinetic inductance per unit length can be found by using the conformal mapping technique, and is calculated from

$$\mathrm{L}_{kin1} = \frac{\mu_0 \lambda_L C'}{4A'D'K(k_0)} \times \frac{1.7}{\sinh\left(\frac{t}{2\lambda_L}\right)} \tag{2.35}$$

$$\mathrm{L}_{kin2} = \frac{\mu_0 \lambda_L C'}{4A'D'K(k_0)} \times \frac{0.4}{\sqrt{\left[\left(\frac{B'}{A'}\right)^2 - 1\right]\left[1 - \left(\frac{B'}{D'}\right)^2\right]}} \tag{2.36}$$

where L_{kin1} and L_{kin2} are the contributions from the center line and ground planes respectively. The other parameters are calculated below.

$$A' = -\frac{t}{\pi} + \frac{1}{2}\sqrt{\left(\frac{2t}{\pi}\right)^2 + s^2} \tag{2.37}$$

$$B' = \frac{s^2}{4A'} \tag{2.38}$$

$$C' = B' - \frac{t}{\pi} + \sqrt{\left(\frac{t}{\pi}\right)^2 + w^2} \tag{2.39}$$

$$D' = \frac{2t}{\pi} + C' \tag{2.40}$$

With the inductance having now been calculated, the surface resistance per unit length can be found from (2.16), (2.11) and (2.12).

The film thickness being so low leads to non-ideal microwave performance, as for microwave applications the film thickness should be greater than the effective penetration depth [22], calculated from

$$\lambda_{L,\text{eff}}(\mathrm{T},t) = \lambda_L(\mathrm{T})\coth\left(\frac{\mathrm{t}}{2\lambda_L(\mathrm{T})}\right) \sim \frac{\lambda_L(\mathrm{T})^2}{\mathrm{t}} \tag{2.41}$$

Film thickness below this value causes an exponential increase in surface resistance [11]. $\lambda_L(\mathrm{T})$ is taken from (2.14). Operation near T_c also causes a significant increase in surface resistance and for ideal microwave performance operating temperature should be at or below $\mathrm{T}_c/2$ [11, 20, 23]. Some results suggest operation near T_c causes poor microwave performance due to vortex pair unbinding at high frequencies [24], so operation should at the very least be below the suggested Berezinskii-Kosterlitz-Thouless transition temperature ($\mathrm{T}_{\mathrm{BKT}}$) which is frequency dependent. High input power is also thought to cause a similar effect [23]. The effect of the gold contact pads on the overall impedance was not taken into consideration, though for the devices in question the effective additional surface impedance would be minimal [18], as found from

$$Z_{\text{eff}} \approx Z_{\text{s}} + \frac{\omega\mu_0 \mathrm{t_c}}{2} \tag{2.42}$$

where t_c is the thickness of the cap layer. At 10GHz this generates roughly an additional mΩ to the surface impedance. The resulting dimensions calculated for the CPW design were a center line width (s) of 80 [um] and a spacing (w) of 23 [um]. The ground width was set to 300 [um] and total line length is 4 [mm], which includes a 1 [mm] length of gold at each end as a contact pad. Some variations to these values were included in the designs to determine the validity of this design process, as seen in Table A.1. Neighbouring CPWs have a shared ground line, in order to fit a larger number of devices per sample. The resulting CPW layout can be seen in Fig. 2.12.

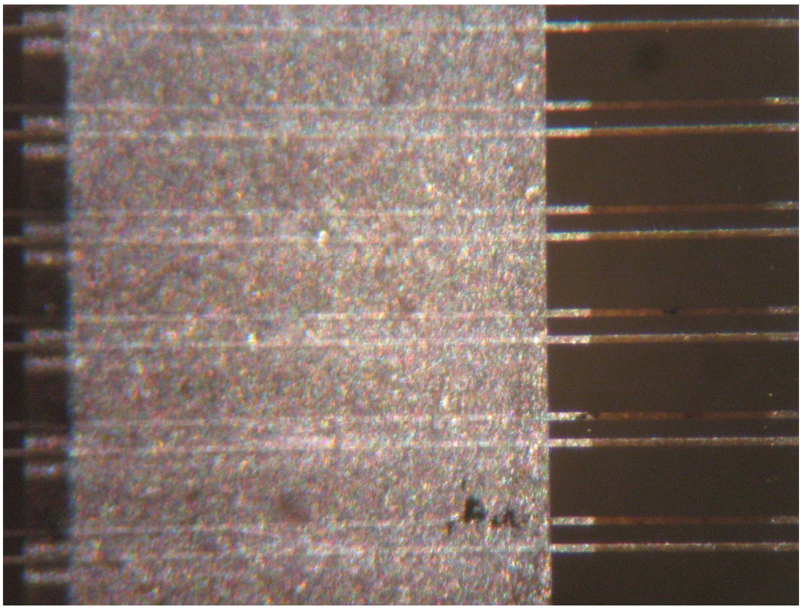

Figure 2.12: CPW layout post fabrication. Dark pads on the right side are gold contact pads. The near transparent film running horizontally is the YBCO thin film.

2.3.3 Fabrication

The wafer substrate is a 500 [um] thick MgO disk, which was chosen as the structural quality and transport properties of $YBa_2Cu_3O_{7-x}$ when fabricated on MgO have shown optimized results, [20], with reasonable thermal conductivity. Though it can suffer from lattice mismatch, as seen in Fig. 2.13, and MgO is a hygroscopic surface. No buffer layer was applied. $LaAlO_3$ and sapphire are other low-loss dielectrics commonly chosen as substrates for YBCO use. Deposition methods most commonly used for YBCO applications are thermal co-evaporation [25, 26], laser-induced evaporation [27], pulsed laser deposition [28, 29, 30], and magnetron sputtering [31, 32].

The YBCO 25 [nm] film deposition for this work was performed by THEVA GmbH by reactive thermal co-evaporation at 680^{o}C in a vacuum chamber, growing epitaxially and c-axes normal

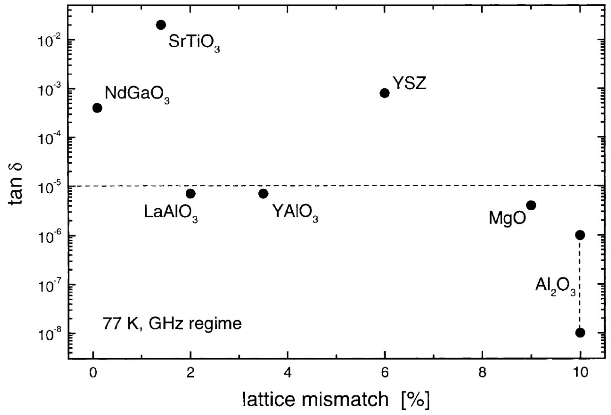

Figure 2.13: Loss tangent vs. lattice mismatch of various substrates with respect to YBCO [22]

to the substrate, resulting in an E-type film. This is a product designation by THEVA implying a rms surface roughness of less than 10 [nm] and typical results of T_c greater than 83 [K] and a critical current density (J_c) greater than 1 [MA/cm^2]. Reported results of this film by THEVA give a T_c of 85.6 [K] and a J_c of 3.1 [MA/cm^2]. This is an unexpected value as a previous 100 [nm] YBCO film from THEVA gave a critical current density of 4 [MA/cm^2], and literature suggests that a decrease of film thickness should increase J_c [33], although when approaching film thickness on the order of single digit number of unit cells, the material strongly diverges from bulk behaviour [34, 25], which could explain the unexpected value of J_c. Reduced film thickness is also known to be more prone to inhomogeneities on the film surface [34], although it is unknown to what degree a-b axes orientation mismatch there might be between different nucleation sites during sputtering.

200 [nm] gold film was applied in situ after cool down in an oxygen atmosphere in order to protect the surface of the YBCO from water vapour and carbon dioxide, as this causes a resistive layer to form on the surface, and results in a lower contact resistance compared to application of a noble metal ex situ [18]. THEVA provided a scanning electron microscope (SEM) image of the film after the deposition process, Fig. 2.14, though it is presumed this is of the gold film since it was applied in situ.

Device patterning on YBCO thin film must be sure to avoid exposure to water, high temperatures and even long exposure to atmosphere as this can cause a change in the oxygen stoichiometry, resulting in a drop in the T_c or even complete loss of the superconductivity [35, 27]. Standard photolithography can be employed when non-fine dimensions are required (on order of 10 [um]) provided care is taken to avoid any of the previously mentioned concerns [36, 30, 31]. This is often paired with e-beam or Ar$^+$ ion milling [28, 37, 29] with the sample being thermally coupled

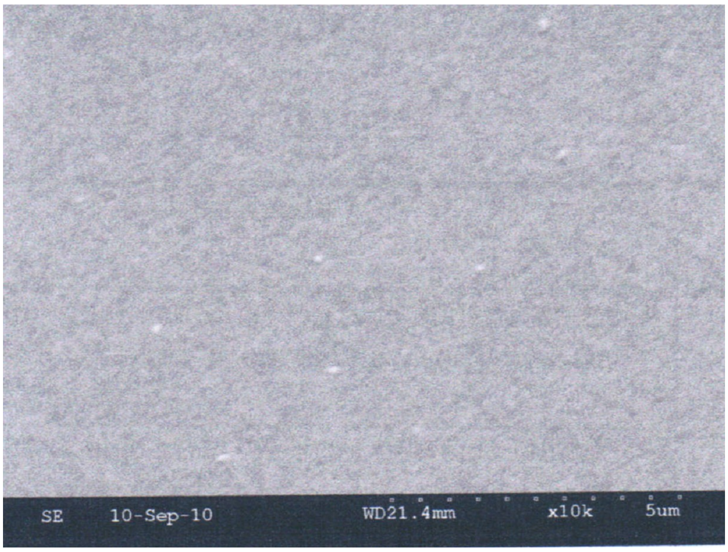

Figure 2.14: SEM of thin film post deposition - THEVA

to a liquid nitrogen cooled (or other heat sink) stage to get to dimensions of the order of 1 [um]. Some newer methods which have proven promising for even smaller dimensions are atomic force microscopy ploughing [32], Superlattice Nanowire Pattern Trasnfer [38], focused ion beam using Ga^{3+} [31, 30] and High-Energy Heavy-Ion lithography by way of generating columnar defects [39, 40]. Many of these methods do require much greater fabrication times and some currently result in inconsistent device quality.

The device patterning for this work was undertaken by Star Cryoelectronics. A complete report on the fabrication methods they use is unavailable as some details are proprietary to Star Cryoelectronics. The initial patterning was done with argon ion milling using a resist mask. To prevent any oxygen diffusing from heating during the milling, the substrate was clamped to an aluminum puck with a small deposit of thermal grease to improve thermal coupling. The puck is filled with a salt that has a melting temperature of 38^{o}C, keeping the sample below any dangerously high temperature. The resist mask is then stripped, allowing a second to be applied for patterning the gold contact pads. The gold is etched with a potassium iodide solution, after which the second resist mask is removed and the entire wafer is cleaned. Following the design file provided to Star Cryoelectronics, Fig. 2.15, the wafer was diced to allow for the samples to fit on their appropriate sample stages. This resulted in 15 DC devices per sample (the southern sections of the wafer) and roughly 50-100 microwave devices per sample (the northern sections of the wafer). The oversized pads seen along the south edge of the equator were added for a simple

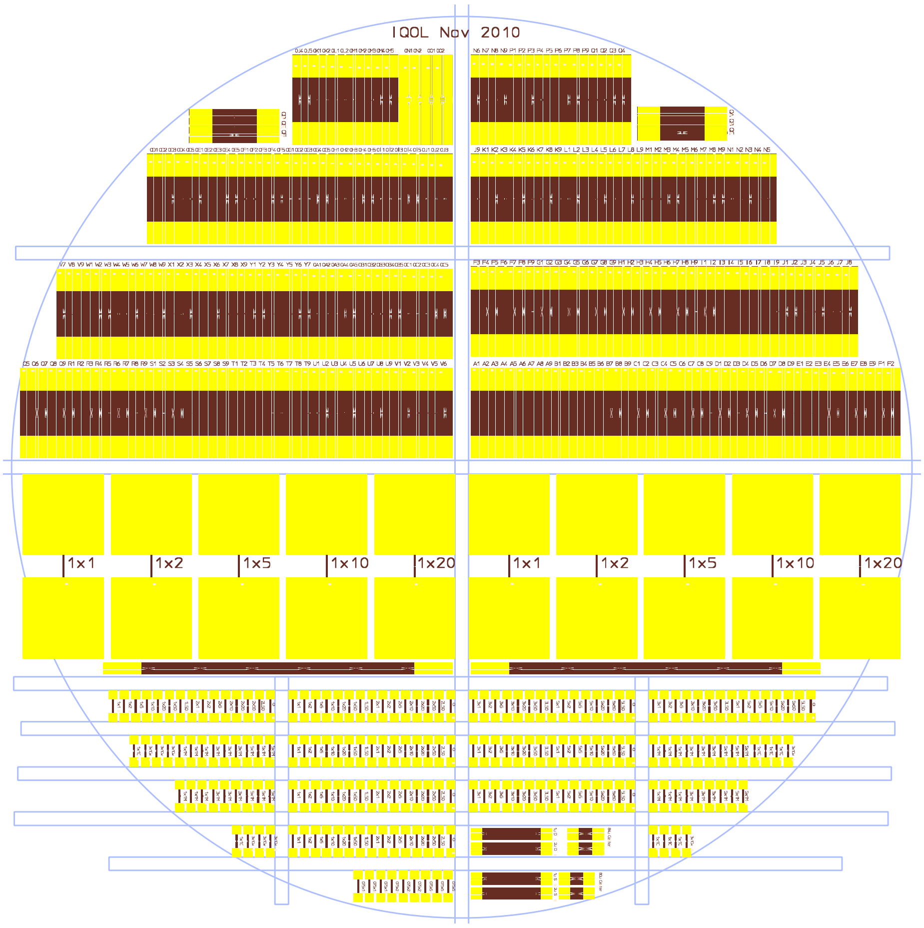

Figure 2.15: Overall wafer design from ADS - some detail missing due to resolution limitation.

measure using toothless crocodile clips, though the bridges for these did not fabricate successfully.

There were some issues with the device patterning that were never fully resolved. Although a resolution of 1 [um] was given as the minimum capabilities of Star Cryoelectronics, a number of components at this resolution failed to fabricate. It was found that short 1 [um] bridges with tapered lines, going from a 80 [um] width to 1 [um] width over a few hundred micrometers, failed to fabricate, though wider bridges generally did, as seen in Fig. 2.16. It was suggested that sharp corners and transitions were a possible explanation for some 1 [um] resolution designs not forming, though this was not a consistent explanation, as seen in Fig. 2.17. It is perhaps possible that the sharp edges of the mask are causing a lensing or scattering effect on the ion beam, [39], such that edges of the design are being milled more than desired, which is only prominent in the case of the very extremes of the resolutions. These issues did not arise when Star Cryoelectronics used the same mask on thin film silicon.

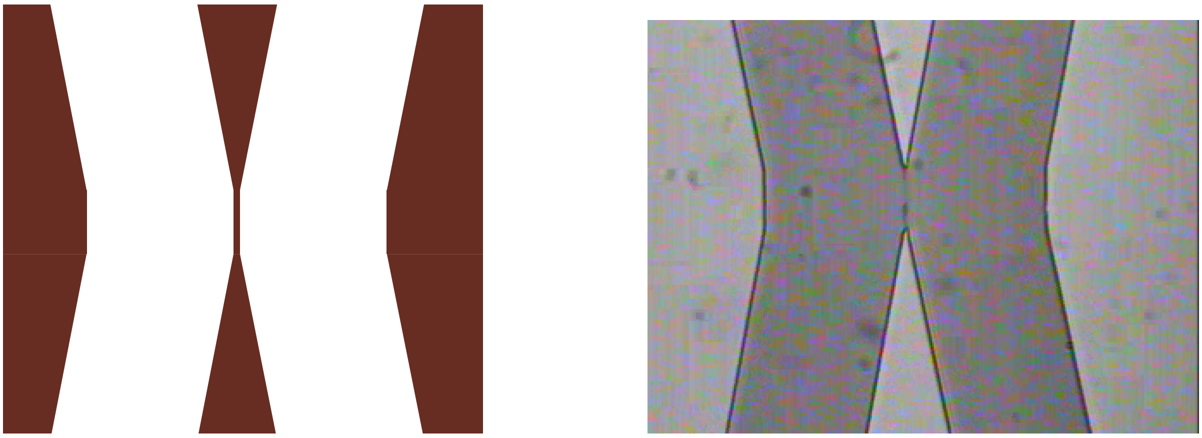

(a) Designed Tapered Line

(b) Tapered Line Result

Figure 2.16: Design vs. Fabrication Result of a 1 x 10 [um] tapered line microbridge

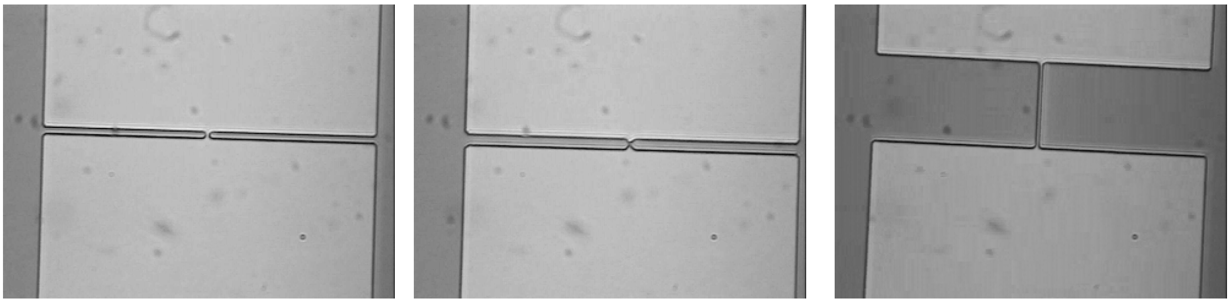

(a) 1um length successful

(b) 2um length unsuccessful

(c) 20um length successful

Figure 2.17: Fabrication results of 1um width micro-bridges

The surface morphology, ignoring the odd artifact from debris, is quite smooth, as seen in Fig. 2.18. The Abbott plot, Fig. 2.19b, shows the cumulative probability distribution of the films surface based on height. Ignoring the initial few percent which are likely due to artifacts/debris, the near constant value suggests a minimal surface roughness (roughly +/- 3 [nm] for 90 percent of the surface). The frequency of this surface roughness is of a concern however due to current crowding, as discussed in Sec. 3.1.

It does seem that overexposure could be partially to explain for fabrication errors, as can be seen from the atomic force microscopy (AFM) scans that were taken of two devices, Fig. 2.20 and Fig. 2.21. The height difference between the top of the YBCO film and the MgO substrate was measured to be roughly 150 [nm] (variance in measurements from 120 [nm] to 180 [nm]). The AFM was recalibrated due to this result being so unexpected, since the film is meant to be 25 [nm], but the height difference remained the same. This strongly suggests the wafer was

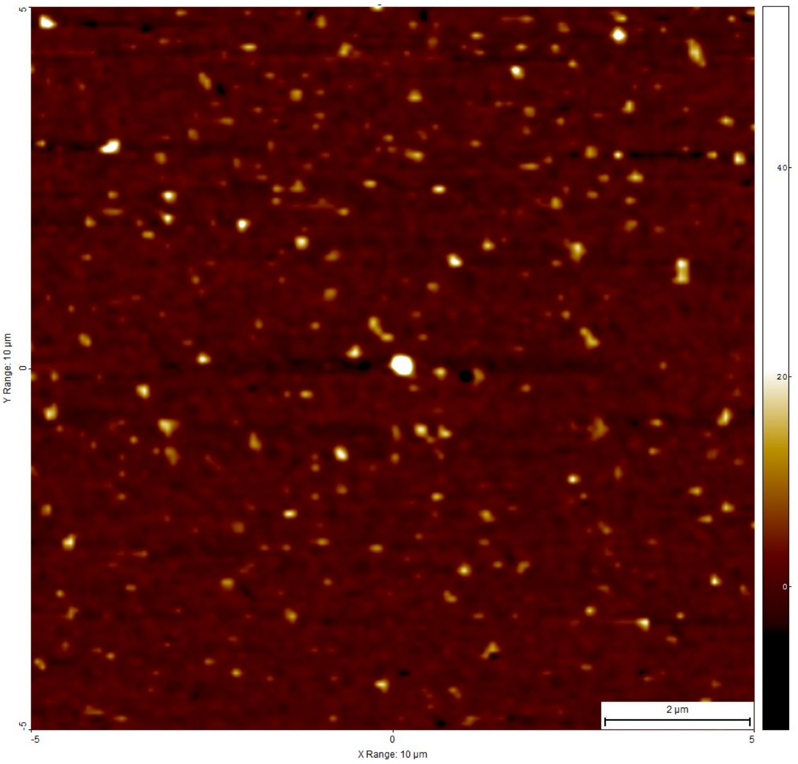

Figure 2.18: AFM of YBCO surface post milling

overexposed to the argon ion beam milling, which resulted in roughly 125 [nm] of MgO being milled away as well. It is difficult to say what else this could entail without more knowledge of Star Cryoelectronics procedures, but dependent on their process, shadow etching might have occurred. This could also explain some of the damaged results of the 1 [um] bridges, in that MgO beneath the bridge was milled away, resulting in a loss of material strength and breaking of the YBCO bridge.

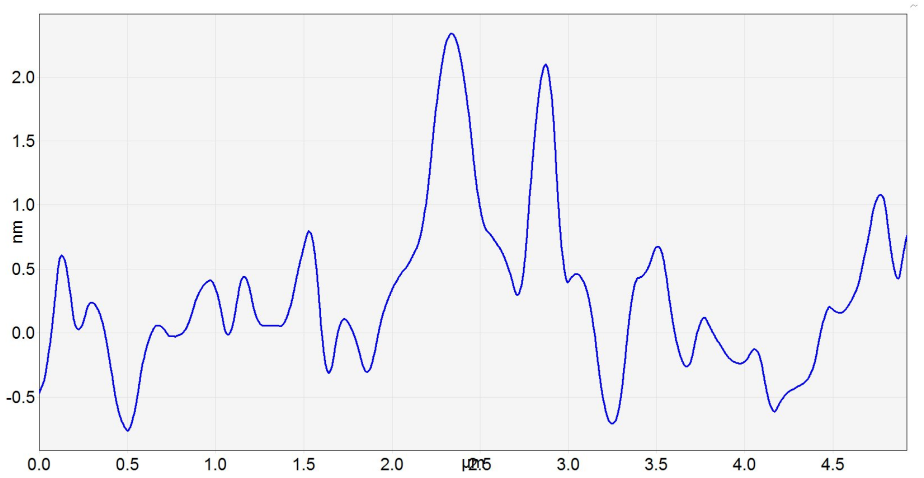

(a) 5 x 5 um averaged cut away of film surface roughness, y-axis averaged film height in nm, x-axis in um

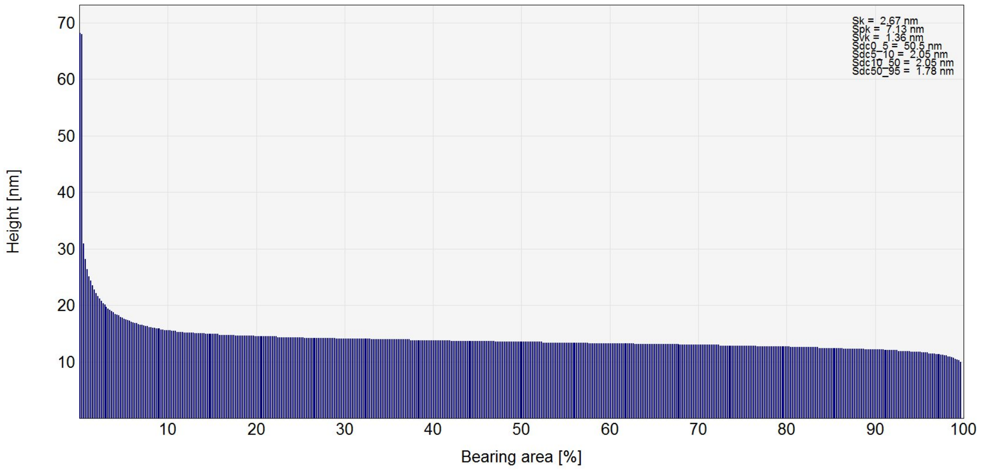

(b) Abbott-Firestone plot of the surface roughness

Figure 2.19: Surface roughness analysis on the AFM scan from Fig.2.18

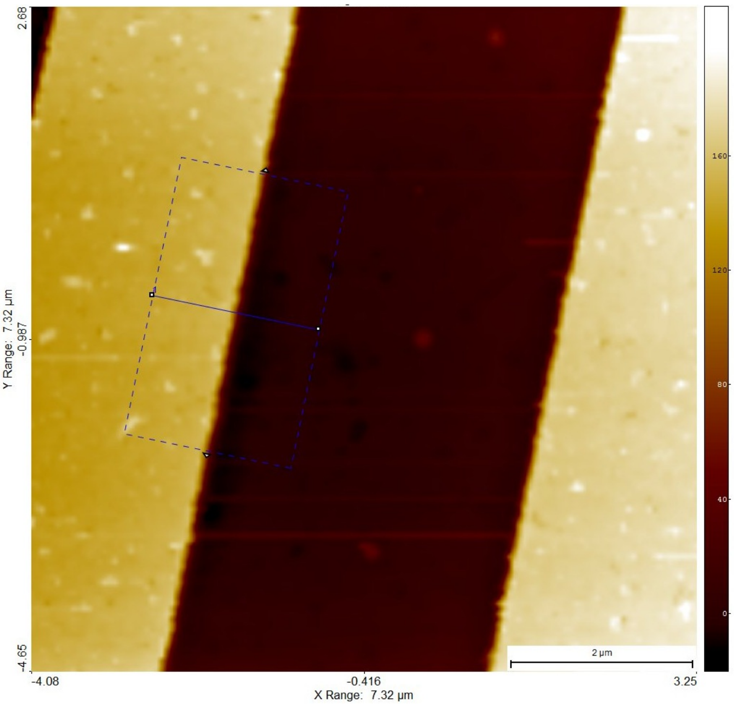

(a) AFM scan of a meander line showing section analyzed for z-axis

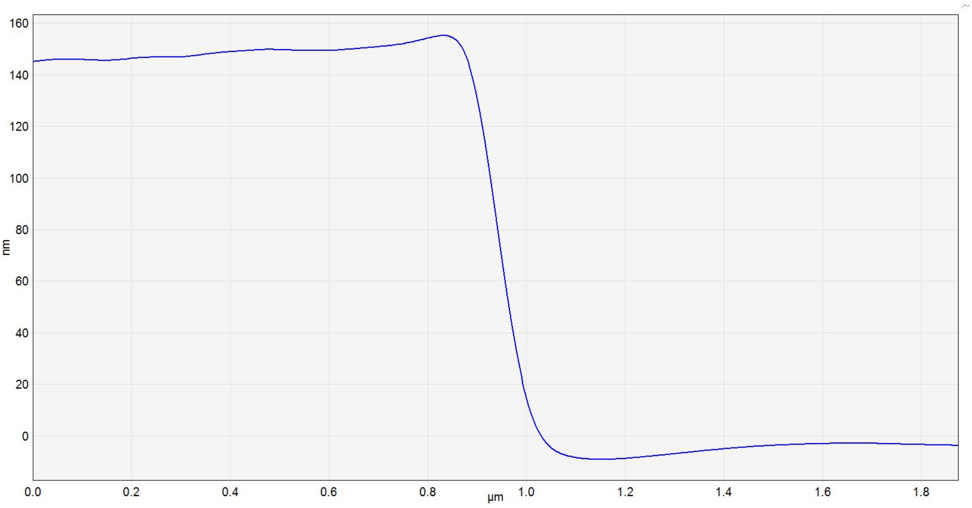

(b) Plot of z-axis (height) averaged over the selected area as seen in (a)

Figure 2.20: Height of film post fabrication. Slight error in global leveling giving overall slant. Gibbs phenomenon explaining the spikes at edges

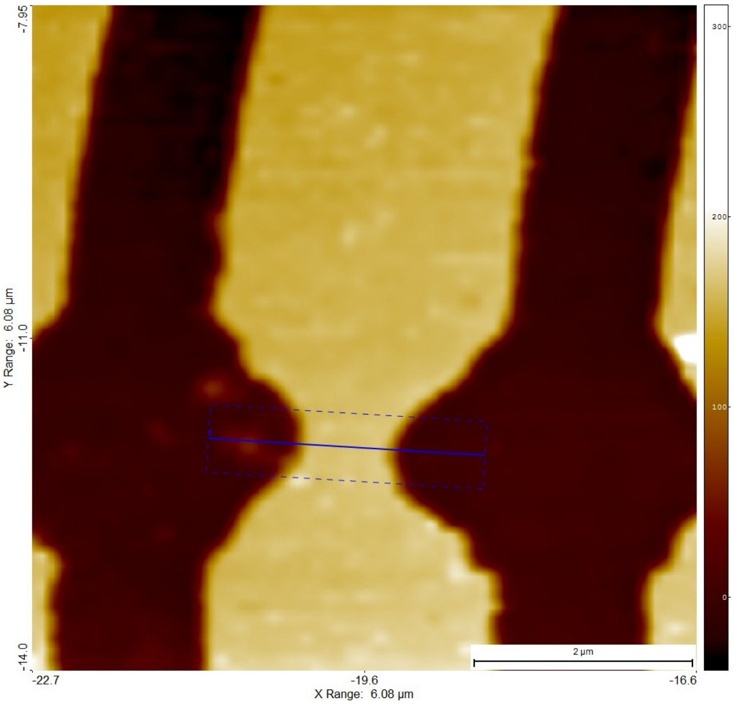

(a) AFM scan of a meander line with microbridge showing section analyzed for z-axis

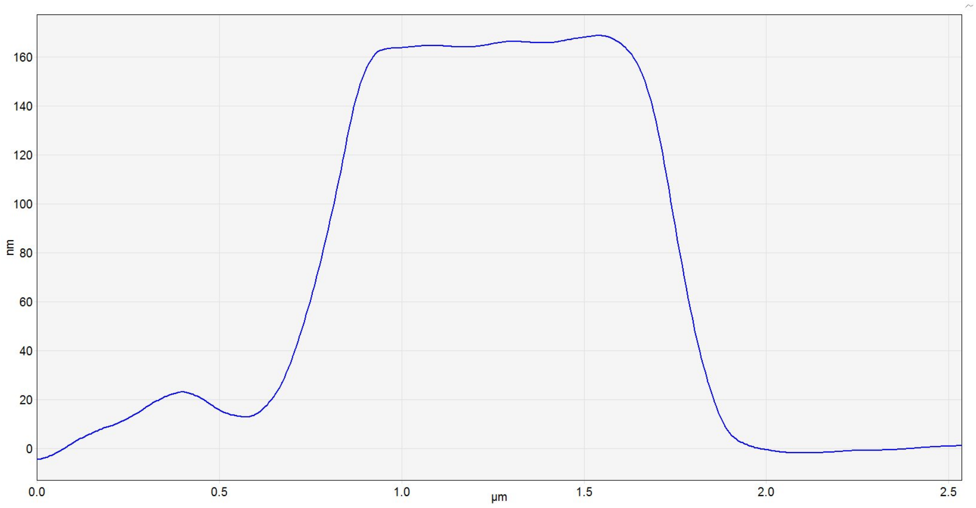

(b) Plot of z-axis (height) averaged over the selected area as seen in (a)

Figure 2.21: Height and width of microbridge post fabrication. Slight error in global leveling giving overall slant.

Chapter 3

DC Measurements

Numerous 4-point measurements have been made on thin film YBCO for the purpose of determining the I_c and DC behavior of various devices. However an accepted means of defining I_c and a review of current theory on possible explanations for device behavior is first required.

3.1 Theory

YBCO unit cell size (measured along c-axis) is roughly 1.17 [nm] [12]. As the film used for this work is only 25 [nm] thick, or roughly 21 unit cells, it can be understood why care must be taken for any analysis that the thin film effect on superconducting parameters is considered. Although the film is not thin enough to fall under the standard definition of 2-dimensional, that $t<\xi$, literature tends to treat film thickness that is significantly below the penetration depth to be in a pseudo 2-dimensional regime [38]. As the film thickness follows $t \ll \lambda_L(T)$, the current density is practically independent of **z** (the axis normal to the substrate) [41, 19]. Furthermore width (w) dimensions that are less than the Pearl length ($w \ll \Lambda$) result in current densities that are nearly independent of **x**. The Pearl length is found from

$$\Lambda(\mathrm{T},t) = \frac{2\lambda(\mathrm{T})^2}{t} \tag{3.1}$$

which is in essence the effective London penetration depth from (2.41). Although the thickness for this and all other calculations used is 25 [nm], the surface roughness as discussed in Sec. 2.3.3

suggests a lower value that accounts for the roughness should be used. For devices which fall under this category, the critical sheet current density ($\mathrm{K}_{c,clem}$), where $\mathrm{I}_c = \mathrm{wK}_c$, can be estimated from work by Clem [41]

$$\mathrm{K}_{c,clem} = \frac{\Phi_0}{\mathrm{e}\pi\mu_0\xi\Lambda} \tag{3.2}$$

where Φ_0 is the magnetic flux quantum, and e is Euler's number. The Ginzburg-Landau approach for determining critical current can not be followed as it was calculated under the assumption both width and film thickness is smaller than both ξ and λ_L. The approach from Clem follows from the Gibbs free energy barrier which prevents the nucleation of vortices. The critical current is the point at which the energy barrier no longer is able to prevent said nucleation, a visual representation can be seen in Fig. 3.1a.

The calculated critical sheet current is for a straight line, and a weighing factor ($0 < k < 1$) must be applied based on the geometry present [19]. $\mathrm{K}_{c,clem}$ does not take into consideration any thermal excitations of vortices over the Gibbs energy barrier, such that any measurements at T>0 will have a measured K_c lower than calculated. It also is primarily considering the formation of Pearl vortices at the edges of the film, with the top of the barrier being the balancing point between the Lorentz force and image force on said vortex, but not considering any vortex-antivortex pairs (VAP) that may form in the film due the presence of a current [44] or thermal fluctuations [28]. It is also for these reasons that the critical current is strongly dependent on available pinning sites in the thin film, such as out of plane edge dislocations which create low angle domain boundaries that naturally form during film deposition [36].

Following the approach used to calculate $\mathrm{K}_{c,clem}$ but considering thermal excitations, it is possible to estimate the IV plot as at high temperature and current the voltage will follow the power law [45]

$$V \propto I^n \tag{3.3}$$

where n is determined from

$$n = \frac{\Phi_0^2}{8\pi^2\Lambda k_B \mathrm{T}} + 1 \tag{3.4}$$

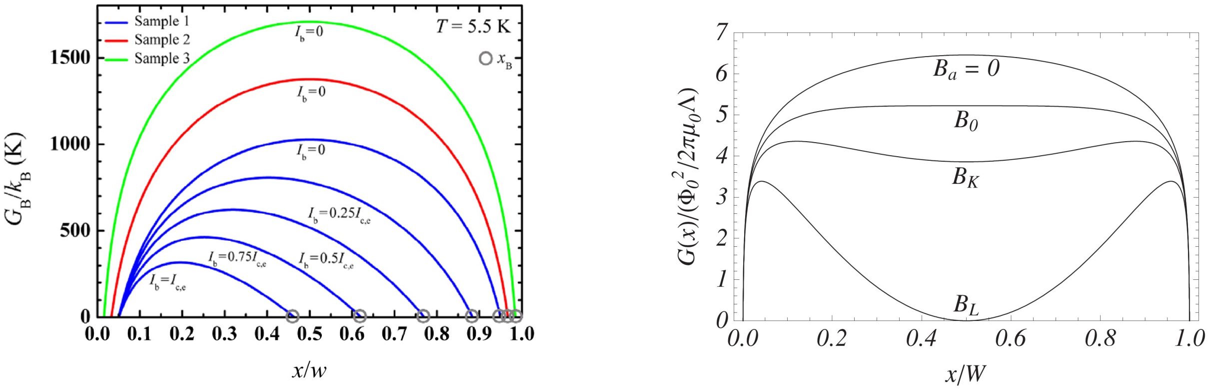

(a) Gibbs free energy along a cross section of NbN meander nanowire at varying levels of bias current; $I_{c,e}$ is the experimental critical current. [42]

(b) Gibbs free energy along a cross section of YBCO in varying levels of applied magnetic field [16]

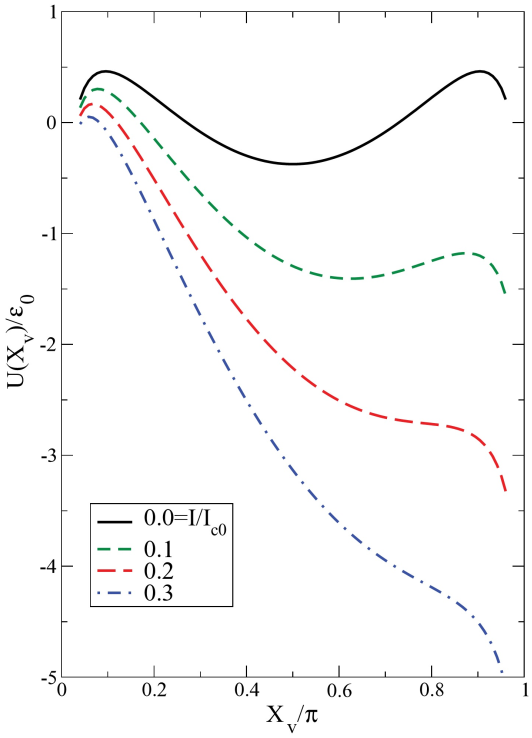

(c) Gibbs free energy along a cross section of YBCO in a magnetic field with varying levels of applied current [43]

Figure 3.1: Gibbs Free Energy

where k_B is the Boltzmann constant. The often seen ‘flux creep’ in IV measurements can be explained by this reasoning. It was found however that calculations of n resulted in unrealistically small values. Brief discussion with Dr. Tafuri lead to the necessity of weighting factors, though it appears these are material specific. All of this analysis however is undertaken considering zero magnetic field. As was mentioned in Sec. 2.1, the lack of mu metal shielding results in the DUTs being exposed to any magnetic fields present in the lab. To determine if the magnetic fields present could be strong enough to cause any noticeable effect on measurements, the temperature and film thickness dependent lower critical field must be calculated from [11]

$$\mathrm{H}_{\perp c1}(\mathrm{T},t) = \sqrt{2}\kappa(\mathrm{T},t)\mathrm{H}_{c1}(\mathrm{T}) \tag{3.5}$$

$$\kappa(\mathrm{T},t) = \frac{2\sqrt{2\pi}\lambda_L^2(\mathrm{T},t)\mu_0\mathrm{H}_c(\mathrm{T})}{\Phi_0} \tag{3.6}$$

$$\mathrm{H}_c(\mathrm{T}) = \mathrm{H}_c(0)\left[1 - \left(\frac{\mathrm{T}}{\mathrm{T}_c}\right)^2\right] \tag{3.7}$$

It is known that for type II superconductors vortices begin to form in fields around H_{c1}, and even more easily when a current is present, as can be easily seen from Fig. 1.1a. The presence of the field also has an effect on the Gibbs free energy barrier as seen in Fig. 3.1b. The value of interest is B_k as it is this strength of field where vortices can begin to become pinned by the field, though this barrier does not inhibit the motion of antivortices [28], and the vortices can of course be thermally excited over this barrier.

$$\mathrm{B}_k = 1.65\frac{\Phi_0}{w^2} \tag{3.8}$$

The unbinding of the vortex-antivortex pairs are also strongly tied to thermal excitations [46], and a great deal of literature arguing that this will occur above the Berezinskii-Kosterlitz-Thouless transition temperature in 2-D thin film superconductors [25, 46, 47]. Below T_{BKT} VAPs remain trapped and do not contribute to the resistance of the device, resulting in a voltage-current characteristic as described previously by the power law relation, above T_{BKT} the VAPs will contribute a linear resistance [46].

It is not fully certain if this is applicable to the devices for this work as the precondition for BKT transition is logarithmic intervortex interaction which will not occour on an insulating substrate no matter the size of the film [47], but would be present in layered compounds due to the pancake vortices (2-D vortices) logarithmic interaction while suppressing Josephson coupling [48]. Even though YBCO is highly anisotropic and can be somewhat thought of as a layered system (from the CuO planes), not much work has looked at BKT transitions in YBCO in a non-layered system. Kuzmichev, [49], has shown what is believed to be evidence of BKT transitions in single crystal YBCO, while other work suggests for thickness above 10 [nm] it is not present [31].

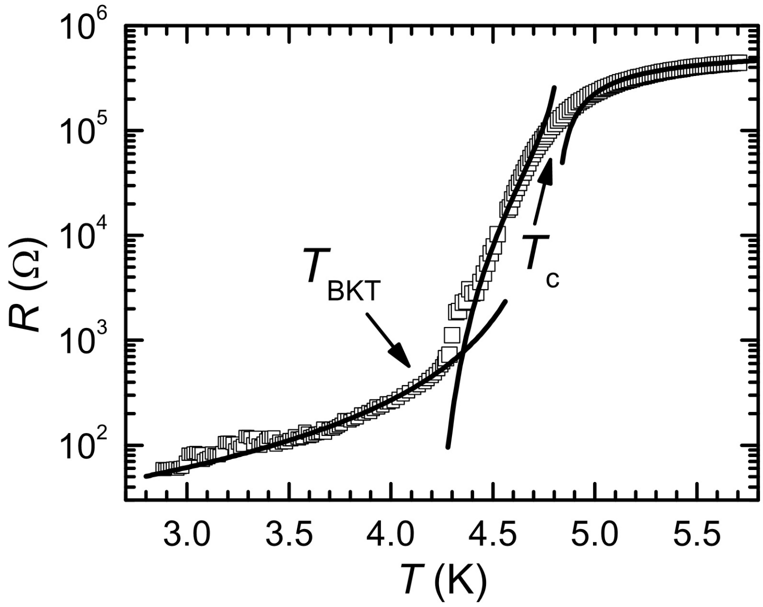

Figure 3.2: Examples of resistance-temperature plot showing both the critical temperature and the Berezinskii-Kosterlitz-Thouless transition temperature [50]

Not only would any BKT transitions effect the behavior of IV measurements, but would also have an effect on resistance-temperature measurements. It is known that narrow constrictions can have a drop in T$_c$ compared to bulk and that film thickness also lowers effective critical temperature [39, 25, 38], in addition to a broadening of the transition temperature range. The onset temperature at which superconductivity starts does not shift significantly from bulk however.

The hotspot model may also provide insight into IV behavior of the devices. As that the initial cross section which switches into normal phase will generate a hot spot, which as current increases, and in turn voltage across this hot spot, will result in the hot spot growing until the entire device has switched to normal phase. The nucleation point for the hot spot will be at the narrowest, or weakest point of the device [51], which if the device has a constant width, will be at any bends or internal corners [41], and has been shown visually [52].

Although this theory gives a means to estimate the behaviour and provide possible explanations for such, an approach to accurately analyze measurement data must be decided upon. For determining the I_c of a device, Ekin provides three criterion from [18]. Fig. 3.4 provides examples of the application of each criterion.

1. Electric-field criterion - A critical voltage level is chosen such that the critical current is the current which drives the DUT to cross this voltage. The electric field can be determined from the length of the superconductor between the two voltage taps. For measurement of short samples, such as micro-bridges, the critical voltage is generally chosen based on the noise floor of the experiment. A generally defined standard value in literature is 1uV/cm, though for most experimental setups this is below the noise floor and must be modified [31].
2. Resistivity criterion - A resistivity is chosen such that the critical current is the current at which the IV curve intersects the resistivity line. This criterion is primarily used for engineering of superconductor magnets.
3. Offset Criterion - A variation of the Electric-field criterion, the crossing point of a chosen critical voltage of the IV curve of the device is used. The tangent of the IV curve at this point is determined and it is the intersection of this tangent line with the current axis which defines the critical current.

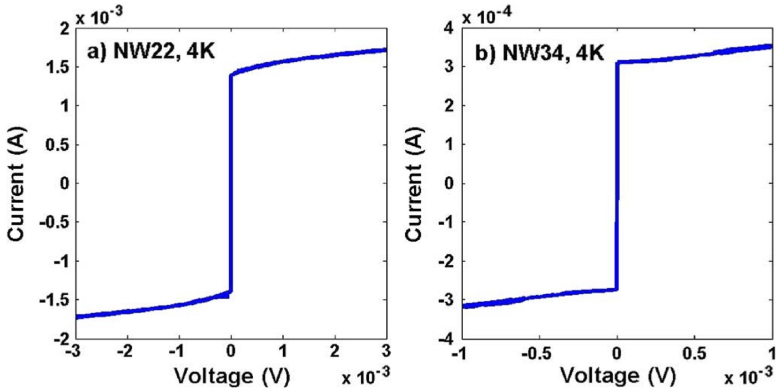

Figure 3.3: Plot of two thin film YBCO bridges IV behaviour: a)Flux Flow like b)RCSJ like [37]. Differention between the two based on plot curvature just after I_c is reached.

For highly nonlinear IV characteristics, criterion 1 and 3 give nearly the same I_c. The nonlinearity tends to be constant for a magnitude change of voltage or greater [18], and can be reasonably modeled following the same power law (3.3) as discussed previously. Analyzing the dR/dI plots of measurement data can also be beneficial as although this does not directly provide the critical current, it can provide better insight as to ideal biasing current levels for detection purposes.

Nawaz has proposed a method for designating between the different IV behaviour of a thin film bridge [37]. It can be determined if a bridge has flux flow like current-voltage characteristic or Resistively Capacitively Shunted Junction like current-voltage characteristic, as seen in Fig. 3.3. If the bridge is flux flow like, observation of Shapiro steps under the right applied microwave radiation will occur, as it is the coherent flow of vortices causing these steps, as also seen in [44].

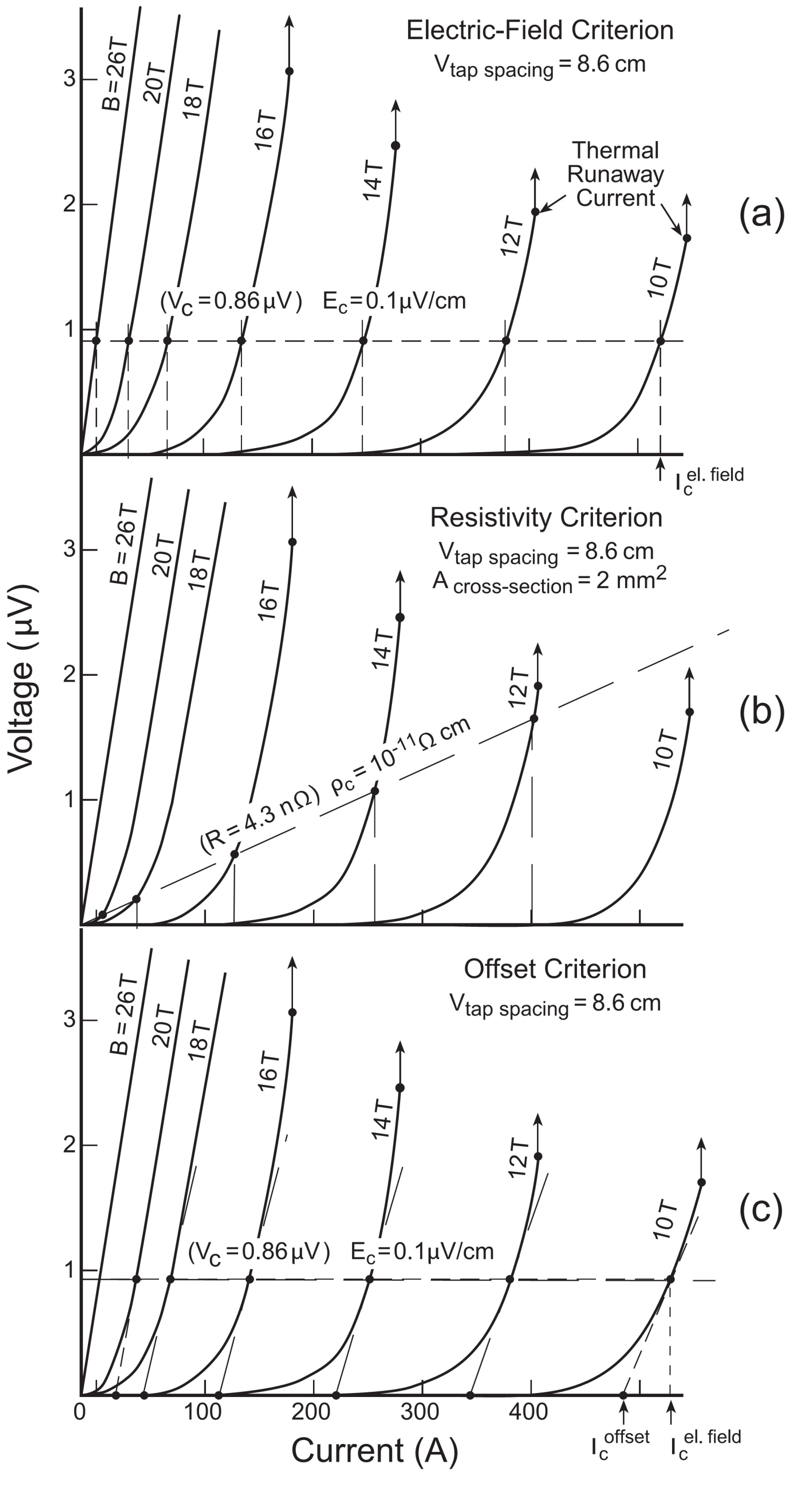

Figure 3.4: Examples of implementations of the three different criterion for determining critical current: a)Electric-field b)Resistivity c)Offset [18]

3.2 Measurements

The dipper probe, as discussed in Sec. 2.1, was used for the DC measurements. The samples which had previously been prepared on a PCB, Sec. 2.1.2, were screwed into the copper sample holder after a small amount of thermal grease was applied to the base surface. The blackbody shielding and electrical connectors were then attached, while keeping grounded to avoid any static discharge damaging the sample. The interior cavity of the dipper probe was filled with helium gas. The copper base and blackbody shielding was then inserted into the dipper probe and screwed into place. The dipper probe was then clamped into an aluminum holder which was screwed onto a floating optical table. The electrical wiring was attached to the sourcemeter, temperature controller and universal ground. The sourcemeter and temperature controller were in turn attached to a GPIB controller, through which Matlab programming using SCPI code would run automated IV sweeps and resistance-temperature measurements.

3.2.1 Resistance-Temperature Measurements

For RT measurements, the dipper probe would be slowly inserted into the LN2 filled dewar, during which a small bias current would be fed to the DUT and the voltage and temperature would be measured. Initial measurements were yielding highly improbable RT curves, with it being explained due to poor temperature sensor placement. The new placement, much closer to the sample, resulted in more accurate RT measurements. Some discrepancies were still present, but using the T_c of the bulk as measured by THEVA allowed for these minor errors to be compensated for.

The key data of interest from the measurements are the T_c of the DUT, the normal resistance R_n, if any BKT transition was present and if there was any change in transition temperature compared to bulk measurements. Fig. 3.5 shows the results of measurements on a bulk line, a 2x50 [um] bridge, and a 5 [um] width circular meander. It can be seen clearly in Fig. 3.6 that a narrowing of the line causes a drop in the T_c of the device and an increase in the transition temperature range. The temperature at which the devices initially begin to transition to superconducting phase appears to be the same. If the THEVA value is taken as correct and the measurements are modified as such, the T_c of a 5 [um] width device becomes 84.4 [K] and a 2 [um] width device to 82.9 [K]. Measurements for other device dimensions were made, but as mentioned in Sec. 2.1, improper temperature sensor placement was giving poor results. As a result more measurements are needed for improved accuracy and to cover all devices. R_n is taken

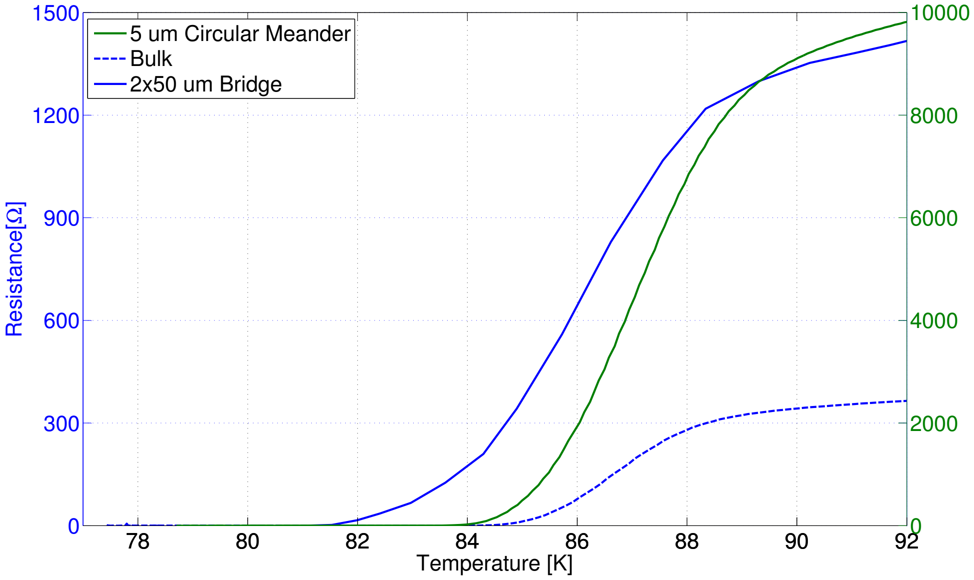

Figure 3.5: Resistance - Temperature Measurement of three different devices.

based on the resistance of the bulk measurement just before the onset of the superconductive phase change, and used to determine ρ_N as seen in Table 3.1.

No clear indications of T$_{BKT}$ was present in these resistance-temperature measurements, however a possible sign of it was seen in the RT measurement of a 1 [um] width circular meander in a helium dipper probe setup. The temperature sensor location provided inaccurate temperature values, but the slope of the measurement treating the temperature as relative gives some interesting results. From IV measurements discussed in Sec. 3.2.2, it is known the device is still resistive at T$_{LN2}$, which if compared to the relative temperature scale and resistance value on Fig. 3.7, puts T$_{LN2}$ at roughly 120. This also suggests that the possible T$_{BKT}$ seen in the plot is below T$_{LN2}$.

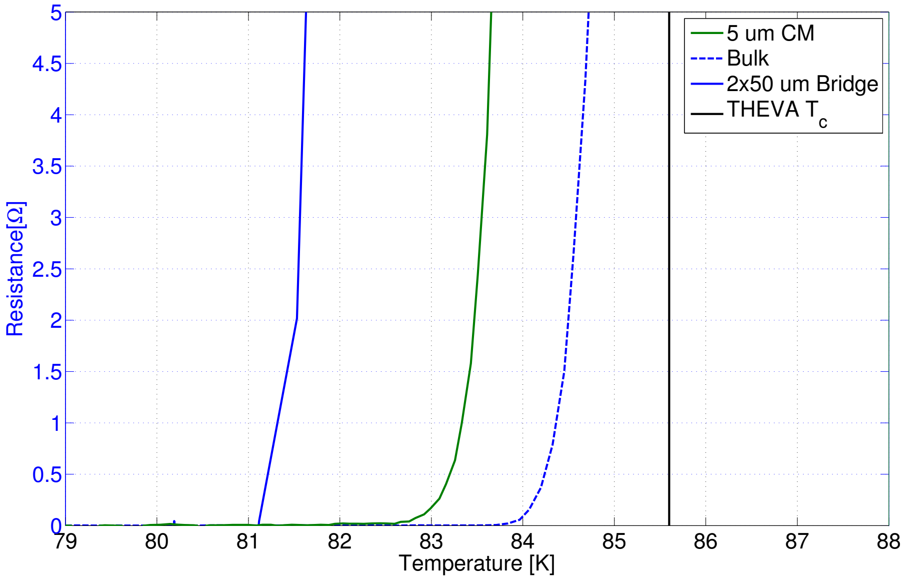

Figure 3.6: Resistance - Temperature Measurement of three different devices showing T_c of each device and $T_{c,THEVA}$.

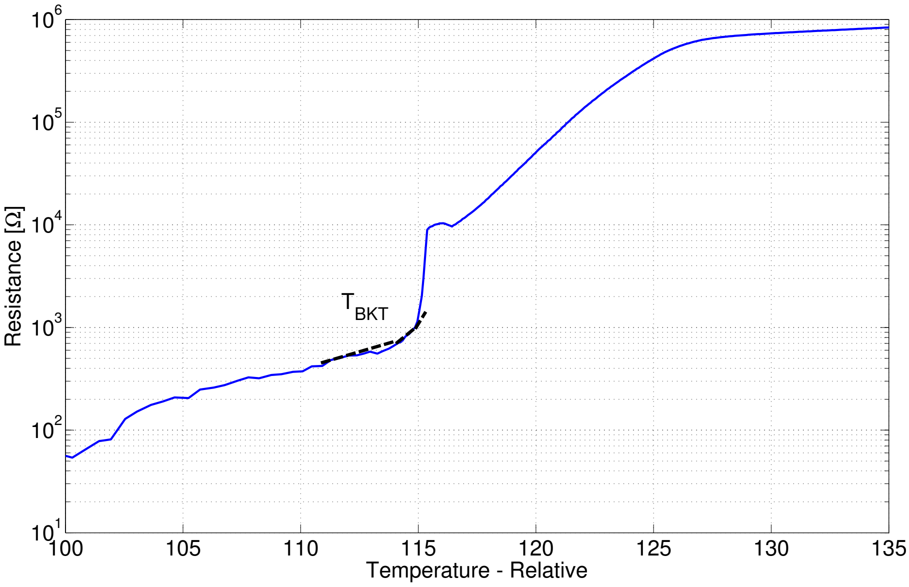

Figure 3.7: Resistance - Temperature Measurement of a 1 [um] width circular meander line. Due to temperature sensor placement temperature values are not absolute and are shown merely for relative change. Suspected T_{BKT} point shown.

3.2.2 Current-Voltage Measurements

As discussed in Sec. 3.1, some useful values for analysis can be calculated based on parameters and dimensions of the devices under test. The results of can be seen in Table 3.1 and Table 3.2. The weighting factor to apply to K_c is non-consistent, as it depends on the device geometry and even then experimental work has values much different from those suggested by theory. For 90^o sharp corners theory from [41] suggests a factor of 0.33, though experimental work from [19] found a better fit at 0.51. The critical current density measured by THEVA, $J_{c,THEVA}$, can also be used to give an estimate on the critical current of a device, though it is unknown at what temperature THEVA measured the bulk thin film. If it was measured at a $T \ll T_{LN2}$, measurements in this work will not compare.

Table 3.1: Values for DC Analysis - a)From National Oceanic and Atmospheric Administration's online database

$\xi(77.5[K])$	10 [nm]
$\Lambda(77.5[K], 25[nm])$	10 [um]
$K_{c,THEVA}$	0.775 [mA/um]
$K_{c,clem}$	1.927 [mA/um]
$B_{c1}(0)$	18 [mT] [53]
$B_{c1}(77.5[K], 25nm)$	225 [mT]
B_{Earth}	51.2 [uT] $_a$
ρ_N	1.17 [uΩm]

Table 3.2: Values for DC Analysis dependent on device width

Line Width [um]	1	2	3	5	80
$I_{c,THEVA}$ [mA]	0.775	1.550	2.325	3.875	62
$I_{c,clem}$ [mA]	1.927	3.854	5.781	9.635	//
Weighted $I_{c,clem}$ [mA]	0.636	1.272	1.908	3.180	//
Weighted-Hortensius [mA]	0.983	1.966	2.948	4.914	//
B_k [uT]	3412	853.0	379.1	136.5	0.53

The measuring algorithm used evolved throughout the measurements, beginning with a simple for-loop to drive a current at set step size and measure voltage, to a semi-automated system as seen in Fig. 3.8. Some attempts at fine step size control were implemented, but noise levels would often result in runaway step sizes.

The 'bulk' devices, 80 [um] wide lines designed to match the center lines used in the CPW devices, gave fairly standard IV curves, as can be seen in Fig. 3.9, showing the measured I_c. Using

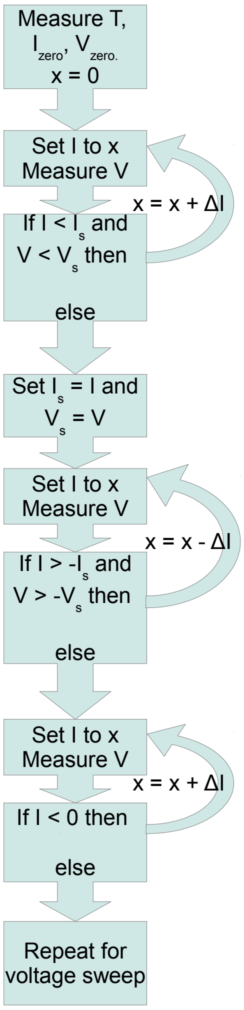

Figure 3.8: Finalized measurement algorithm used in Matlab and with SCPI code

the critical voltage of 2 [uV] (based on noise floor of instrumentation, giving a critical electric field of 20 [uV/cm]) an average I_c of 25 [mA] was measured. This is much smaller than would be suggested from the critical current density provided by THEVA, as seen in Fig. 3.10. Fig. 3.9 shows an example of linear Current-transfer voltage, and a zero-offset, with sample 1. Sample 2 and 3 are examples of the average behaviour of the bulk devices. Fig. 3.10 gives examples of cases of thermal runaway, and switching effects. In addition the plots showing the average upper and lower bounds of the IV characteristics are shown. These were plotted following the power law form discussed in [18], with $n_{lower} = 11$ and a fitting parameter of 10^{13}, and $n_{upper} = 10.5$ and a fitting parameter of $10^{11.8}$. This primarily provides evidence that this behaviour is not due to the presence of nonlinear current-transfer voltage, as this is found at values of n between 1 and 6.

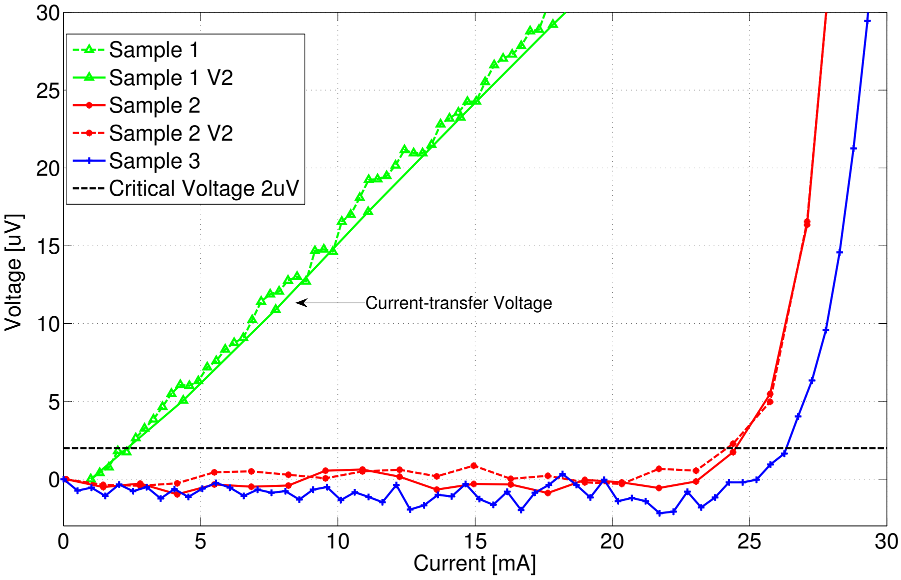

Figure 3.9: IV Plots of Bulk (80 [um]) lines for determining of I_c. Multiple samples (1,2,3) measured, some of which were measured multiple times at different time periods (designated with V2). Critical voltage level also shown. Sample 1 portrays current-voltage error.

The I_c from bulk gives a critical sheet current of 0.312 [mA/um]. Why this is such a significant amount below that measured by THEVA is unknown, though perhaps if their measurement was based on a very narrow bridge sample of the film, as it is known that shrinking of bridge width increases the critical current density [30].

It is also possible that the presence of Earth's magnetic field, which is much higher than the

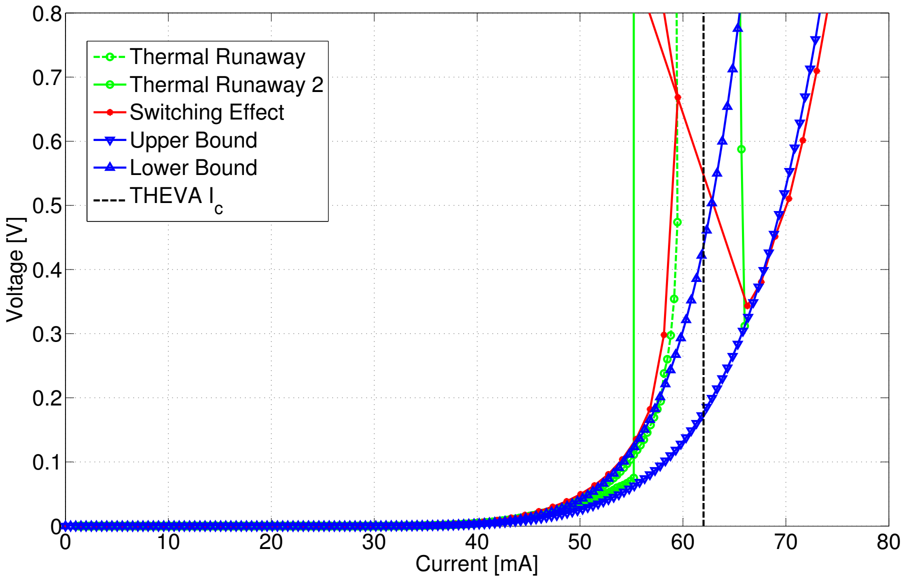

Figure 3.10: Bulk IV showing expected I$_c$ from THEVA J$_c$, average IV behaviour and examples identifying problem measurements.

B$_k$ for 80 [um] width as seen in Table 3.1 and 3.2, that the trapped vortices which are present could be the leading factor for the early voltage onset, and the possible reason for the relatively low n values of the fitting plots, as good quality superconductors should be in the range of 20 or greater [18]. The device is certainly in the Meissner state as B$_{Earth}$ < B$_{c1}$.

The I$_c$ of the 5 width bridges can be seen in Fig. 3.11 and as can be seen it ranges between 1.3 [mA] and 1.8 [mA] based on bridge length which is inversely proportional. Possible explanations for this behaviour are that as a bridge becomes longer, there is greater chance for fabrication errors, constrictions along the bridge or misalignment of ab axis of neighbouring nucleation sites during deposition. However minor defects would act as pinning sites for vortices and actually increase critical current. If this is the explanation then these defects must be rather abundant, since it is such a clear-cut relation between the measured I$_c$ and bridge length, as seen in Fig. 3.13a. There are outliers amongst the measurements, which suggest these are devices that have altered I$_c$ due to damage of some kind. The other possible explanation is the actual I$_c$ being even lower, but it is not detectable due to the noise limitations of the equipment in use.

If this is the case, the separation of IV behaviour that is seen between the different lengths would simply be due to the increased number of vortices present in the line. As it starts to transition into the normal regime the variance based on length is merely due to increased normal

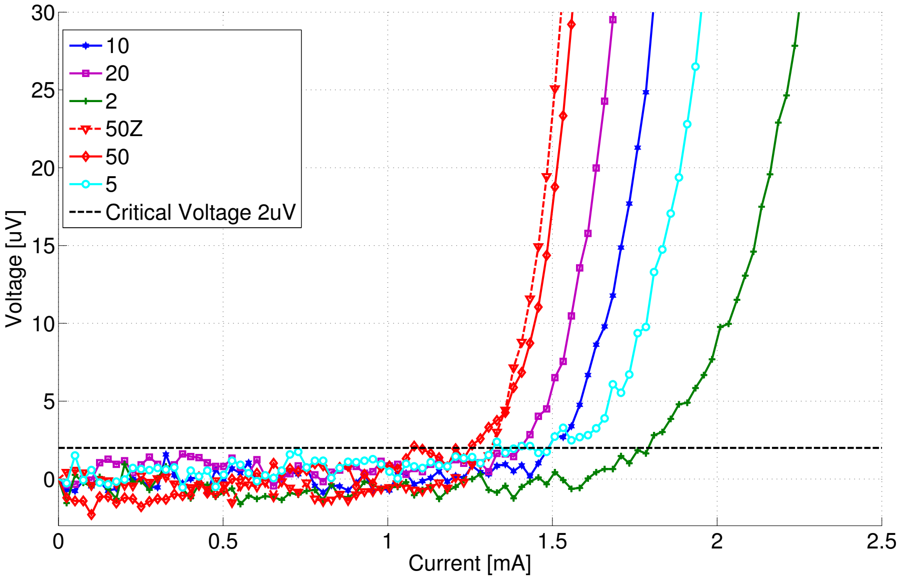

Figure 3.11: IV Sweeps of 5 width microbridges by X length [um]. Clear relation between length and I_c can be seen.

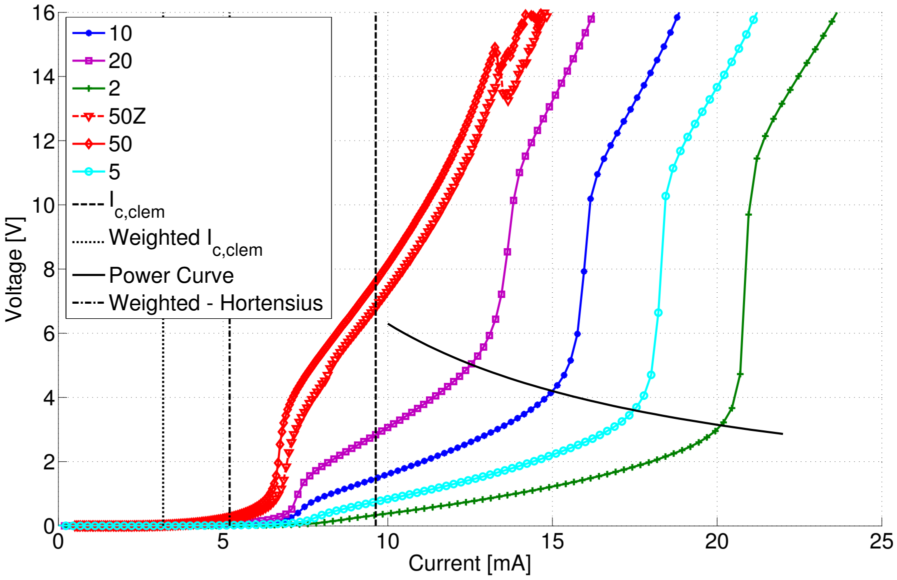

Figure 3.12: High voltage measurement of 5 width microbridges by X length [um]. Theoretical I_cs and power line shown.

resistance, as seen in Fig. 3.12. This is of course working on the definition of critical current which results in a detectable voltage across the device, rather than the device transition into normal phase, as the detectable voltage is that being generated by the vortex motion due to the Lorentz force rather than any actual resistance. When the device has transitioned into normal phase can be determined based on any hysteresis behaviour, as seen in Fig. 3.13c, as the hysteresis is likely due to hotspot generation [52].

The observed critical current values are far below those calculated from the theory, though this bridge width is not significantly less than the Pearl length and so is not a completely uniform current distribution. This may account for some of the lower than expected I_c. It may be that a greater weighing factor is required as the transition from the 80 um center line to the microbridge is a much larger change in width than was analyzed by Clem. Taking an average I_c of 1.5 [mA] gives a weighting factor of 0.156. The weighting factors as determined for the other bridge widths can be seen in Table 3.3. Attempts at fitting models following the methods proposed by Tafuri [45] were made, but were unsuccessful as determination of the weighting factors would require measurements at multiple temperatures.

Table 3.3: Measurement results for different microbridge widths.

Line Width [um]	2	3	5	80
I_c [mA]	0.2	0.62	1.5	25
Weighting factor - measured	0.052	0.107	0.156	//

Analyzing the resistance behaviour of the microbridges at high voltage can help explain the visible behaviour as seen in Fig. 3.12. The R_n for the microbridge and the 80 [um] central line can be determined and compared to measurement results to confirm if it is merely the components transitioning into normal phase, even though current is below the measured I_c for the 'bulk' line. From the calculated ρ_n the expected R_n for the bridge is found to be 188 Ω, shown on Fig. 3.13b.

The normal resistance of the microbridge increases due to joule heating from the increased current, generating higher temperatures. This higher temperature will also start to bleed into the central line, which is likely the cause for the entire line transitioning into normal phase at a lower current than seen previously. This could also explain the reason as to why there seems to be an inverse relation between microbridge length and current point which causes a full normal phase transition, as the higher resistance causes larger power consumption, which can be seen in the power curve plotted in Fig. 3.12. At roughly 63 [mW] the entire device begins to switch into normal phase. The reason for the odd behaviour seen with the 50 [um] length bridges at high voltage is unknown, and was not pursued due to such high voltages likely burning out the DUT.

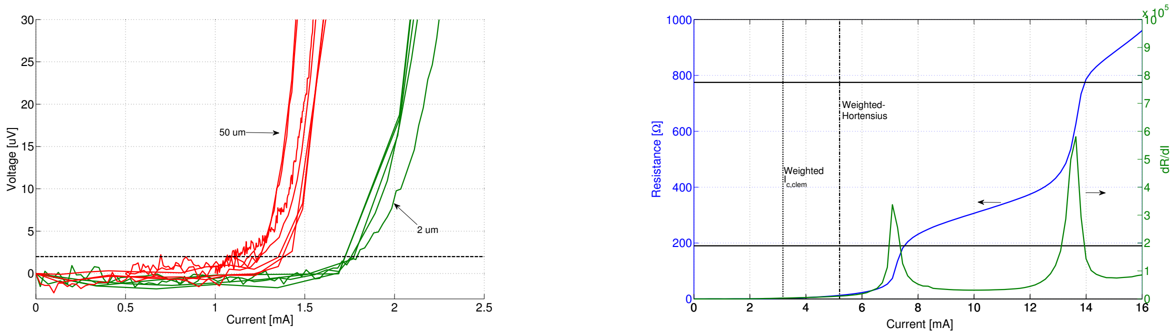

(a) Comparison of I$_c$ of 5 width microbridges by 50 and 2 length [um]. Multiple different sample measurements are shown. Correlation between I$_c$ and bridge length clearly seen. Critical voltage line (black-dashed) shown.

(b) High voltage measurement showing resistance line for the bridge (lower) and entire device (upper).

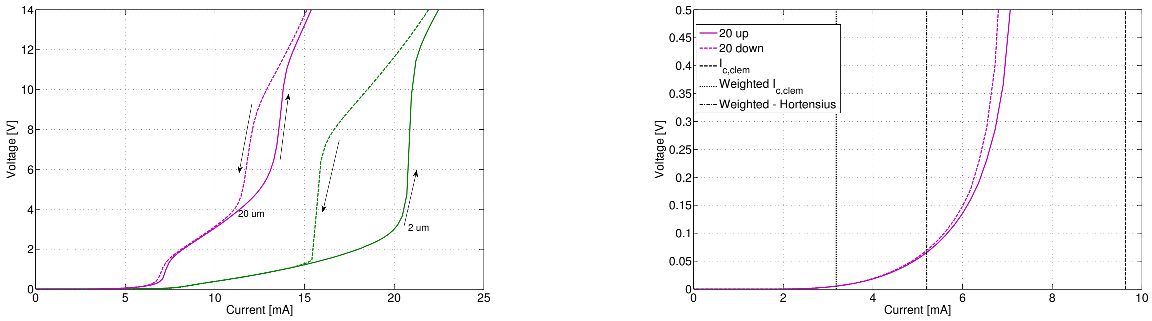

(c) Showing hysteresis of two different bridge lengths.

(d) Zoomed portion of the lower point of visible hysteresis.

Figure 3.13: 5 width microbridges [um] IV behaviour

The dR/dI behaviour from Fig. 3.13b could provide more ideal biasing current information than I_c. Biasing near a high resistance transition point could make detection events more probable. This analysis was followed for the 3 and 2 width microbridges as well, though as was discussed previously in Sec. 2.3.3, chances of successful device fabrication is proportional to dimensions of the device, and so there is less measurement data to analyze.

A comparison of the I_c of the microbridges of equal length can be seen in Fig. 3.14a. What is unexpected is the significantly smaller I_c of the narrower bridges compared to the 5 [um] width bridge, even more so when considering that decreasing width should if anything increase critical current density [30]. However they are also more susceptible to thermally induced voltages and self-generated hotspots, which could explain the drop. Another explanation, which could also explain the reason the measured I_c for all the devices is lower than theory suggests, is that the bridge edges were damaged during fabrication, leading to a far narrower superconducting channel than the design geometries suggest. Although the average critical current of 3 [um] width devices is higher than seen in Fig. 3.14a, likely due to a fabrication error that caused a narrow constriction along the line. Using Fig. 3.14a as a rough working point, there is no obvious ratio to suggest what this damaged amount might be, but Fig. 3.14b and given that most 1 [um] wide bridges are only resistive, suggests that up to 0.5 [um] from the edge of a device may be damaged.

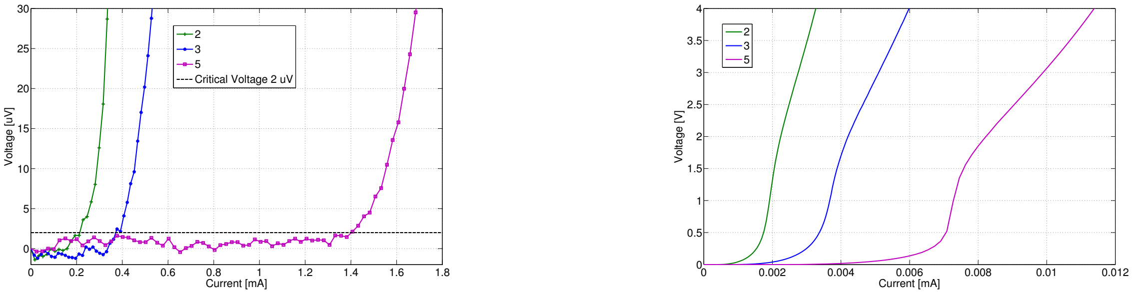

(a) Comparison of I_c of the microbridges. Correlation between I_c and bridge width clearly seen.

(b) High voltage measurement of 20 length microbridges [um].

Figure 3.14: X width by 20 length microbridges [um] IV behaviour

Measurements have actually shown that all of the 1 [um] wide devices (which were still intact) remain resistive at LN2 boiling temperature, an example of such seen in Fig. 3.15a. An alternative dipper probe setup using liquid helium was used to attempt to determine if the 1 [um] wide devices were damaged to the point of never transitioning to superconducting phase or if merely that the T_c was now below that of T_{LN2}. These measurements were taken with 2 point connections, as such a slight resistive slope is present even when the DUT is superconducting. In Fig. 3.15b, the IV curves of three identically designed 1 [um] wide circular meanders can be seen.

Sample 1 is clearly still resistive, where samples 2 and 3 show signs of superconducting. As the dipper probe at the time was not setup for accurate temperature measurements, it is unknown what the exact temperature was, though the sensor that was present was reading 20 [K], to which the devices should be within +/-5 [K]. With the measurement lead resistance being present in measurements it is difficult to determine the exact I$_c$ based on the 2 [uV] critical voltage used in the rest of this work. It is clear that at roughly 1 [nA] for sample 2 and 3 [nA] for sample 3, the devices transition to normal phase.

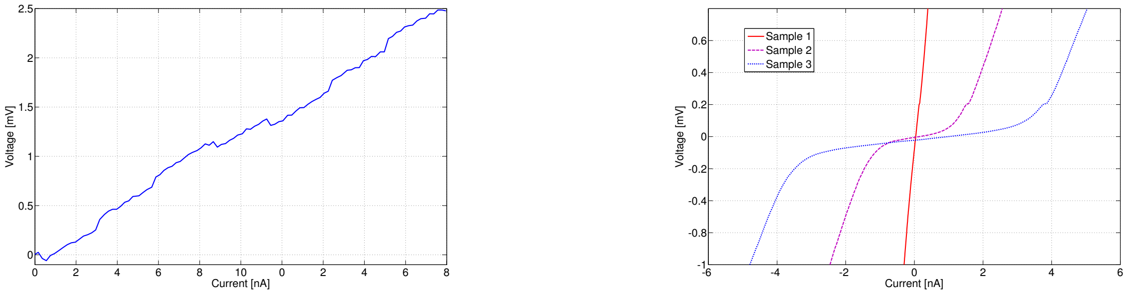

(a) 1 by 1 microbridge [um] at T$_{LN2}$ showing resistance behaviour

(b) Three samples of 1 [um] wide circular meanders. Sample 1 showing resistance, Sample 2 and 3 a superconducting phase.

Figure 3.15: IV plots of 1 [um] wide devices, showing both resistive behaviour at T$_{LN2}$ and superconducting at 20 [K]

Chapter 4

Microwave and Optoelectronic Measurements

The microwave cryostat, as discussed in Sec. 2.2, was used for both the Scattering parameter (S-parameter) and optoelectronic measurements of the CPW lines and devices. Though as was the case with the DC measurements, a review of relevant theory is first necessary to better analyze the results of these measurements.

4.1 Theory

The process for designing a superconducting thin film CPW line was discussed in depth in Sec. 2.3.2, though some of the theoretical reasoning behind the design process, such as the kinetic inductance, which was not explained, is discussed below. In addition how this applies for the purposes of photon detection is discussed.

4.1.1 Kinetic Inductance

The kinetic inductance is merely a representation of the inertia of the charge carriers. For normal conductors with extremely small collision times this effect is negligible, but with superconductors it begins to have a significant effect on microwave properties [11]. The total kinetic energy of the cooper pairs ($E_{k,tot}$) in a superconducting line can be found from

$$\mathrm{E}_{k,tot} = \left(\frac{1}{2}m^* v^2\right)(n_s l A) \tag{4.1}$$

where m^* is the mass of the cooper pair, two times that of an electron, n_s is the superconductor charge carrier density from (1.2) and l and A are the length and cross sectional area respectively. By equating this to an equivalent inductive energy E_L, the inductance due to the motion of the cooper pairs can be determined.

$$\mathrm{E}_\mathrm{L} = \frac{1}{2}\mathrm{LI}^2 \tag{4.2}$$

$$\mathrm{I} = q_e^* v n_s A \tag{4.3}$$

$$\mathrm{L}_k = \left(\frac{m^*}{n_s \left(q_e^*\right)^2}\right)\left(\frac{l}{A}\right) \tag{4.4}$$

where q_e^* is the charge of the cooper pairs, two times that of an electron. It is easy to see why the kinetic inductance increases as the temperature approaches T_c as the cooper pair density decreases. So any effect that causes a change in cooper pair density could be determined by measuring a change in the kinetic inductance. This change in kinetic inductance would in turn cause a change in the S-parameters of a device [54]. By illuminating a device by a laser of a known optical power and determining the change of the S-parameters compared to no illumination, the change of the kinetic inductance can be determined. This can give insight into the possible photon detection capability of the device. Another approach to measure such a change is the detection of a voltage pulse, as voltage from inductance is determined by

$$\mathrm{V} = \frac{\partial}{\partial t}(\mathrm{LI}) \tag{4.5}$$

Given a constant current, a change in the kinetic inductance would produce a voltage. Biasing near the critical current, as is the case with detectors following the hot spot model [55, 56, 57], is unnecessary as the current merely applies a scalar multiple to the voltage, though the bias current does reduce the energy gap [50]. This actually improves the response time as the detection is non-bolometric and so the fall time is not set by the cooling of a hotspot [58]. The minimum energy required for the breaking of a cooper pair to induce a voltage pulse can be determined from the temperature dependent energy gap from BCS theory.

$$2\Delta(T) = 3.52k_B \mathrm{T}_c\sqrt{1 - \left(\frac{\mathrm{T}}{\mathrm{T}_c}\right)^2} \tag{4.6}$$

This gives an energy gap of 11 [meV] for the devices in this work. Furthermore the change in behaviour of the kinetic inductance has been found to be closely related to the temperature relative to T_{BKT} [24, 59]. This implies that the presence of vortices has an effect on the behaviour of the kinetic inductance.

4.1.2 Vortex Microwave Behaviour

A number of experiments have resulted in a connection between vortices and microwave behaviour dependent on frequency, magnetic field and temperature. Work by Gasparov has shown a switch in the temperature dependence of the inductance of superconducting line at what is suggested to be a frequency dependent T_{BKT} [24]. Goettee found that in highfields, $\mathrm{B}_{c1}<\mathrm{B}<\mathrm{B}_{c2}$, the complex conductivity is dominated by the vortex dynamics in the YBCO thin film [60]. Einfeld shows that increased artificially generated defects in the thin film improved the surface resistance, as it provided pinning sites to reduce the number of free vortices [22], with a greater reduction of R_s at higher frequencies. Barboy also found steps in IV measurements similar to Shapiro steps that are due to the frequency of vortex nucleation inversely matching the flight time of the vortex across the channel [61]. This suggests a possibility of resonance due to vortices.

This behaviour of the vortices at microwave frequency relates to the interplay of the vortex viscosity and pinning strength depending on the frequency in question [62]. Song showed that at low frequencies the vortices will remain pinned in potential wells and can be viewed as harmonic with a spring constant of k_p. At higher frequencies, above the depinning frequency (f_d), the flux-flow vortex viscosity (η_e) becomes dominant leading to a more dissipative response. This can be accounted for from an effective complex resistivity due to vortices calculated from

$$\widetilde{\rho}_v = \frac{\Phi_0\left(\mathrm{B} - \mathrm{B}_{\mathrm{th}}\right)}{\eta_e}\frac{\epsilon + i\frac{f}{f_d}}{1 + i\frac{f}{f_d}} \tag{4.7}$$

$$\eta_e = \frac{\Phi_0 \mathrm{B}_{c2}}{\rho_n} \tag{4.8}$$

$$f_d = \frac{k_p}{2\pi\eta_e} \tag{4.9}$$

where $B_{\text{th}} = B_k/1.65$, and ϵ is a quantity between 0 and 1 representing the strength of the flux creep [62]. This can then be related to the change in the surface resistance and reactance compared between the values with and with out vortices present by

$$\frac{\Delta X_s}{\Delta R_s} - \frac{\operatorname{Im}(\widetilde{\rho}_v)}{\operatorname{Re}(\widetilde{\rho}_v)} = 0 \tag{4.10}$$

This provides a manner in which to analyze any variance in the expected microwave performance of a device as designed from the process in Sec. 2.3.2. Such variance could be averted by incorporating the modification to surface resistance calculations for high-T_c superconductors as presented by Marcon [59].

4.1.3 Vortex Assisted Photon Detection

Photon detection in superconductors has generally been accepted to follow the hotspot model [55, 39], though more recently suggestions towards kinetic inductance detectors as mentioned in Sec. 4.1.1 [58] or traveling wave detectors [63] have been proposed. In addition, vortex assisted detectors have been suggested as a modification to the hotspot model and as a means of explaining dark counts in detectors. Engel analyzed the dark count rates versus a biased current of a superconducting single photon detector (SSPD) with the theoretical thermal fluctuations in the number density of quasi-particles and thermal unbinding of VAPs as seen in Fig. 4.1 [50]. Bulaevskii took this a step further to suggest that detection events in a SSPD could be generated due to the photon exciting a vortex over the Gibbs free energy barrier, as discussed in Sec. 3.1 [43, 64].

Bulaevskii proposes that a detection event in a SSPD can be brought on by either a photon with enough energy to cause a normal belt transition across a narrow superconducting line, or a photon exciting a vortex over the Gibbs energy barrier (or breaking of a VAP). Provided a bias current that is greater than a threshold value (I^*) the vortex will excite quasi-particles, which is the work done by the Lorentz force, along the path it travels resulting in a normal belt across the width of the strip, referred to as a 'hot' vortex crossing. If the bias current is below the threshold value, it is a 'cold' crossing and does not excite enough quasi-particles to cause a belt transition. For the threshold value to be below that of the critical current, and allow the strip to be in this metastable state, the width of the strip must follow

$$w_c = 1.745 \times 10^6 \frac{\xi^2}{\widetilde{\Lambda}} \tag{4.11}$$

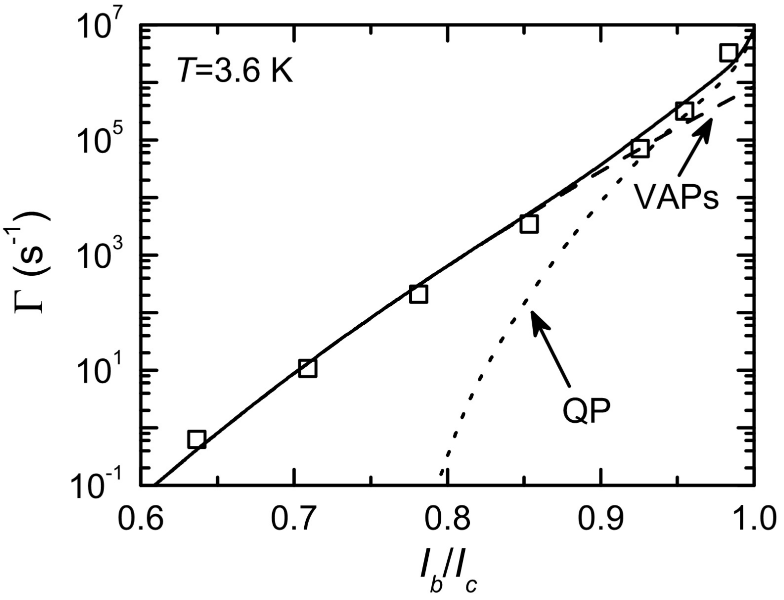

Figure 4.1: Dark count rate (squares) versus bias current with plots showing theoretical dark counts due to vortex-antivortex pairs and quasi-particle fluctuation [50]

where $\tilde{\Lambda}$ is the renormalized Pearl length to account for the bias current, though it causes a change no greater than roughly 15%. The application of a magnetic field in combination with a bias current will enhance the vortex crossing rate, with the magnetic field being equivalent to an increase in bias current but while not affecting hotspot creation rate [43].

The current dependent barrier height, and in turn the energy required to excite the vortex over it, can be determined from the work by Clem where

$$G_b = \frac{\phi_0^2}{2\pi\mu_0\Lambda}\ln\left(\frac{\mathrm{I}_c}{\mathrm{I}}\right) \tag{4.12}$$

For the devices in this work, this translates into a current dependent barrier height as shown in Fig. 4.2a. The energy required to locally suppress superconductivity as proposed by Xu is found from

$$\Delta F\left(\mathrm{T}\right) = \frac{1}{a}\frac{4\hbar}{6e}\mathrm{I}_c\left(\mathrm{T}\right) \tag{4.13}$$

where a is a fitting parameter. This gives a value of $(1/a)2739\times\mathrm{I}_c(\mathrm{T})$ [eV], which is shown in Fig. 4.2b with the I_c values for devices in this work highlighted. The value of the fitting parameter is unknown for the dimensions of the devices in this work, though literature has given values in the range of 0.76 and 0.95 for widths of 15 and 10 [nm] [38].

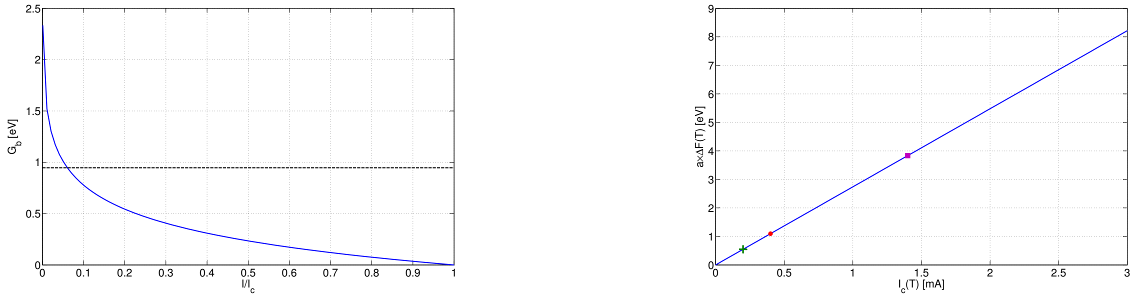

(a) Height of Gibbs barrier versus normalized bias current (solid blue). The dashed horizontal line shows the energy of a single 1310 [nm] photon.

(b) Energy to locally suppress superconductivity versus critical current. Fitting parameter has been removed from results as no values were available for device dimensions of this work. I_c of 2 [um] (+), 3 [um] (circle) and 5 [um] (square) width devices shown.

Figure 4.2: Energy Barriers of YBCO devices measured in this work

4.2 Measurements

The sample to be measured was placed on to the copper sample base after a thin layer of 'Leitsilber' Conductive Silver Cement was applied. It was then placed in the humidex safe until it had fully dried. The copper sample base was then screwed into place in the microwave cryostat, with the plexiglass top cap put firmly into place. The chamber was then pumped down to $10^{-}5$ [mbar] using the vacuum pump. Once down to near vacuum, liquid nitrogen was poured into the cryogen inlet port to cool down the cryostat. The cooldown (for both temperature sensors to reach steady state) would take roughly 50 minutes. Once the steady state temperature was reached, measurements would begin.

As the microwave cryostat in use for these measurements contained no blackbody shielding, the possible heat transfer caused by this, and as such the amount of energy any DUT might absorb during measurements, needs to be considered. Using the formula from Sec. 2.1.1, and assuming a best case unrealistic scenario (all radiation is completely normal to the surface and the side walls are not emitting any radiation), leads to 18.3 [mW] over the copper base sample holder. If only the area of device OF1 is considered, this drops to 3.246×10^{-8} [J/s], or 2.023×10^{11} [eV/s]. If we compare this to the relaxation time presented in [58] as a reasonable time window to analyze, this gives 2.023×10^{2} [eV/ns]. The peak wavelength of an item at room temperature (treating it as a blackbody) is 9.67 [um], which translates into a photon energy of 128 [meV]. If one considers the excitation values from Fig. 4.2, it is obvious that numerous vortices are being excited into the DUT and even possibly sections of the device switching to a normal state dependent on the fitting parameter from (4.13).

4.2.1 S-Parameter Measurements

The S-parameter measurements were made with the Agilent 8364B PNA, set to 6400 measurement points and an IF Bandwidth of 500 [Hz]. Before any reliable measurements could be taken, the system had to be calibrated, as in the setting of the reference plane to the tips of the picoprobes. An improper calibration would result in erroneous measurement results, giving S-parameter values that include effects from the measurement setup and not just the DUT. As the dimensions available in the cryostat made a Thru-Reflect-Line (TRL) calibration unfavorable, as it would result in poor accuracy at low frequencies, a Short-Open-Load-Thru (SOLT) calibration was chosen. Though SOLT also had an issue, as the Load component of the calibration is temperature sensitive. To compensate for this, a modified C-5 calibration wafer from GGB Industries was acquired, where the precision resistors were laser trimmed such that a DC resistance of 50 [Ω] was measured at T_{LN2}. Care was required of probe placement during calibration, as improper placement of the probe tips from the intended location could result in faulty calibration, such as geometric inductances being partially ignored. This care of probe placement was also required during regular operations, not only for proper measurements but to avoid any damaging of the picoprobes.

Initial measurements were taken on the CPW lines of varying dimensions, as seen in Table A.1, with the results seen in Fig. 4.3. Certainly as expected the variation from the dimensions as calculated in Sec. 2.3.2 result in a drop in performance quality, though a closer inspection of the actually matched dimensions (80 um) shows a drop of half a dB by 13 GHz and a full dB by 32 GHz. This warranted comparison to simulated results. As such it was compared to (i) a perfect conductor, (ii) a perfect conductor with calculated kinetic inductance, and (iii) surface resistance and reactance as calculated from [65]. The third comparison is at a smaller sample rate as the simulation software used, Agilent Design System and Sonnet, does not have the proper quadratic scaling of surface resistance for a superconductor, so minute frequencies were simulated with the frequency dependent resistance entered manually. This approach was also used to attempt to fit a simulation to measurement results in order to determine the actual surface resistance of the DUT. The results can be seen in Fig. 4.4.

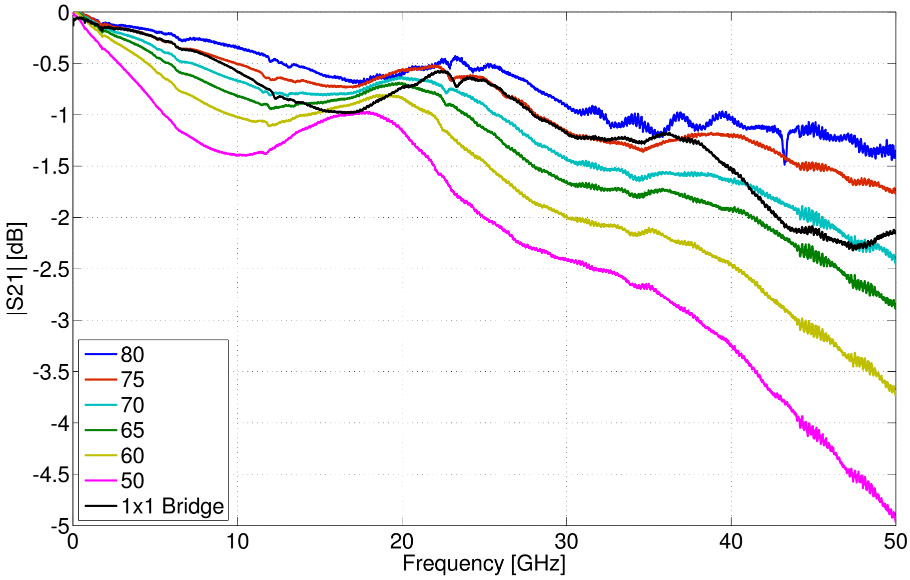

Figure 4.3: |S21| measurement results of 4 mm long CPWs of varying central line widths (s) [um]. |S21| of a 1x1 um bridge embedded in a 80 um central line also shown.

The parameters used for attempting to fit a plot to the measured data was a surface resistance with both linear and quadratic component, $aw + bw^2$ where $a \approx 10^{-10}$ and $b \approx 1.1 \times 10^{-22}$. The linear component is likely partially due to the gold contact pads. The kinetic inductance that was calculated and used in Fig. 4.3, 6.16 pH, was modified slightly in the fitting plot to 7 pH. As this translates into a much higher surface resistance than any of the vortex free models suggest, the measurements seem to strongly indicate vortex motion causing an increase in surface resistance. Although the depinning frequency for these CPWs is unknown, and as the spring force constant of the pinning sites is unknown it can not be calculated. Marcon suggests, based on their measurements, it is approximately 20 GHz. If the relative error of (4.10) is taken for different frequencies (using the calculation as the true value), the result is as seen in Table 4.1. The linear component of the surface resistance, believed to be due to the contact pads, was removed for these calculations. At low frequencies it can be seen there is significant relative error, but at higher frequencies, which are likely higher than the depinning frequency, this drops to merely a few percent.

Table 4.1: Relative error of microwave measurement results compared to theoretical vortex explanation.

Frequency [GHz]	5	10	15	20	25	30	35	40	45
Relative Error - (4.10)	0.730	0.401	0.173	0.047	0.014	0.040	0.044	0.038	0.026

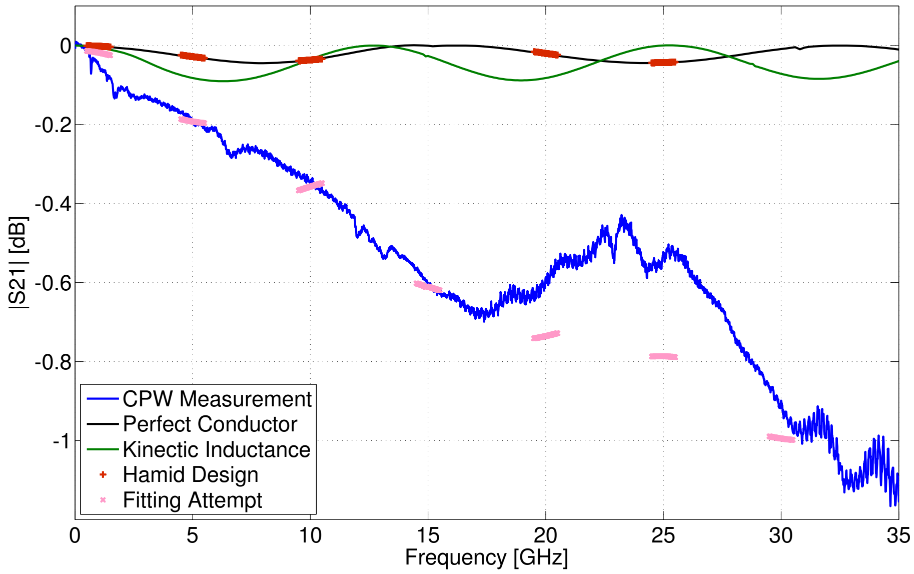

Figure 4.4: |S21| comparison of different modeling of a 80 um central line CPW and the actual measurement.

Although there were a large number of devices tested, as seen in Table A.1, the majority showed no overly interesting microwave behaviour besides that previously discussed. The measurement results are excluded from this work but are available upon request (as there is over 250 figures). The microbridges caused a minor loss in transmission proportional to the bridge length and inversely proportional to the width, with the greatest loss being the 2x50 bridge causing an additional 9 [dB] loss at 35 [GHz]. The meander lines behaviour was similar, but as transmission at low frequencies was still fairly high, |S21| results were similar to that of a low pass filter. Some devices that were showing some interesting responses were the circular and square based meander designs, an example of which is seen in Fig. 4.5. The DC analysis results of this device design can be seen in Fig. A.5 and Fig. A.6.

Although this transmission quality is poor for any practical device application, the sharp change at 27.5 [GHz] provides a convenient response in which to measure any changes due to optical excitation. Further analysis of the CPWs were undertaken, such as plots of the frequency dependent impedance, and are available in the appendix, Figures A.9, A.10, A.11.

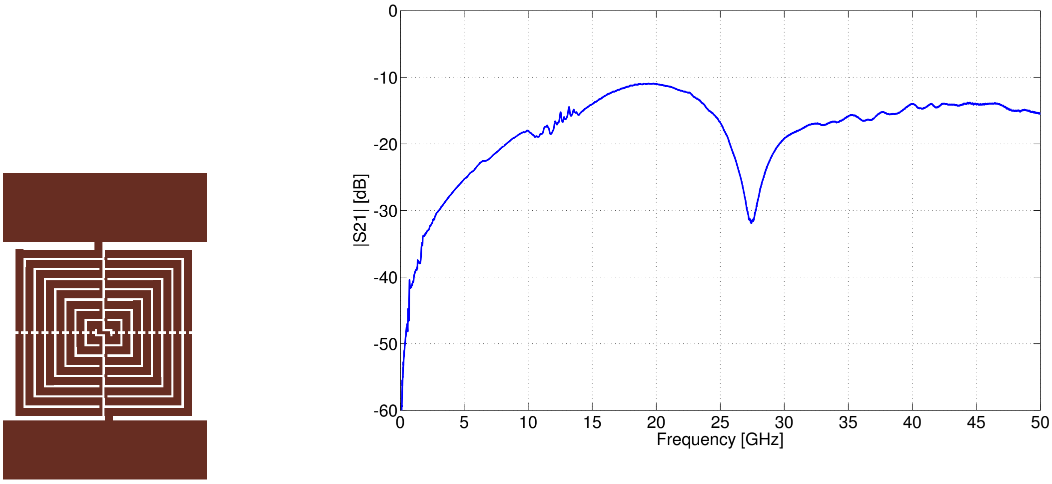

(a) OF1 - ADS Design image.

(b) |S21| of device OF1 from Fig. 4.5a

Figure 4.5: Device OF1 - Square meander device design, 3 um width with multiple 1x1 um embedded bridges. Surface area is 70x65 um with a filling factor of 78%

4.2.2 Optoelectronic Measurements

Initial optoelectronic measurements were made on a number of meander lines using the same setup as for S-parameter measurements, but with the inclusion of the optic fiber probe. A low power red laser was used to align and focus the optic fiber, and a 1310 [nm] wavelength diode laser from NEL Japan was used for the optoelectronic measurements. As measurements were initially just to detect any noticeable change of the S-parameter of a device, the laser diode forward current was set to 100 [mA], which translates into an output power of 16.7 [mW] as it is assumed it was operating in a linear regime. This translates into 1.042 $\times 10^{17}$ [eV/s], or 1.1 $\times 10^{17}$ [photons/s]. It is unknown what the level of attenuation caused by the fiber component in the cryostat, due to both the coupling and bending, was and therefore a weighting factor variable must be applied to all end results.

Analysis is focused on the device that showed the most significant response, OF1, which can be seen in Fig. 4.6. This noticeable shift in resonance that occurs at 27.5 [GHz] of 300 [MHz] suggests a change in the kinetic inductance, but there are likely other aspects in play. Comparing the change of the responses between the measurement and the simulation in Fig. 4.7, a change of kinetic inductance of 0.3 [pH] gives an equivalent shift in the resonance. It does seem odd that the measurement shows no change in attenuation, as not only should the drop in superconductor charge carrier density, which causes the change in kinetic inductance, result in an increase in the normal charge carrier density, but vortices should likely be being excited into the device resulting in loss of power due to the work of the Lorentz force. It is possible that as the 1 [um] bridges in the device are not superconducting, they are causing an unexpected impact on the rest of the devices behaviour. Measurements at a lower temperature would be necessary to clarify the reason for this behaviour.

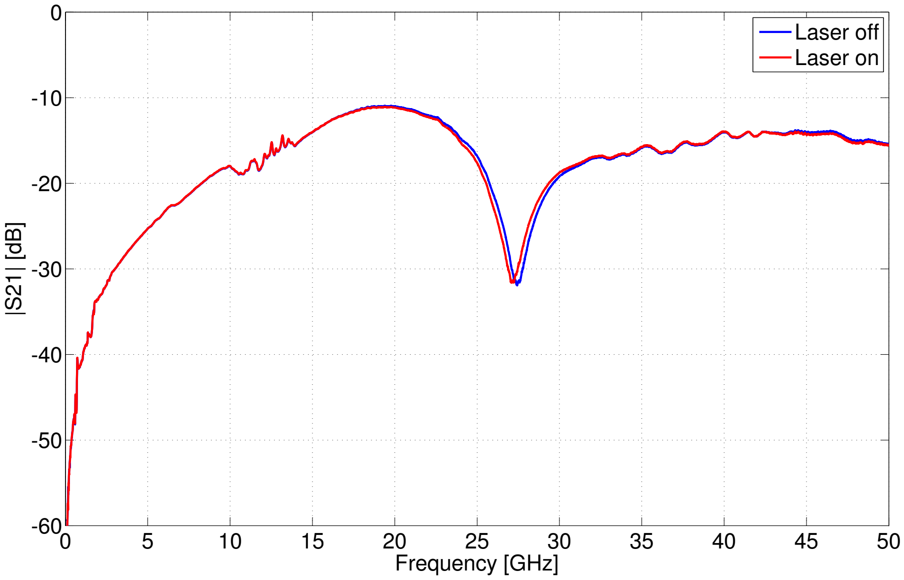

Figure 4.6: |S21| plot of OF1 device response to a 1310 [nm] laser at 16.7 [mW] output power.

Taking the incoming power of the laser with respect to the device area, with the laser spot size of 300 [um], gives 6.707 × 10^{15} [eV/s] or 6.707 × 10^{6} [eV/ns]. This gives 7.082 × 10^{6} photon collision per nanosecond over the device area. Assuming that the photons falling outside the area of the meander line are not affecting the microwave performance, which although is likely not the case it serves for this approximation, then it is this number which is responsible for such a change in the kinetic inductance. The opacity of the YBCO thin film should also be taken into consideration, due to it being so thin it is nearly transparent. Taking the refractive index of YBCO from [66] of n = 1.6 - j0.48, and that the laser beam is normal to the device surface, 5.3% is reflected. Applying Beer-Lambert law with the imaginary component of the refractive index then gives an absorbtion of only 10.9%, which drops to 10.3% when considering reflection loss. This translates into only 6.91 × 10^{5} [eV/ns] being absorbed, or 7.3 × 10^{5} [photons/ns].

Following the relation of kinetic inductance to the number of cooper pairs, a simplified approximation can be reached as seen in (4.14). This is merely a ballpark calculation, for the purposes of determining if the device could possibly be in the realm of detecting a single photon. As the

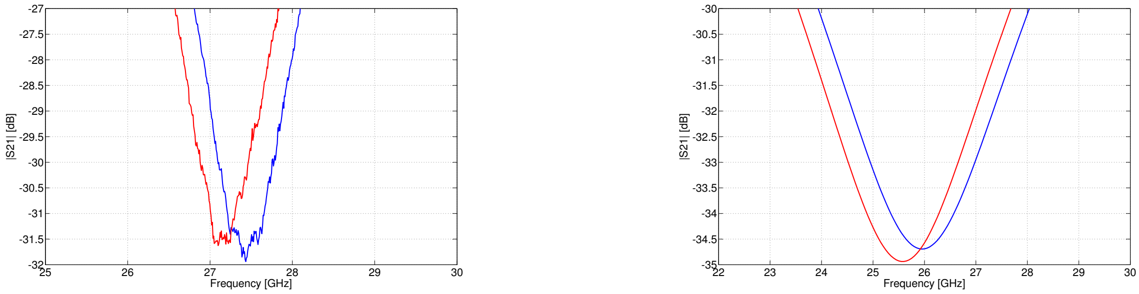

(a) Measurement

(b) Simulation

Figure 4.7: Device OF1 - focus on resonance shift from 1310 nm laser illumination and equivalent change in a simulation with comparable change of kinetic inductance (0.3 [pH]). Blue plot - laser off, red plot - laser on.

rise time measured from [58] for a photon incident is 29 [ps], it is reasonable to consider this as the time frame for determining the voltage generated by a change in kinetic inductance with (4.5). From the same work the fall time is used to estimate a time window for a photon count that sets a constant change in kinetic inductance.

$$\frac{\Delta \mathrm{L}_{k2}}{\Delta \mathrm{L}_{k1}} \sim \frac{\Delta n_{s2}}{\Delta n_{s1}} \tag{4.14}$$

From this it is estimated that a single photon would cause such a small change in the kinetic inductance that no measurable voltage pulse would occur. This collaborates with the measurements from [58] in which a thicker filmed (100 nm) YBCO meander line with 1.067×10^8 photons at 1550 nm wavelength absorbed over a 45 [ps] pulse generated voltage pulses on the order of 10^{-2} V. However, the OF1 device should generate a measurable pulse (on the order of 10^{-8} [V]) with a photon count on the order of a thousand to ten thousand. It should again be kept in mind that this is a rough estimate based on the currently available data, and far more accurate measurements are required to determine device viability. This however can not be accurately measured in the currently available microwave cryostat due to the large sources of thermal noise that is present as discussed previously.

These calculations also ignored the possibility of vortex assisted detection, which is more likely than simply being due to change in kinetic inductance as seen from Fig. 4.2a. For this to apply, the device line width must be less than the critical width, which is found to be 17 [um] for 25 [nm] thin film YBCO at T_{LN2}. With the largest line component of device OF1 being only 3 [um], it is far below this critical width, and so vortex assisted detection is far more probable. For an apt analysis of this scenario, pulse detection measurements are required in the presence of a variable magnetic field, following the method from [64]. Pulse measurements with a scanning squid microscope could also give useful insight on the vortex influence on detection events.

Chapter 5

Conclusion and Future Work

5.1 Conclusion

A series of YBCO thin film (25 [nm]) devices were designed for the purpose of DC, microwave and optoelectronic characterizations. To accommodate the DC characterization of these devices, a functioning dipper probe cryostat has been successfully designed, constructed and implemented. PCB test beds were also successfully designed and constructed to accommodate the samples used in said dipper probe. Thermal calculations showed the DUTs suffering negligible increases in temperature and being strongly coupled to the cryogen bath. For the microwave and optoelectronic measurements, CPW transmission lines were designed following an accepted superconductor microwave methodology which was discussed.

Both resistance-temperature and current-voltage measurements were made on the DC devices. The T_c of a selection of devices was determined and fell into agreement with theory. 1 [um] width devices showed T_c of below T_{LN2}, which was explained through the introduction of vortex physics. This explanation was also applied to the I_c values measured, which fell below that extrapolated from bulk values, agreeing more so with that calculated from vortex theory.

S-parameter measurements were successfully completed on all of the microwave devices. Measurements of the CPWs of varying dimensions were compared to determine viability of design methodology. Comparison to simulations showed higher than expected attenuation, with simulations fitting measurement results having much higher surface resistances than the design process suggested. Explanations for this variance using vortex physics were discussed.

Optoelectronic measurements showed a change in S-parameter measurements from optical excitation translating to a change in the kinetic inductance. Calculations based on the kinetic inductance change showed the photon detection feasibility of the meander devices, falling into the realm of 1000 to 10000 photons for a measurable detection event. Improvement of detection capability through vortex assisted detection was discussed, including explanation on the necessary testing environment for such an implementation.

5.2 Future Work

To improve the understanding behind the vortex physics occurring in these devices, measurements under a variable magnetic field are necessary. This applies for IV measurements, microwave and attempts at photon detection. This also would require the use of a cryostat that can support temperatures below T_{LN2}, as higher magnetic fields would lower the T_c of devices, in addition to the 1 [um] width devices already having a T_c below T_{LN2}. Measurements of Shapiro steps would provide more evidence and insight on the vortex behaviour. The use of a scanning squid microscope would also provide hard evidence on the presence and behaviour of vortices, and possibly on how the geometries alter their nucleation rates and locations; as in if it is primarily vortices excited from edges or thermally excited VAPs forming in the lines. Photon detection measurements using a properly shielded cryostat to confirm the analysis and calculation in this work would give direction to design modifications necessary to approach single photon detection.

Thinner bridges could be generated using even the current YBCO thin film used in this work following the AFM etching process discussed in [67, 32]. This would allow further analysis on the geometrical effect on the DC behaviour of the devices, and if narrowing of the device dimensions would increase photon detection capability. However, it is suggested any design focusing on photon detection also focus on the improvement of coupling, because such a thin film of YBCO has very poor coupling to an optical source. In addition, new designs following the methodology of both Clem for the meander line [41] and Marcon or Song for the CPW [62, 59] should be implemented, as both account for vortices degrading device performance.

Bibliography

[1] H. K. Onnes, “Further experiments with liquid helium. d. on the change of electric resistance of pure metals at very low temperatures, etc. v. the disappearance of the resistance of mercury.,” *Leiden Commun.*, 1911.

[2] K. Fossheim and A. Sudbo, *Superconductivity Physics and Applications.* John Wiley and Sons, 1st ed., 2004.

[3] W. Meissner and R. Ochsenfeld, “Ein neuer effekt bei eintritt der supraleitfähigkeit,” *Naturwissenschaften*, vol. 21, no. 44, pp. 787 – 788, 1933.

[4] F. London and H. London, “The electromagnetic equations of the supraconductor,” *Proc. R. Soc. Lond. A*, vol. 149, pp. 71 – 88, 1935.

[5] V. Ginzburg and L. Landau, “To the theory of superconductivity,” *Zh. Eksp. Teor. Fiz.*, vol. 20, p. 1064, 1950.

[6] A. A. Abrikosov, “On the magnetic properties of superconductors of the second group,” *Soviet Physics JETP 5*, vol. 5, no. 6, p. 1174, 1957.

[7] J. Bardeen, L. N. Cooper, and J. R. Schrieffer, “Theory of superconductivity,” *Phys. Rev.*, vol. 108, pp. 1175–1204, Dec 1957.

[8] W. A. Little, “Possibility of synthesizing an organic superconductor,” *Phys. Rev.*, vol. 134, pp. A1416–A1424, Jun 1964.

[9] J. G. Bednorz and K. A. Muller, “Perovskite-type oxides - the new approach to high-tc superconductivity,” *Reviews of Modern Physics*, vol. 60, pp. 585–600, July 1988.

[10] M. K. Wu, J. R. Ashburn, C. J. Torng, P. H. Hor, R. L. Meng, L. Gao, Z. J. Huang, Y. Q. Wang, and C. W. Chu, “Superconductivity at 93 k in a new mixed-phase y-ba-cu-o compound system at ambient pressure,” *Phys. Rev. Lett.*, vol. 58, pp. 908–910, Mar 1987.

[11] T. V. Duzer and C. W. Turner, *Superconductive Devices and Circuits.* Prentice Hall, 2nd ed., 1999.

[12] I. Hetel, T. R. Lemberger, and M. Randeria, "Quantum critical behaviour in the superfluid density of strongly underdoped ultrathin copper oxide films," *Nature Physics*, vol. 3, pp. 700–702, Oct 2007.

[13] V. M. Vinkour, T. I. Baturina, M. V. Fistul, A. Y. Mironov, M. R. Baklanov, and C. Strunk, "Superinsulator and quantum synchronization," *Nature*, vol. 452, pp. 613–615, April 2008.

[14] D. S. Fisher, M. P. A. Fisher, and D. A. Huse, "Thermal fluctuations, quenched disorder, phase transitions, and transport in type-ii superconductors," *Phys. Rev. B*, vol. 43, pp. 130–159, Jan 1991.

[15] O. Vendik, I. Vendik, and D. Kaparkov, "Empirical model of the microwave properties of high-temperature superconductors," *Microwave Theory and Techniques, IEEE Transactions on*, vol. 46, pp. 469–478, May 1998.

[16] K. H. Kuit, J. R. Kirtley, W. van der Veur, C. G. Molenaar, F. J. G. Roesthuis, A. G. P. Troeman, J. R. Clem, H. Hilgenkamp, H. Rogalla, and J. Flokstra, "Vortex trapping and expulsion in thin-film ybco strips," *Phys. Rev. B*, vol. 77, p. 134504, Apr 2008.

[17] A. Pound, J. Carbotte, and E. Nicol, "Optical properties of the pseudogap state in underdoped cuprates," *The European Physical Journal B - Condensed Matter and Complex Systems*, vol. 81, pp. 69–77, May 2011.

[18] J. W. Ekin, *Experimental Techniques for Low-Temperature Measurements: Cryostat Design, Material Properties and Superconducting Critical Current Testing.* Oxford University Press, 1st ed., 2006.

[19] H. L. Hortensius, E. F. C. Driessen, T. M. Klapwijk, K. K. Berggren, and J. R. Clem, "Critical-current reduction in thin superconducting wires due to current crowding," *Applied Physics Letters*, vol. 100, no. 18, p. 182602, 2012.

[20] M. Hein, *High-Temperature-Superconductor Thin Films at Microwave Frequencies.* Springer, 1st ed., 1999.

[21] H. Mohebbi and A. Majedi, "Analysis of series-connected discrete josephson transmission line," *Microwave Theory and Techniques, IEEE Transactions on*, vol. 57, pp. 1865–1873, Aug. 2009.

[22] J. Einfeld, P. Lahl, R. Kutzner, R. Wardenweber, and G. Kastner, "Reduction of the microwave surface resistance in ybco thin films by microscopic defects," *Physica C: Superconductivity*, vol. 351, no. 2, pp. 103 – 117, 2001.

[23] J. Wosik, L.-M. Xie, and R. Grabovickic, "Thermal effects in microwave current-induced weak link switching in ybco thin films," *Superconductor Science and Technology*, vol. 22, no. 10, p. 105003, 2009.

[24] V. Gasparov, G. Tsydynzhapov, I. Batov, and Q. Li, "Temperature and frequency dependence of complex conductance of ultrathin ybco films: Observation of vortex–antivortex pair unbinding," *Journal of Low Temperature Physics*, vol. 139, pp. 49–63, 2005. 10.1007/s10909-005-3911-6.

[25] Y. Matsuda, S. Komiyama, T. Onogi, T. Terashima, K. Shimura, and Y. Bando, "Thickness dependence of the kosterlitz-thouless transition in ultrathin ybco films," *Phys. Rev. B*, vol. 48, pp. 10498–10503, Oct 1993.

[26] S. A. Cybart, S. M. Anton, S. M. Wu, J. Clarke, and R. C. Dynes, "Very large scale integration of nanopatterned ybco josephson junctions in a two-dimensional array," *Nano Letters*, vol. 9, no. 10, pp. 3581–3585, 2009.

[27] D. Prokof'ev, M. Volkov, and Y. Boikov, "Pseudogap and its temperature dependence in ybco from the data of resistance measurements," *Physics of the Solid State*, vol. 45, pp. 1223–1232, 2003. 10.1134/1.1594234.

[28] K. Kuit, J. Kirtley, J. Clem, H. Rogalla, and J. Flokstra, "Vortex trapping and expulsion in thin-film type-ii superconducting strips," *Applied Superconductivity, IEEE Transactions on*, vol. 19, pp. 3537–3540, june 2009.

[29] J. Bonetti, D. Caplan, D. Van Harlingen, and M. Weissman, "Electronic transport in underdoped ybco nanowires: Evidence for fluctuating domain structures," *Physical Review Letters*, vol. 93, no. 8, pp. 20–23, 2004.

[30] H. Jiang, Y. Huang, H. How, S. Zhang, C. Vittoria, A. Widom, D. B. Chrisey, J. S. Horwitz, and R. Lee, "Observation of ultrahigh critical current densities in high–tc superconducting bridge constrictions," *Phys. Rev. Lett.*, vol. 66, pp. 1785–1788, Apr 1991.

[31] N. Curtz, E. Koller, H. Zbinden, M. Decroux, L. Antognazza, O. Fischer, and N. Gisin, "Patterning of ultrathin ybco nanowires using a new focused-ion-beam process," *Superconductor Science and Technology*, vol. 23, no. 4, 2010.

[32] A. Elkaseh, V. Srinivasu, and W. Perold, “Observation of shapiro-steps in afm-plough micron-size ybco planar constrictions,” *Applied Superconductivity, IEEE Transactions on*, vol. 19, pp. 187–190, June 2009.

[33] K. Develos-Bagarinao, H. Yamasaki, J. C. Nie, and Y. Nakagawa, “Thickness dependence of j_c for ybco thin films prepared by large-area pulsed laser deposition on ceo2-buffered sapphire substrates,” *Superconductor Science and Technology*, vol. 18, no. 5, p. 667, 2005.

[34] O. Shcherbakova, A. Pan, S. Gorman, S. Fedoseev, I. Golovchanskiy, and S. Dou, “Inhomogeneities in ybco thin films with reduced thickness,” *Physica C: Superconductivity*, 2012.

[35] R. Liang, D. Bonn, and W. Hardy, “Growth of high quality ybco single crystals using bazro3 crucibles,” *Physica C: Superconductivity*, vol. 304, no. 1-2, pp. 105 – 111, 1998.

[36] I. Golovchanskiy, A. Pan, S. Fedoseev, O. Shcherbakova, and S. Dou, “Critical current behaviour of ybco thin films described by vortex pinning on low-angle domain boundaries and vortex creep,” *Physica C: Superconductivity*, 2012.

[37] S. Nawaz, T. Bauch, and F. Lombardi, “Transport properties of ybco nanowires,” *Applied Superconductivity, IEEE Transactions on*, vol. 21, pp. 164 –167, June 2011.

[38] K. Xu and J. R. Heath, “Long, highly-ordered high-temperature superconductor nanowire arrays,” *Nano Letters*, vol. 8, no. 11, pp. 3845–3849, 2008.

[39] R. Gerbaldo, F. Laviano, G. Ghigo, L. Gozzelino, B. Minetti, A. Rovelli, and E. Mezzetti, “Nanostructuring ybco thin films by heavy-ion beam for local magnetic field and infrared photon detection,” *Nuclear Instruments and Methods in Physics Research Section B: Beam Interactions with Materials and Atoms*, vol. 272, no. 0, pp. 291–295, 2012. Proceedings of the 17th International Conference on Ion Beam Modification of Materials (IBMM 2010).

[40] W. Kwok, R. Olsson, G. Karapetrov, U. Welp, V. Vlasko-Vlasov, K. Kadowaki, and G. Crabtree, “Modification of vortex behavior through heavy ion lithography,” *Physica C: Superconductivity*, vol. 382, no. 1, pp. 137–141, 2002.

[41] J. R. Clem and K. K. Berggren, “Geometry-dependent critical currents in superconducting nanocircuits,” *Phys. Rev. B*, vol. 84, p. 174510, Nov 2011.

[42] H. Bartolf, A. Engel, A. Schilling, K. Il’in, M. Siegel, H. H, and A. Semenov, “Current-assisted thermally activated flux liberation in ultrathin nanopatterned nbn superconducting meander structures,” *Phys. Rev. B*, vol. 81, p. 024502, Jan 2010.

[43] L. N. Bulaevskii, M. J. Graf, and V. G. Kogan, “Vortex-assisted photon counts and their magnetic field dependence in single-photon superconducting detectors,” *Phys. Rev. B*, vol. 85, p. 014505, Jan 2012.

[44] L. Steponaviciene, J. Sulcas, A. Jukna, and I. Barboy, “Current-voltage dependences of ybco superconducting thin films with laser-written channel of easy vortex motion,” *Materials Science (Medziagotyra)*, vol. 15, no. 4, pp. 291–295, 2009.

[45] F. Tafuri, J. Kirtley, D. Born, D. Stornaiuolo, P. Medaglia, P. Orgiani, G. Balestrino, and V. Kogan, “Dissipation in ultra-thin current-carrying superconducting bridges; evidence for quantum tunneling of pearl vortices,” *EPL (Europhysics Letters)*, vol. 73, no. 6, p. 948, 2006.

[46] S. L. Chu, A. Bollinger, and A. Bezryadin, “Phase slips and vortex-antivortex pairs in superconducting films with constrictions,” *Physical Review B*, vol. 70, p. 6, 2003.

[47] V. Kogan, “Interaction of vortices in thin superconducting films and the berezinskii-kosterlitz-thouless transition,” *Physical Review B*, vol. 75, 2007.

[48] J. R. Clem, “Pancake vortices,” *Journal of Superconductivity*, vol. 17, pp. 613–629, Nov. 2004.

[49] N. Kuzmichev, M. Vasyutin, and A. Golovashkin, “Ybco single cystals i-v characteristics nonlinearity and nelson-kosterlitz jump,” *Physica C*, vol. 460-462, pp. 849 – 850, 2007.

[50] A. Engel, A. Semenov, H.-W. Huebers, K. Ilin, and M. Siegel, “Fluctuation effects in superconducting nanostrips,” *Physica C: Superconductivity*, vol. 444, no. 12, pp. 12 – 18, 2006.

[51] G. D. Poulin, J. Lachapelle, S. H. Moffat, F. A. Hegmann, and J. S. Preston, “Current–voltage characteristics of dc voltage biased high temperature superconducting microbridges,” *Applied Physics Letters*, vol. 66, no. 19, pp. 2576–2578, 1995.

[52] O. Haugen, T. Johansen, H. Chen, V. Yurchenko, P. Vase, D. Winkler, B. Davidson, G. Testa, E. Sarnelli, and E. Altshuler, “High resolution thermal imaging of hotspots in superconducting films,” *Applied Superconductivity, IEEE Transactions on*, vol. 17, pp. 3215–3218, june 2007.

[53] S. Tochihara, H. Yasuoka, H. Mazaki, M. Osada, and M. Kakihana, “Lower critical fields of bscco and ybco single crystals,” *Journal of Applied Physics*, vol. 85, no. 12, pp. 8299–8306, 1999.

[54] H. Atikian, B. Ghamsari, and A. Majedi, “Experimental characterization of optically tunable high-temperature superconducting microwave resonators and delay lines,” *Microwave Theory and Techniques, IEEE Transactions on*, vol. 58, pp. 3320–3326, Nov. 2010.

[55] R. Sobolewski, J. Zhang, W. Slysz, A. Pearlman, A. Verevkin, A. Lipatov, O. Okunev, G. Chulkova, A. Korneev, K. Smirnov, P. Kouminov, B. Voronov, N. Kaurova, V. Drakinsky, and G. N. Goltsman, "Ultrafast superconducting single-photon optical detectors," *Advanced Optical Devices, Technologies, and Medical Applications*, vol. 5123, no. 1, pp. 1–11, 2003.

[56] C. M. Natarajan, M. G. Tanner, and R. H. Hadfield, "Superconducting nanowire single-photon detectors: physics and applications," *Superconductor Science and Technology*, vol. 25, no. 6, p. 063001, 2012.

[57] A. M. Kadin and M. W. Johnson, "Nonequilibrium photon-induced hotspot: A new mechanism for photodetection in ultrathin metallic films," *Applied Physics Letters*, vol. 69, no. 25, pp. 3938–3940, 1996.

[58] H. A. Atikian, B. G. Ghamsari, S. M. Anglage, and A. H. Majedi, "Ultrafast linear kinetic inductive photoresponse of ybco meander-line structures by photoimpedance measurements," *Applied Physics Letters*, vol. 98, 2011.

[59] R. Marcon, R. Fastampa, M. Giura, and E. Silva, "Vortex-motion dissipation in high-t_c superconductors at microwave frequencies," *Phys. Rev. B*, vol. 43, pp. 2940–2945, Feb 1991.

[60] J. Goettee, Y. Kudasov, W. Zerwekh, A. Bykov, M. Dolotenko, C. Fowler, B. Feeman, J. King, N. Kolokolchikov, W. Lewis, B. Marshall, B. Papatheofanis, V. Platonov, P. Rodriguez, M. Sheppard, O. Tatsenko, and L. Veeser, "Complex microwave conductivity of ybco in magnetic fields up to 500t," *Physica C: Superconductivity*, vol. 235-240, Part 3, pp. 2090–2091, 1994.

[61] I. Barboy, A. Jukna, G. Bareli, and G. Jung, "Quasi-josephson effects generated by coherent vortex flow in easy motion laser processed channels," *Physica C: Superconductivity*, vol. 470, Supplement 1, no. 0, pp. S799 – S800, 2010.

[62] C. Song, T. W. Heitmann, M. P. DeFeo, K. Yu, R. McDermott, M. Neeley, J. M. Martinis, and B. L. T. Plourde, "Microwave response of vortices in superconducting thin films of re and al," *Phys. Rev. B*, vol. 79, p. 174512, May 2009.

[63] B. G. Ghamsari and A. H. Majedi, "Superconductive traveling-wave photodectors: Fundamentals and optical propagation," *IEEE Journal of Quantum Electronics*, vol. 44, pp. 667–675, July 2008.

[64] L. N. Bulaevskii, M. J. Graf, C. D. Batista, and V. G. Kogan, "Vortex-induced dissipation in narrow current-biased thin-film superconducting strips," *Phys. Rev. B*, vol. 83, p. 144526, Apr 2011.

[65] H. R. Mohebbi and A. H. Majedi, “Cad model for circuit parameters of superconducting-based hybrid planar transmission lines,” *Superconductor Science and Technology*, vol. 22, no. 12, p. 125028, 2009.

[66] B. G. Ghamsari and A. H. Majedi, “Surface plasmon-enhanced coupling of optical guided waves to high-temperature superconducting optoelectronic structures,” *IEEE Transactions on Applied Superconductivity*, vol. 21, pp. 3646–3651, December 2011.

[67] A. Elkaseh, W. J. Perold, and V. V. Srinivasu, “Josephson nanoconstrictions made by afm plowing of ybco films,” *Journal of Applied Physics*, vol. 108, no. 5, 2010.

Appendix A

Appendix

Table A.1: Listing of all microwave devices. DC devices make up a subset of this list (no tapered designs for the DC devices). ML = Meander Line WLB = Weak Link Bridge

ID#	Width	Device	Additional Notes
A1	80 um	CPW	
A2	80 um	CPW	
A3	90 um	CPW	
A4	90 um	CPW	
A5	75 um	CPW	
A6	75 um	CPW	
A7	70 um	CPW	
A8	70 um	CPW	
A9	65 um	CPW	
B1	65 um	CPW	
B2	60 um	CPW	
B3	60 um	CPW	
B4	50 um	CPW	
B5	50 um	CPW	
B6	80 um	1x1 um WLB	Width x Length
B7	80 um	1x1 um WLB	Tapered center and ground
B8	80 um	1x1 um WLB	Tapered center
B9	80 um	0.75x1 um WLB	
C1	80 um	0.75x1 um WLB	Tapered center and ground
C2	80 um	0.75x1 um WLB	Tapered center
C3	80 um	1x2 um WLB	
C4	80 um	1x2 um WLB	Tapered center and ground
C5	80 um	1x2 um WLB	Tapered center
C6	80 um	1x5 um WLB	
C7	80 um	1x5 um WLB	Tapered center and ground
C8	80 um	1x5 um WLB	Tapered center
C9	80 um	1x10 um WLB	
D1	80 um	1x10 um WLB	Tapered center and ground
D2	80 um	1x10 um WLB	Tapered center
D3	80 um	1x20 um WLB	
D4	80 um	1x20 um WLB	Tapered center and ground
D5	80 um	1x20 um WLB	Tapered center
D6	80 um	1x50 um WLB	
D7	80 um	1x50 um WLB	Tapered center and ground
D8	80 um	1x50 um WLB	Tapered center
D9	80 um	1x50 um WLB	Bent bridge, for minimal spacing of center line
E1	80 um	1x50 um WLB	Bent bridge, for minimal spacing of center line

Continued on next page

Table A.1 – continued from previous page

ID#	Width	Devices	Additional Notes
E2	80 um	1x50 um WLB	Bent bridge, for minimal spacing of center line
E3	80 um	2x1 um WLB	
E4	80 um	2x1 um WLB	Tapered center and ground
E5	80 um	2x1 um WLB	Tapered center
E6	80 um	2x2 um WLB	
E7	80 um	2x2 um WLB	Tapered center and ground
E8	80 um	2x2 um WLB	Tapered center
E9	80 um	2x5 um WLB	
F1	80 um	2x5 um WLB	Tapered center and ground
F2	80 um	2x5 um WLB	Tapered center
F3	80 um	2x10 um WLB	
F4	80 um	2x10 um WLB	Tapered center and ground
F5	80 um	2x10 um WLB	Tapered center
F6	80 um	2x20 um WLB	
F7	80 um	2x20 um WLB	Tapered center and ground
F8	80 um	2x20 um WLB	Tapered center
F9	80 um	2x50 um WLB	
G1	80 um	2x50 um WLB	Tapered center and ground
G2	80 um	2x50 um WLB	Tapered center
G3	80 um	5x1 um WLB	
G4	80 um	5x1 um WLB	Tapered center and ground
G5	80 um	5x1 um WLB	Tapered center
G6	80 um	5x2 um WLB	
G7	80 um	5x2 um WLB	Tapered center and ground
G8	80 um	5x2 um WLB	Tapered center
G9	80 um	5x5 um WLB	
H1	80 um	5x5 um WLB	Tapered center and ground
H2	80 um	5x5 um WLB	Tapered center
H3	80 um	5x10 um WLB	
H4	80 um	5x10 um WLB	Tapered center and ground
H5	80 um	5x10 um WLB	Tapered center
H6	80 um	5x20 um WLB	
H7	80 um	5x20 um WLB	Tapered center and ground
H8	80 um	5x20 um WLB	Tapered center
H9	80 um	5x50 um WLB	
I1	80 um	5x50 um WLB	Tapered center and ground
I2	80 um	5x50 um WLB	Tapered center
I3	80 um	2x50 um WLB	Bent bridge, for minimal spacing of center line
I4	80 um	2x50 um WLB	Bent bridge, for minimal spacing of center line
I5	80 um	2x50 um WLB	Bent bridge, for minimal spacing of center line
I6	80 um	5x50 um WLB	Bent bridge, for minimal spacing of center line
I7	80 um	5x50 um WLB	Bent bridge, for minimal spacing of center line
I8	80 um	5x50 um WLB	Bent bridge, for minimal spacing of center line
I9	80 um	50x50 um, 1 um, 1 um, ML	w x l of meander box, width of ML, spacing of MLs
J1	80 um	50x50 um, 1 um, 1 um, ML	Tapered center and ground
J2	80 um	50x50 um, 1 um, 1 um, ML	Tapered center
J3	80 um	70x70 um, 1 um, 1 um, ML	
J4	80 um	70x70 um, 1 um, 1 um, ML	
J5	80 um	70x70 um, 1 um, 1 um, ML	Tapered center
J6	80 um	70x70 um, 3 um, 3 um, ML	
J7	80 um	70x70 um, 3 um, 3 um, ML	
J8	80 um	70x70 um, 3 um, 3 um, ML	Tapered center
J9	80 um	70x70 um, 3 um, 1 um, ML	
K1	80 um	70x70 um, 3 um, 1 um, ML	
K2	80 um	70x70 um, 3 um, 1 um, ML	Tapered center
K3	80 um	70x75 um, 5 um, 5 um, ML	
K4	80 um	70x75 um, 5 um, 5 um, ML	
K5	80 um	70x75 um, 5 um, 5 um, ML	Tapered center
K6	80 um	70x75 um, 5 um, 1 um, ML	
K7	80 um	70x75 um, 5 um, 1 um, ML	
K8	80 um	70x75 um, 5 um, 1 um, ML	Tapered center
K9	80 um	70x70 um, 3 um, 3 um, 1(1x1um),ML	width x length of meander box, width of ML,
L1	80 um	70x70 um, 3 um, 3 um, 1(1x1um),ML	spacing of MLs, # of weak links (width x length)
L2	80 um	70x70 um, 3 um, 3 um, 1(1x1um),ML	Tapered center

Continued on next page

Table A.1 – continued from previous page

ID#	Width	Devices	Additional Notes
L3	80 um	70x70 um, 3 um, 3 um, 9(1x1um),ML	
L4	80 um	70x70 um, 3 um, 3 um, 9(1x1um),ML	
L5	80 um	70x70 um, 3 um, 3 um, 9(1x1um),ML	Tapered center
L6	80 um	70x70 um, 3 um, 3 um, 9(1x3um),ML	
L7	80 um	70x70 um, 3 um, 3 um, 9(1x3um),ML	
L8	80 um	70x70 um, 3 um, 3 um, 9(1x3um),ML	Tapered center
L9	80 um	70x70 um, 3 um, 3 um, Blocks(1x1um),ML	Blocks' for when series of YxY um blocks connected by
M1	80 um	70x70 um, 3 um, 3 um, Blocks(1x1um),ML	(yxz um) weak links (Y being the width of the ML)
M2	80 um	70x70 um, 3 um, 3 um, Blocks(1x1um),ML	
M3	80 um	70x70 um, 3 um, 3 um, Blocks(1x1um),ML	Tapered center
M4	80 um	70x70 um, 3 um, 3 um, Blocks(1x1um),ML	Tapered center
M5	80 um	70x70 um, 3 um, 3 um, Blocks(1x3um),ML	
M6	80 um	70x70 um, 3 um, 3 um, Blocks(1x3um),ML	
M7	80 um	70x70 um, 3 um, 3 um, Blocks(1x3um),ML	
M8	80 um	70x70 um, 3 um, 3 um, Blocks(1x3um),ML	Tapered center
M9	80 um	70x70 um, 3 um, 3 um, Blocks(1x3um),ML	Tapered center
N1	80 um	70x70 um, 3 um, 1 um, 1(1x1um),ML	
N2	80 um	70x70 um, 3 um, 1 um, 1(1x1um),ML	
N3	80 um	70x70 um, 3 um, 1 um, 1(1x1um),ML	Tapered center
N4	80 um	70x70 um, 3 um, 1 um, 1(1x3um),ML	
N5	80 um	70x70 um, 3 um, 1 um, 1(1x3um),ML	
N6	80 um	70x70 um, 3 um, 1 um, 1(1x3um),ML	Tapered center
N7	80 um	70x70 um, 3 um, 1 um, 15(1x1um),ML	
N8	80 um	70x70 um, 3 um, 1 um, 15(1x1um),ML	
N9	80 um	70x70 um, 3 um, 1 um, 15(1x1um),ML	Tapered center
P1	80 um	70x70 um, 3 um, 1 um, 15(1x3um),ML	
P2	80 um	70x70 um, 3 um, 1 um, 15(1x3um),ML	
P3	80 um	70x70 um, 3 um, 1 um, 15(1x3um),ML	Tapered center
P4	80 um	70x70 um, 3 um, 1 um, Blocks(1x1um),ML	
P5	80 um	70x70 um, 3 um, 1 um, Blocks(1x1um),ML	
P6	80 um	70x70 um, 3 um, 1 um, Blocks(1x1um),ML	
P7	80 um	70x70 um, 3 um, 1 um, Blocks(1x1um),ML	Tapered center
P8	80 um	70x70 um, 3 um, 1 um, Blocks(1x1um),ML	Tapered center
P9	80 um	70x70 um, 3 um, 1 um, Blocks(1x3um),ML	
Q1	80 um	70x70 um, 3 um, 1 um, Blocks(1x3um),ML	
Q2	80 um	70x70 um, 3 um, 1 um, Blocks(1x3um),ML	
Q3	80 um	70x70 um, 3 um, 1 um, Blocks(1x3um),ML	Tapered center
Q4	80 um	70x70 um, 3 um, 1 um, Blocks(1x3um),ML	Tapered center
Q5	80 um	3x1 um WLB	
Q6	80 um	3x1 um WLB	Tapered center and ground
Q7	80 um	3x1 um WLB	Tapered center
Q8	80 um	3x2 um WLB	
Q9	80 um	3x2 um WLB	Tapered center and ground
R1	80 um	3x2 um WLB	Tapered center
R2	80 um	3x5 um WLB	
R3	80 um	3x5 um WLB	Tapered center and ground
R4	80 um	3x5 um WLB	Tapered center
R5	80 um	3x10 um WLB	
R6	80 um	3x10 um WLB	Tapered center and ground
R7	80 um	3x10 um WLB	Tapered center
R8	80 um	3x20 um WLB	
R9	80 um	3x20 um WLB	Tapered center and ground
S1	80 um	3x20 um WLB	Tapered center
S2	80 um	3x50 um WLB	
S3	80 um	3x50 um WLB	Tapered center and ground
S4	80 um	3x50 um WLB	Tapered center
S5	80 um	3x50 um WLB	Bent bridge, for minimal spacing of center line
S6	80 um	3x50 um WLB	Bent bridge, for minimal spacing of center line
S7	80 um	3x50 um WLB	Bent bridge, for minimal spacing of center line
S8	80 um	2 parallel 1x1 um WLB	
S9	80 um	3 parallel 1x1 um WLB	
T1	80 um	2 parallel 1x2 um WLB	
T2	80 um	3 parallel 1x2 um WLB	
T3	80 um	2 parallel 1x5 um WLB	

Continued on next page

Table A.1 – continued from previous page

ID#	Width	Devices	Additional Notes
T4	80 um	3 parallel 1x5 um WLB	
T5	80 um	2 parallel 1x10 um WLB	
T6	80 um	3 parallel 1x10 um WLB	
T7	80 um	1x1 um WLB	
T8	80 um	1x1 um WLB	
T9	80 um	70x75 um, 5 um, 5 um, 1(1x1um),ML	width x length of meander box, width of ML,
U1	80 um	70x75 um, 5 um, 5 um, 1(1x1um),ML	spacing of MLs, # of weak links (width x length)
U2	80 um	70x75 um, 5 um, 5 um, 1(1x1um),ML	Tapered center
U3	80 um	70x75 um, 5 um, 5 um, 1(1x3um),ML	
U4	80 um	70x75 um, 5 um, 5 um, 1(1x3um),ML	
U5	80 um	70x75 um, 5 um, 5 um, 1(1x3um),ML	Tapered center
U6	80 um	70x75 um, 5 um, 5 um, 5(1x1um),ML	
U7	80 um	70x75 um, 5 um, 5 um, 5(1x1um),ML	
U8	80 um	70x75 um, 5 um, 5 um, 5(1x1um),ML	Tapered center
U9	80 um	70x75 um, 5 um, 5 um, 5(1x3um),ML	
V1	80 um	70x75 um, 5 um, 5 um, 5(1x3um),ML	
V2	80 um	70x75 um, 5 um, 5 um, 5(1x3um),ML	Tapered center
V3	80 um	70x75 um, 5 um, 5 um, Blocks(1x1um),ML	Blocks' for when series of YxY um blocks connected
V4	80 um	70x75 um, 5 um, 5 um, Blocks(1x1um),ML	by (yxz um) weak links (Y being the width size of the ML)
V5	80 um	70x75 um, 5 um, 5 um, Blocks(1x1um),ML	
V6	80 um	70x75 um, 5 um, 5 um, Blocks(1x1um),ML	Tapered center
V7	80 um	70x75 um, 5 um, 5 um, Blocks(1x1um),ML	Tapered center
V8	80 um	70x75 um, 5 um, 5 um, Blocks(1x3um),ML	
V9	80 um	70x75 um, 5 um, 5 um, Blocks(1x3um),ML	
W1	80 um	70x75 um, 5 um, 5 um, Blocks(1x3um),ML	
W2	80 um	70x75 um, 5 um, 5 um, Blocks(1x3um),ML	Tapered center
W3	80 um	70x75 um, 5 um, 5 um, Blocks(1x3um),ML	Tapered center
W4	80 um	70x75 um, 5 um, 1 um, 1(1x1um),ML	
W5	80 um	70x75 um, 5 um, 1 um, 1(1x1um),ML	
W6	80 um	70x75 um, 5 um, 1 um, 1(1x1um),ML	Tapered center
W7	80 um	70x75 um, 5 um, 1 um, 1(1x3um),ML	
W8	80 um	70x75 um, 5 um, 1 um, 1(1x3um),ML	
W9	80 um	70x75 um, 5 um, 1 um, 1(1x3um),ML	Tapered center
X1	80 um	70x75 um, 5 um, 1 um, 10(1x1um),ML	
X2	80 um	70x75 um, 5 um, 1 um, 10(1x1um),ML	
X3	80 um	70x75 um, 5 um, 1 um, 10(1x1um),ML	Tapered center
X4	80 um	70x75 um, 5 um, 1 um, 10(1x3um),ML	
X5	80 um	70x75 um, 5 um, 1 um, 10(1x3um),ML	
X6	80 um	70x75 um, 5 um, 1 um, 10(1x3um),ML	Tapered center
X7	80 um	70x75 um, 5 um, 1 um, Blocks(1x1um),ML	
X8	80 um	70x75 um, 5 um, 1 um, Blocks(1x1um),ML	
X9	80 um	70x75 um, 5 um, 1 um, Blocks(1x1um),ML	
Y1	80 um	70x75 um, 5 um, 1 um, Blocks(1x1um),ML	Tapered center
Y2	80 um	70x75 um, 5 um, 1 um, Blocks(1x1um),ML	Tapered center
Y3	80 um	70x75 um, 5 um, 1 um, Blocks(1x3um),ML	
Y4	80 um	70x75 um, 5 um, 1 um, Blocks(1x3um),ML	
Y5	80 um	70x75 um, 5 um, 1 um, Blocks(1x3um),ML	
Y6	80 um	70x75 um, 5 um, 1 um, Blocks(1x3um),ML	Tapered center
Y7	80 um	70x75 um, 5 um, 1 um, Blocks(1x3um),ML	Tapered center
0A1	80 um	50x50 um, 1 um, 1 um, Square Spiral	Non-Inductive Design
0A2	80 um	50x50 um, 1 um, 1 um, Square Spiral	
0A3	80 um	50x50 um, 1 um, 1 um, Square Spiral	
0A4	80 um	50x50 um, 1 um, 1 um, Square Spiral	Tapered center
0A5	80 um	50x50 um, 1 um, 1 um, Square Spiral	Tapered center
0B1	80 um	70x70 um, 1 um, 1 um, Square Spiral	
0B2	80 um	70x70 um, 1 um, 1 um, Square Spiral	
0B3	80 um	70x70 um, 1 um, 1 um, Square Spiral	
0B4	80 um	70x70 um, 1 um, 1 um, Square Spiral	Tapered center
0B5	80 um	70x70 um, 1 um, 1 um, Square Spiral	Tapered center
0C1	80 um	50x50 um, 1 um, 1 um, Circle Spiral	
0C2	80 um	50x50 um, 1 um, 1 um, Circle Spiral	
0C3	80 um	50x50 um, 1 um, 1 um, Circle Spiral	
0C4	80 um	50x50 um, 1 um, 1 um, Circle Spiral	Tapered center

Continued on next page

Table A.1 – continued from previous page

ID#	Width	Devices	Additional Notes
0C5	80 um	50x50 um, 1 um, 1 um, Circle Spiral	Tapered center
0D1	80 um	70x70 um, 3 um, 3 um, 1(1x3um),Square Spiral	
0D2	80 um	70x70 um, 3 um, 3 um, 19(1x3um),Square Spiral	
0D3	80 um	70x70 um, 3 um, 3 um, 19(1x3um),Square Spiral	Tapered center
0D4	80 um	70x70 um, 3 um, 3 um, 39(1x3um),Square Spiral	
0D5	80 um	70x70 um, 3 um, 3 um, 39(1x3um),Square Spiral	
0E1	80 um	70x70 um, 3 um, 3 um, 39(1x3um),Square Spiral	Tapered center
0E2	80 um	70x70 um, 3 um, 1 um, 1(1x1um), Square Spiral	
0E3	80 um	70x70 um, 3 um, 1 um, 1(1x1um), Square Spiral	
0E4	80 um	70x70 um, 3 um, 1 um, 1(1x1um), Square Spiral	Tapered center
0E5	80 um	70x70 um, 3 um, 1 um, 1(1x1um), Square Spiral	Tapered center
0F1	80 um	70x70 um, 3 um, 1 um, 31(1x1um), Square Spiral	
0F2	80 um	70x70 um, 3 um, 1 um, 31(1x1um), Square Spiral	
0F3	80 um	70x70 um, 3 um, 1 um, 31(1x1um), Square Spiral	
0F4	80 um	70x70 um, 3 um, 1 um, 31(1x1um), Square Spiral	Tapered center
0F5	80 um	70x70 um, 3 um, 1 um, 31(1x1um), Square Spiral	Tapered center
0G1	80 um	70x70 um, 3 um, 3 um, Circle Spiral	
0G2	80 um	70x70 um, 3 um, 3 um, Circle Spiral	
0G3	80 um	70x70 um, 3 um, 3 um, Circle Spiral	
0G4	80 um	70x70 um, 3 um, 3 um, Circle Spiral	Tapered center
0G5	80 um	70x70 um, 3 um, 3 um, Circle Spiral	Tapered center
0H1	80 um	70x70 um, 3 um, 3 um, 19(1x3um), Circle Spiral	
0H2	80 um	70x70 um, 3 um, 3 um, 19(1x3um), Circle Spiral	
0H3	80 um	70x70 um, 3 um, 3 um, 31(1x3um), Circle Spiral	
0H4	80 um	70x70 um, 3 um, 3 um, 19(1x3um), Circle Spiral	Tapered center
0H5	80 um	70x70 um, 3 um, 3 um, 31(1x3um), Circle Spiral	Tapered center
0I1	80 um	70x70 um, 3 um, 1 um, Circle Spiral	
0I2	80 um	70x70 um, 3 um, 1 um, Circle Spiral	
0I3	80 um	70x70 um, 3 um, 1 um, Circle Spiral	
0I4	80 um	70x70 um, 3 um, 1 um, Circle Spiral	Tapered center
0I5	80 um	70x70 um, 3 um, 1 um, Circle Spiral	Tapered center
0J1	80 um	70x70 um, 3 um, 1 um, 27(1x1um), Circle Spiral	
0J2	80 um	70x70 um, 3 um, 1 um, 27(1x1um), Circle Spiral	
0J3	80 um	70x70 um, 3 um, 1 um, 27(1x1um), Circle Spiral	
0J4	80 um	70x70 um, 3 um, 1 um, 27(1x1um), Circle Spiral	Tapered center
0J5	80 um	70x70 um, 3 um, 1 um, 27(1x1um), Circle Spiral	Tapered center
0K1	80 um	20 parallel 1x50um bridges	
0K2	80 um	20 parallel 1x50um bridges	
0L1	80 um	20 parallel 1x50um bridges with thatching	
0L2	80 um	20 parallel 1x50um bridges with thatching	
0M1	80 um	70x75 um, 5 um, 1 um, 2(1x2um),ML	
0M2	80 um	70x75 um, 5 um, 1 um, 2(1x2um),ML	
0M3	80 um	70x75 um, 5 um, 1 um, 2(1x2um),ML	
0M4	80 um	70x75 um, 5 um, 1 um, 2(1x2um),ML	Tapered center
0M5	80 um	70x75 um, 5 um, 1 um, 2(1x2um),ML	Tapered center
QA	80 um	70x70 um, 3 um, 1 um, 2(1x1um),ML	Weak links at ends
QB	80 um	70x70 um, 3 um, 1 um, 2(1x1um),ML	
QC	80 um	70x70 um, 3 um, 1 um, 2(1x1um),ML	Tapered center
QD	80 um	70x70 um, 3 um, 1 um, 2(1x1um),ML	
QE	80 um	70x70 um, 3 um, 1 um, 2(1x1um),ML	
QF	80 um	70x70 um, 3 um, 1 um, 2(1x1um),ML	Tapered center

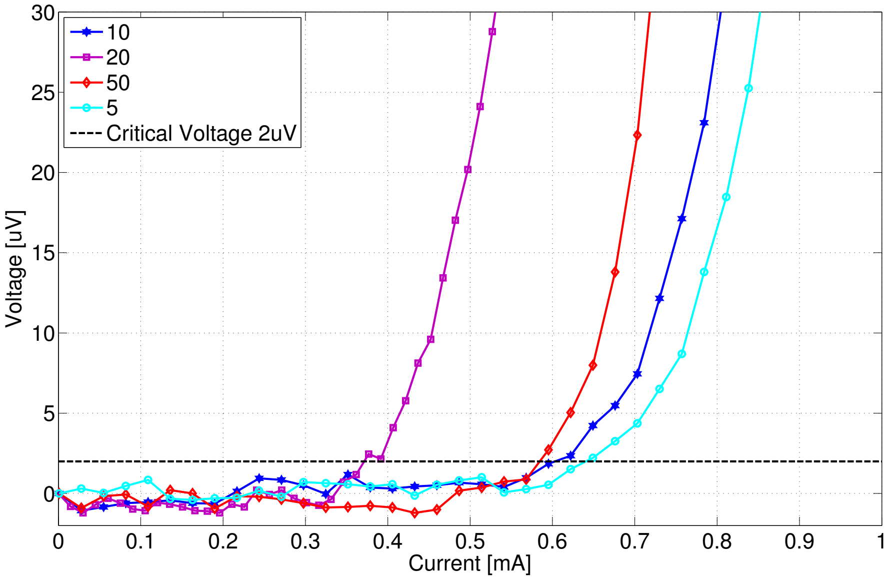

Figure A.1: IV Sweeps of 3 width microbridges by X length [um]. Clear relation between length and I$_c$ can be seen. The discrepancy with the 20 length bridge is likely due to a narrow constriction point due to fabrication error.

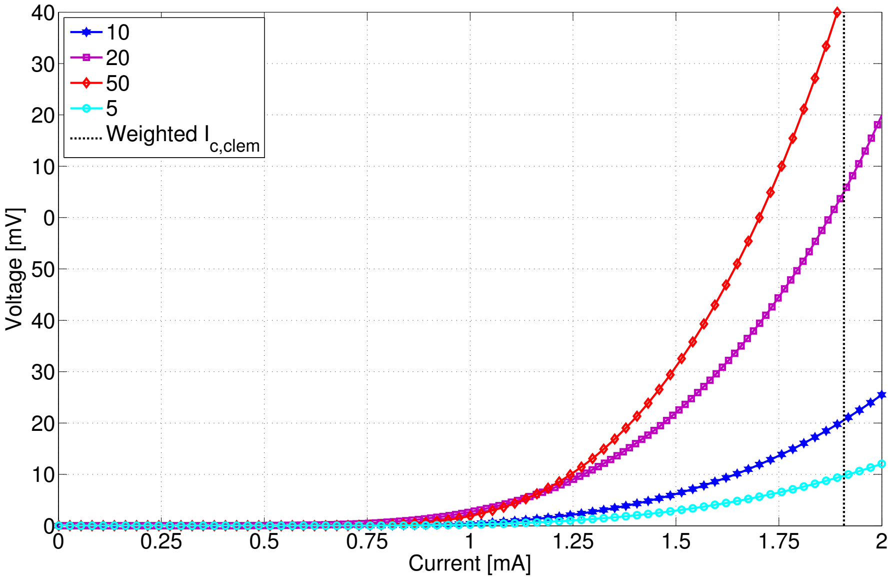

Figure A.2: High voltage measurement of 3 width microbridges by X length [um]. Theoretical I$_c$s shown. The 20 length bridge behaviour is as expected at higher voltages, supporting the reasoning for the error seen in Fig. A.1

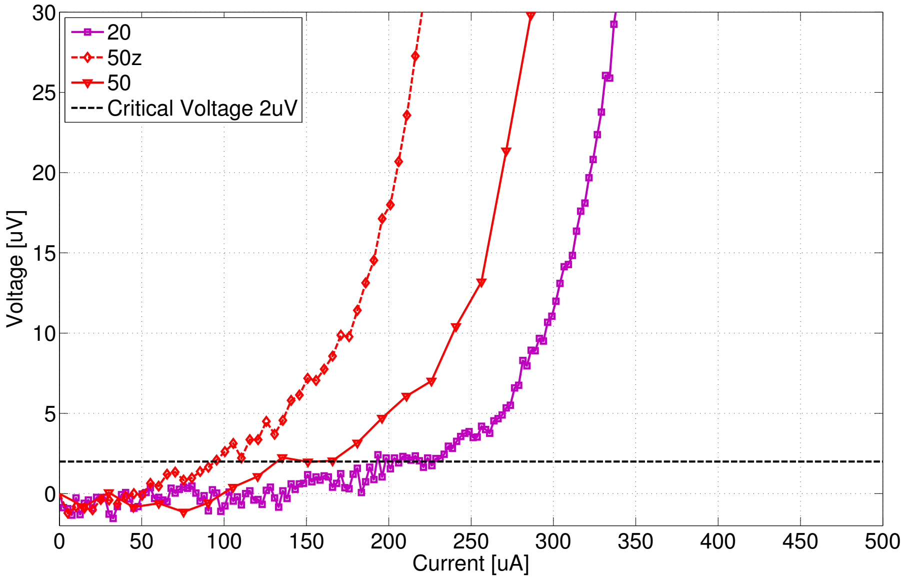

Figure A.3: IV Sweeps of 2 width microbridges by X length [um]. Clear relation between length and I_c can be seen.

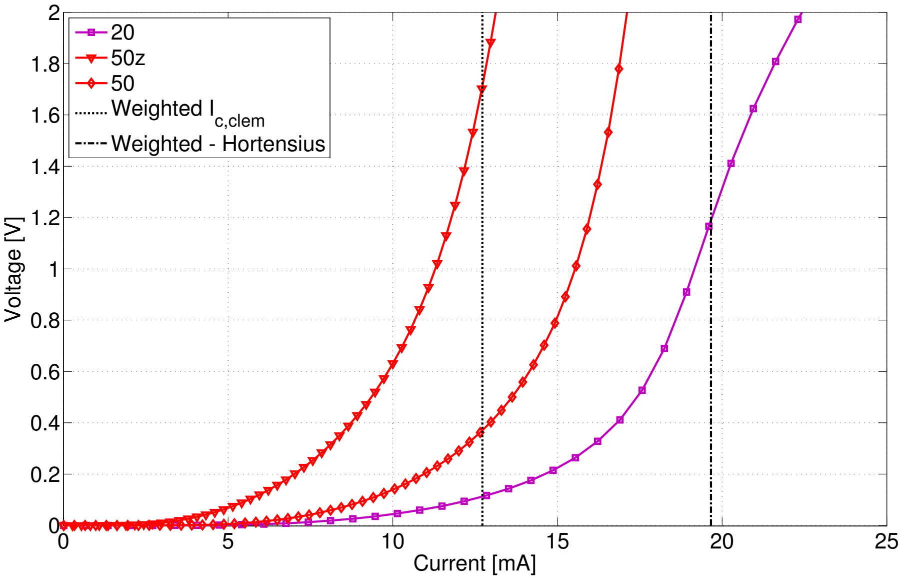

Figure A.4: High voltage measurement of 2 width microbridges by X length [um]. Theoretical I_cs shown

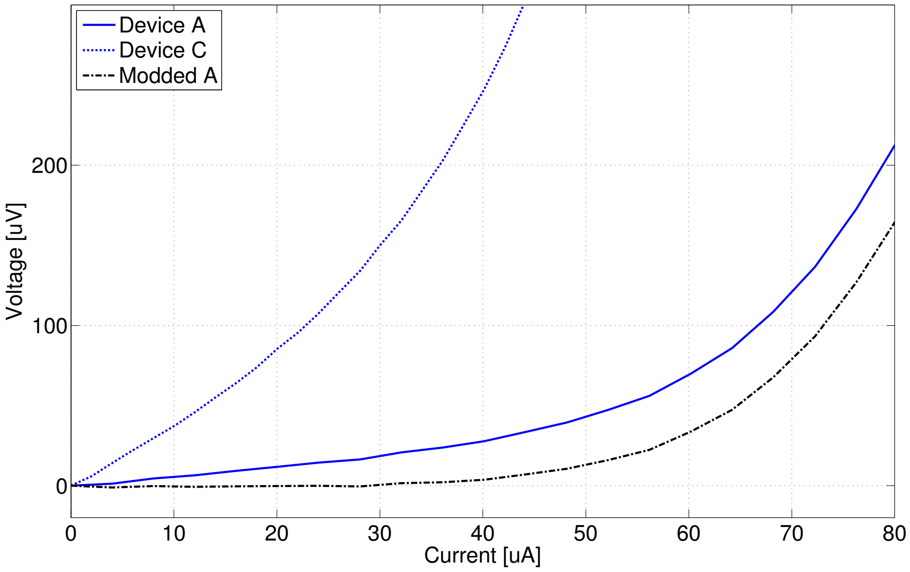

Figure A.5: Two different copies of device OF1. Linear resistance present due to 1x1 [um] embedded bridges. Modded plot removes the linear resistance.

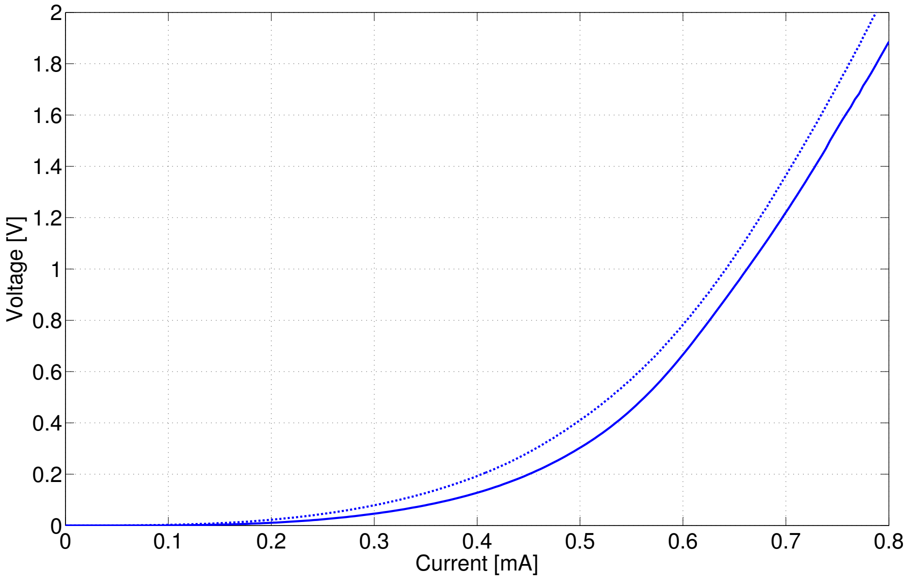

Figure A.6: High voltage measurement of OF1 devices.

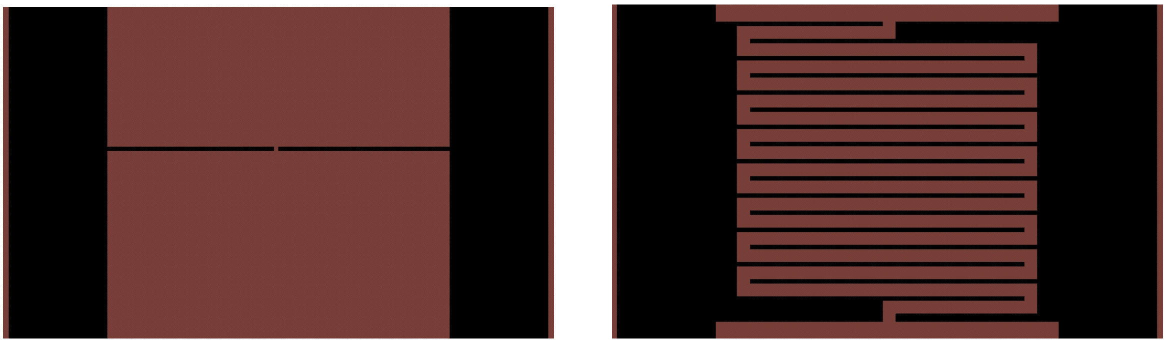

(a) Microbridge - B6

(b) Meander line - J9

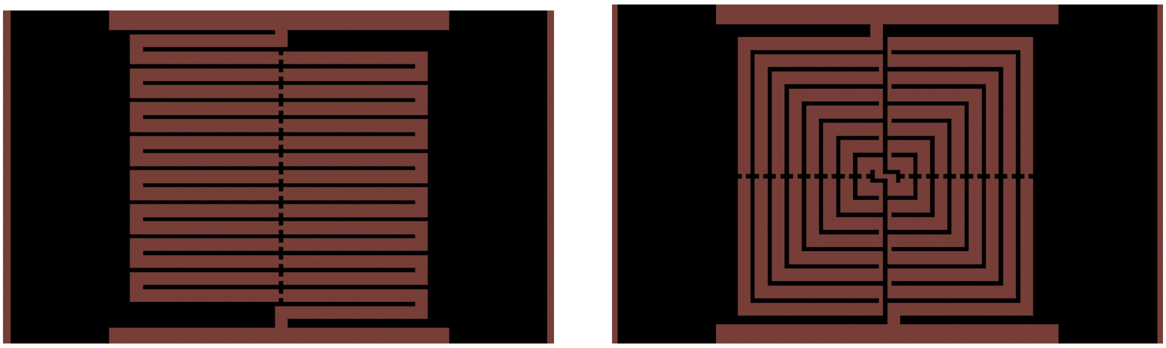

(c) Meander line with bridges - N7

(d) Square Meander - OF3

(e) Circle Meander - OH1

Figure A.7: Examples of different device designs and the device name from Table A.1.

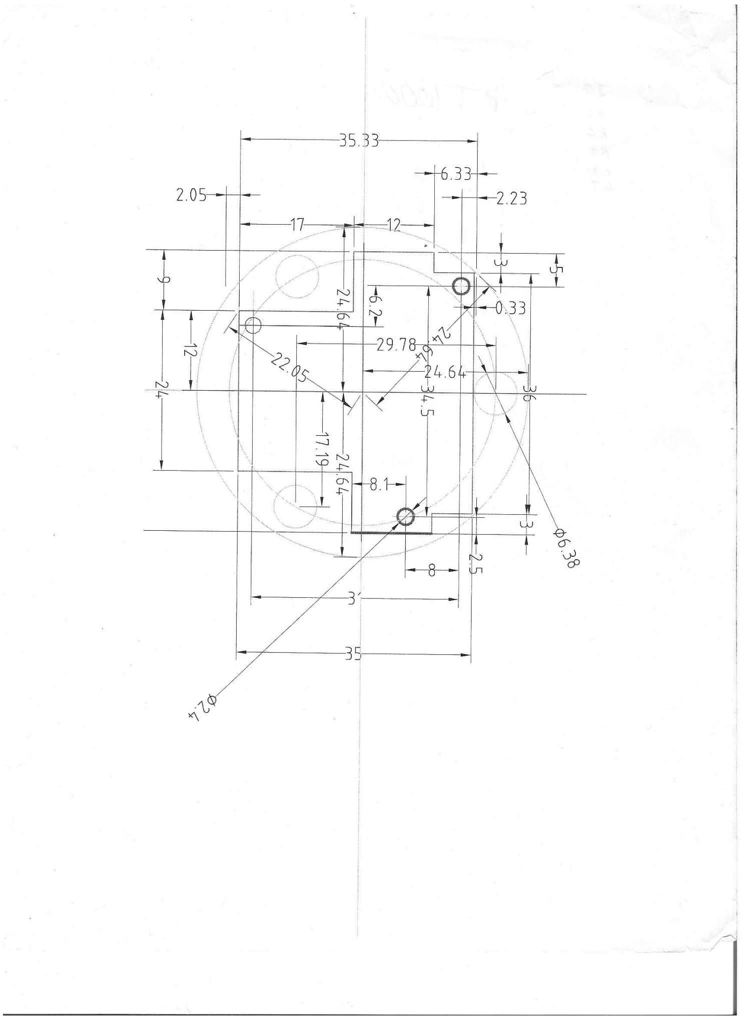

Figure A.8: CAD file for PCB and copper sample base screw alignment and dimensions - in cooperation with physics machine shop.

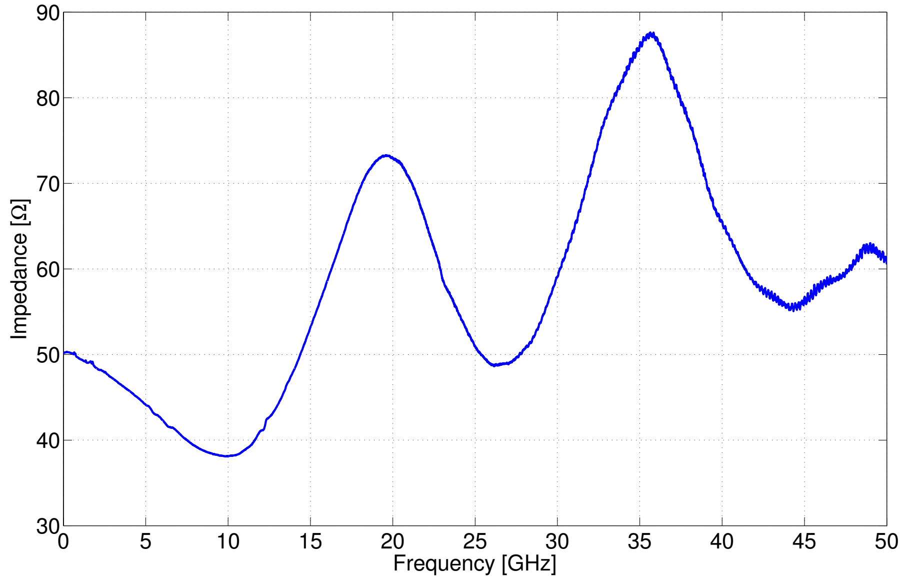

Figure A.9: Characteristic impedance of the 80 [um] CPW.

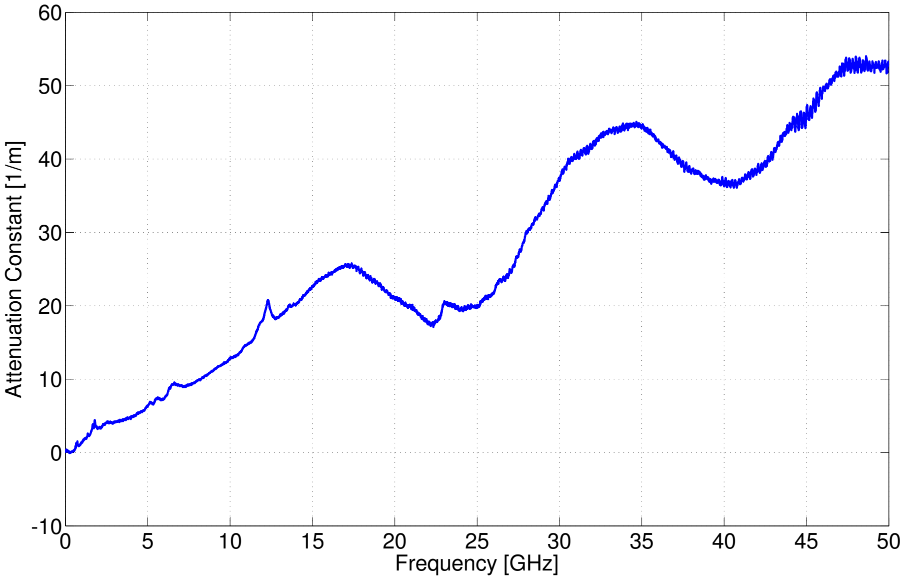

Figure A.10: Attenuation constant of the 80 [um] CPW.

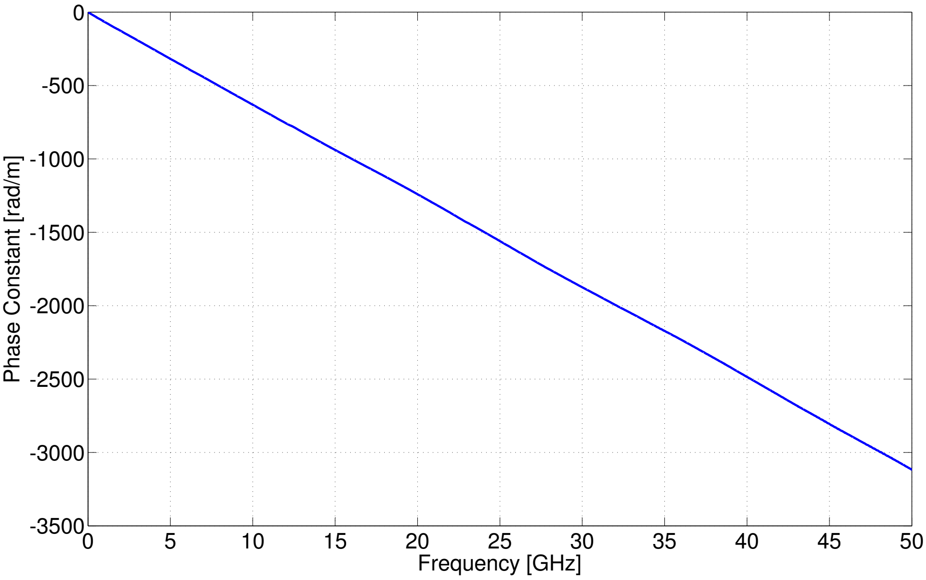

Figure A.11: Phase Constant of the 80 [um] CPW.